Tesis Doctoral

EXTRACCIÓN EVOLUTIVA DE PARÁMETROS EN MODELOS COMPACTOS DE TRANSISTORES ORGÁNICOS DE LÁMINA DELGADA.

Autor:

ADRIÁN ROMERO CÁCERES

Directores:

Jesús González Peñalver
Juan Antonio Jiménez Tejada

Programa de Doctorado en Tecnologías de la Información y Comunicación (B25.56.1)

Universidad de Granada
2019

Editor: Universidad de Granada. Tesis Doctorales
Autor: Adrián Romero Cáceres
ISBN: 978-84-1306-364-5
URI: http://hdl.handle.net/10481/58061

A Thesis for the Degree of Doctor of philosophy

EVOLUTIVE EXTRACTION OF PARAMETERS IN ORGANIC THIN-FILM TRANSISTORS COMPACT MODELS.

Author:

ADRIÁN ROMERO CÁCERES

Supervisors:

Jesús González Peñalver
Juan Antonio Jiménez Tejada

Doctorate program on Information and Communication Technologies (B25.56.1)

University of Granada
2019

Acknowledgments

To my life-support, my girlfriend Sara: because you have stayed by my side in good times and bad. Many Thanks!

I would like to express deep appreciation and gratitude to my tutor and director, Prof. Jesús González Peñalver, for his invaluable help, for all the time that he has devoted to me, his constant encouragement and support, his patience and for sharing with me his scientific knowledge. He is an exceptional researcher in the evolutionary computation field. His guidance helped me during the time of research and writing of this thesis. Everything started with the final project in the Degree in Computer Science Engineering. It was followed by the TFM of the Master in Data Science and Computer Engineering and finally with this thesis. Without his guidance and constant help this thesis would not be possible. From all my heart, I will always be grateful to you.

I would also like to express my special appreciation and thanks to my co-director, Prof. Juan Antonio Jiménez Tejada, for the continuous support, for his patience, motivation, and immense knowledge. He is an exceptional researcher in the modeling of semiconductor devices. I could not have imagined having a better co-director and mentor for this thesis. Everything started when Jesús and I were looking for an expert in the field of organic transistors modeling. After several emails and Skype calls, Juan Antonio decided to take part in this project, and for that, I will eternally grateful to you. Without his guidance and constant help this thesis would not be possible. Thank you from the bottom of my heart.

Last but not the least, I would like to thank my family: my parents and my brothers for supporting me spiritually throughout writing this thesis and in my life in general.

Thanks to all of you,

Adrián

Abstract

Organic thin-film transistors (OTFTs) have attracted considerable research interest because of the benefits associated to their constituent materials, such as flexibility, low fabrication costs and weight, and their potential applications in large-area, flexible electronics, such as displays and sensors. Nevertheless, they also have important limitations, for example a low carrier mobility compared to inorganic TFTs, high process variability, or degraded performance characteristics due to contact effects. Contact effects, specifically, have been extensively studied in order to introduce them in transistor compact models. For the purpose of obtaining the values of these models, parameter extraction procedures are normally applied to the device output characteristics. It has to be noted that the parameter extraction is a complex procedure when contact effects are present, since the device $I - V$ characteristics are affected by them. This work focuses on developing an efficient procedure to extract the parameters of an OTFT compact model, in which contact effects are taken into account. This compact model is valid for all the operation regimes of the transistors.

This thesis begins with the proposal of a multi-objective evolutionary algorithm (MOEA), which is employed to simultaneously determine (i) the values of the parameters of a compact model for the current-voltage characteristics of OTFTs and (ii) the voltage drop at the contact region. This procedure can be used to overcome shortcomings of previous parameter extraction procedures. With the challenge of improving the accuracy of the estimated parameters, additional objectives and constraints are added to guide the search process. The intention is to explore more promising areas, in which even more accurate parameter sets may be found. As a result, the initial multi-objective problem (MOP) gives place to a many-objective problem (MaOP). By means of the many-objective procedure, high quality parameter sets are estimated.

In an effort to extend the applicability of our extraction method to other devices and physical mechanisms, the work includes a study of the effect of illumination on organic phototransistors (OPTs), emphasizing the effect of the light on the contact region. For this purpose, the compact model for the $I - V$ characteristics of OTFTs is redesigned for OPTS. This compact model includes a model for the contact region of the device that incorporates the effects of illumination (photovoltaic and photoconductive effects). Then, our evolutionary procedure is applied to published experimental data from several OPTs under different illumination conditions. After the parameter extraction, the compact model and the contact region model are validated by reproducing the experimental data using the estimated parameter sets. The results show that both photoconductive and photovoltaic effects impact

the intrinsic region of the transistor, as well as the electrical behavior of the contact region.

The work ends with improvements on the model for the contact region of the OTFTs. In particular, a standard model for the contact region of OTFTs is proposed. It is a versatile model that describes the current-voltage characteristics of different kinds of contacts. It reproduces the behavior of Schottky-barrier or space-charge limited contacts. It is a simple unified model since only the value of a single parameter is necessary in order to distinguish between both kinds of contacts. The model is easily integrated in the generic compact model for the current-voltage characteristics of OTFTs used in this work. The resulting compact model, used in combination with the evolutionary parameter extraction procedure, allows to extract the intrinsic parameters and the current-voltage curves at the contact of single short-channel transistors. The model is tested with published experimental data of OTFTs with Schottky-barrier or space-charge limited contacts. Finally, the method has been used as a diagnose tool in order to analyze how an ammonia sensor reacts to different concentrations of the ammonia gas. Interestingly, alterations in the contact region have been detected when the gas concentration varies, transforming the space-charge limited contact of a pristine OTFT into a Schottky-barrier contact under the exposure of gas.

Contents

1

Introduction and background

1.1. Motivation

Organic thin-film transistors (OTFTs) have attracted considerable research interest due to the advantages associated with the materials used, such as flexibility, low manufacturing costs and weight, and their possible applications in large area flexible electronic devices, such as screens and sensors [1]. However, they also have important limitations, for example, low carrier mobility compared to inorganic TFT transistors, high process variability, or degraded performance due to contact effects. The contact effects, specifically, have been widely studied for the purpose of introducing them in compact models of transistors [2–4].

Compact models are analytical models that can reproduce the electrical behavior of a determined device in all regimes of operation. In general, they are based on physical principles, with some free parameters that are used to ensure a continuous transition between modes or to simplify the device physics. Therefore, these models must be associated with methods to extract their respective parameters, using as a basis the electrical characteristics of the corresponding transistor [3–5]. The extracted parameters must have a correct physical value, since an invalid value of any of them would mean the invalidation of the extracted parameter set, and therefore, a failure of the parameter search process. Finally, the extracted parameter set must provide an accurate agreement between the data simulated using the model and the experimental data employed for the extraction.

1.2. Objectives and Methodology

This thesis is focused on the definition of a procedure to extract parameters of a compact model for OTFTs, including those related with the contact effects, from the device output characteristics. This procedure must ensure that a parameter set is reached, thereby, solving some limitations presented in the procedures found in the bibliography. For this purpose, the following goals are outlined:

1. Describe an efficient methodology for the extraction of the parameters of an OTFT compact model, which includes the effects of the contacts using a multi-objective evolutionary algorithm (MOEA).

2. Validate the extracted parameter set with physical and electrical laws that describe the behavior of the device. The parameter set validation must include the validation of both the evolutionary procedure and the compact model.

3. Provide the evolutionary procedure with expert knowledge. The search process have to explore more promising areas, in which more accurate parameter sets are found.

4. Expand the functionality of the compact model to new applications of the OTFTs such as sensors. The purpose of this objective is the standardization of the evolutionary procedure, encompassing as many physical phenomena and applications as possible.

In order to carry out this research, it is necessary to give a brief introduction on how OTFTs operate, including the different degrading effects limiting the device performance, with a special attention to the

contact effects, and also to give a brief description on how evolutionary algorithms work. This is done in the next section.

1.3. Background

1.3.1. Organic Materials

Organic materials used in organic devices can be classified into polymers, small molecules, doped organic semiconductors, charge transfer complexes, and organic semiconductor/insulator composites [6]. Among them, polymers semiconductors are preferred for leads and contacts in organic devices because of their suitability for printing. Their main characteristics are: they do not require the use of halogenated solvents, which present both environmental and regulatory concerns; they are also less susceptible to adhesion issues, their solubility profiles more easily enable access to viscosity values larger than 200 mPa.s and they provide significantly greater device-to-device uniformity [7, 8].

Transistors, diodes, sensors [9], transducers, and memory elements can incorporate semiconductors consisting of organic molecular solids and/or semiconducting polymers (named organic semiconductors). Applications of these devices can be found in circuits of moderate complexity, such as display drivers [10], radio-frequency identification (RFID) tags [11], or pressure mapping elements.

The lowest unoccupied molecular orbital (LUMO) of most conjugated organic compounds lie outside the preferred ranges for electron transport. This is the reason why there are considerably fewer molecular structures that have been identified as preferentially electron-carrying (n-channel) transistor semiconductors in comparison with the hole-transporting (p-channel) semiconductors. The amount of holes in the semiconductor is mainly determined by the relative position of the highest occupied molecular orbital (HOMO) to the Fermi level in the contact (contact work function).

This technological delay regarding n-channel transistors directly has affected the development of complementary technology. There has been a particular need for n-channel organic semiconductors to level the performance of p-channel materials, in order to design complementary circuits with organic transistors. Significant progress was made on the development of solution processable organic semiconductors and both p- and n-type materials that present high performance and good air-stability [12, 13]. In complementary circuits, both positive and negative gate voltages are used to switch transistors, which are characterized by better speed and reliability when compared to their unipolar counterparts [14, 15]. Several organic complementary circuits made with solution deposited materials were also reported [13, 14, 16, 17], but there is no fully printed complementary technology on flexible substrate presenting high mobility for both p- and n-type semiconductors [11].

1.3.2. Organic Field-Effect Transistor

An Organic Field-Effect Transistor (OFET) is an electronic device whose structure turns around a capacitor-like structure. It is formed by a metallic gate, a dielectric, and semiconductor layers. Two metal contacts, the source and drain electrodes, are connected electrically to the semiconductor film. The

organic semiconductor layer is usually very thin, this is the reason why these transistors are also called Organic Thin-Film Transistors (OTFTs). The position of these electrodes at the top of the structure or embedded between the semiconductor and the insulator define the top-contact and bottom-contact configurations, respectively. The conductive gate electrode is also used as substrate, providing mechanical support to the structure. Insulating oxide or polymeric insulators coated on the gate, with or without surface treatment, act as dielectric layers. Without applied gate voltage V_G, the intrinsic conductivity of most organic semiconductors is low; when a voltage V_D is applied between drain and source, very little current can flow through the thin semiconductor film, and the device is in the OFF-state. When a gate voltage V_G is applied on the gate, the electric field existing across the capacitor structure attracts charges towards the dielectric-semiconductor interface. These accumulated charges are mostly mobile and give rise to a conducting channel between source and drain. These mobile charges can move in response to the applied V_D. The transistor is working in the ON-state or accumulation mode.

There is a threshold voltage, V_T, above which the conducting channel is formed. The value of this threshold voltage depends on different internal mechanisms of the structure. Most organic semiconductors are not intentionally doped so that charges are actually injected and extracted from source and drain electrodes. For most cases, there is a mismatch between the Fermi level of metal electrodes and the HOMO (LUMO) of the p-channel (n-channel) semiconductors, which induces charge injection barriers. A non zero V_G is required to shift the molecular orbital energy levels of semiconductors up or down so that the molecular orbitals become resonant with the Fermi level of metal electrodes and reduce the charge injection barriers. In addition, there are always trap states in the semiconductor film that are induced from impurities and defects (including grain boundaries), as well as molecules such as H_2O and O_2 adsorbed from the environment. A non zero V_G must be applied to fill these trap states before mobile charges can be transported along the conducting channel. All those effects affect the value of the threshold voltage V_T.

The experimental current-voltage curves of the OFET are very similar to the MOSFET. This is the reason why the OFETs have extensively been described with the classical equations that describe the MOS transistor drain current I_D:

$$\begin{aligned} I_D &= \frac{W\mu_0 C_i}{L}\left[(V_G - V_T)V_D - \frac{V_D^2}{2}\right],\ V_D < V_G - V_T \\ I_D &= \frac{W\mu_0 C_i}{2L}\left[(V_G - V_T)^2\right],\ V_D \leq V_{GS} - V_T \end{aligned} \tag{1.1}$$

where C_i is the gate insulator capacitance per unit area, μ_0 is the carrier mobility and W and L are the channel width and length, respectively.

There are some aspects that need special consideration and make the OFETs to separate from ideal MOS model (1.1): the injection of charge from the contacts, the transport of charge in the organic semiconductor and the instabilities created by the charge build-up in the structure. Because of them, among others factors, model (1.1) is not able to reproduce the $I - V$ characteristics of OFETs, being mandatory for such a purpose the use of specific models.

1.3.3. Contacts Effects

Understanding and reducing contact effects in OTFTs are of great technological importance since they limit the device performance [18]. There are experimental evidences that prove the presence of these degrading effects, and therefore the existence of the contact region. The first one is obvious because of the nature of the different material that constitute the contacts. We can find a second reason in surface micro-graphs of the contact regions. They show how the density of molecules in the organic material are not the same just at the metallurgical contact or far from it. A third reason is found in scanning potentiometer measurements. These measurements can monitor the voltage drop between source and drain. In many cases, they show a larger voltage drop between the source-contact (injecting contact) than in the drain contact (collecting contact). In this situation, the voltage drop between the drain and the intrinsic channel can be neglected.

Great efforts have been made in order to reduce the impact of contact effects and hence, to improve the device performance. Among the attempts to reduced the contacts effects are the use of new materials for the contact electrodes, the insertion of layers at the metal-semiconductor interface, or the use of molecular doping. In addition, models capable of reproducing the current-voltage curves at the contacts of OTFTs have been developed [4, 19], being this still a topic of major interest [20].

1.3.4. Evolutionary Algorithms

Evolutionary Algorithms (EAs) are meta-heuristics based on natural and genetic evolution [21, 22]. The concept of natural evolution will help the reader to get an initial idea about how EAs work. In nature, there are entities or populations of individuals with the ability of reproduction. These individuals usually have different characteristics, such as height or strength. The offspring individuals inherit some characteristics of their progenitors. In addition, some of them may mutate acquiring new qualities. As time passes, only the individuals able to adapt to the environment survive, usually the fittest ones. Taking as reference the natural evolution, EAs process at each iteration a population of potential solutions (individuals) for a determined problem (environment). During the EA execution the potential solutions are combined (reproduction) and some of them may be altered (mutation), giving rise to an offspring population, in which the fittest potential solutions have the highest probability of remaining in it (adaptation to the environment).

The most important difference between classical optimization techniques and EAs is that they process a population of potential solutions at each iteration, rather than a single solution for the problem. Fig. 1.1 shows the basic flow chart of an EA, where P_t is the population of the EA in the t-th iteration and N is the population size. The individuals of the population are potential solutions of a minimization (maximization) function $f(x)$. They are named $x^{(i,t)} = ({x_1}^{(i,t)}, \ldots, {x_p}^{(i,t)})$, $i = 1, 2, \ldots, N$ and $x^{(i,t)} \in X^p \subseteq \mathbb{R}^p$, where X^p is the domain of the population.

Three main operators guide the evolution of the population:

- *Recombination operator*. It is mainly responsible for the population to improve. This operator mixes characteristics of progenitors in order to create new individuals, called offsprings. The idea

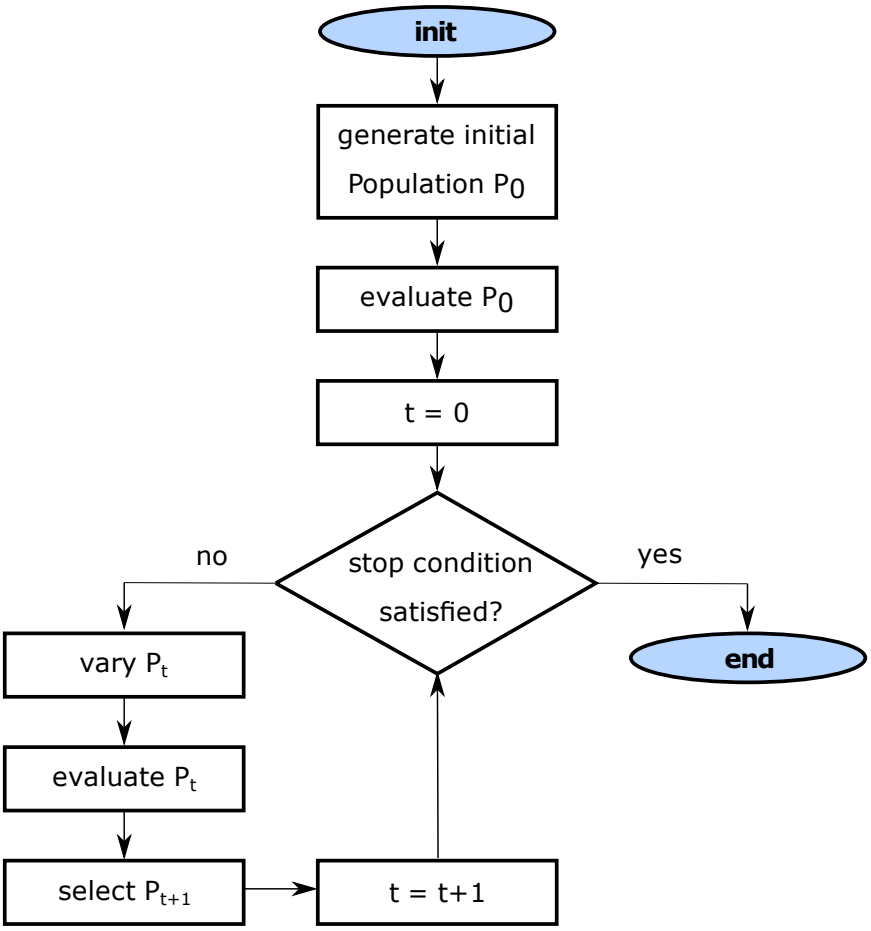

Figure 1.1: Basic flow chart of an EA.

of recombination is to discover better individuals than the original ones, or intermediate individuals that in future would allow to discover better ones.

- *Mutation operator*. This operator contributes to the diversity of the population. The recombination of progenitors by itself may not improve the population or may not discover new individuals. In these cases, some of the offsprings should be altered by other means. The mutation operator is responsible for securing that every individual from the search space is achievable. This operator is also used by the EA to evade from local optima.

- *Selection operator*. Based on a measure of adequacy of the individuals, this operator decides which individuals will be part of the next generation population.

EAs are highly parameterized algorithms, being their most important features introduced in the next subsections.

1.3.4.1. Individual Representation

The first step in defining an EA is to link the original problem context and the problem solving space where evolution takes place. Very importantly, it has to be clear what kind of solutions the original problem has. Then, the most appropriate domain for them is defined, and finally the most appropriate individual representation for it is used.

1.3.4.2. Initial Population

At the beginning of an EA, the population is empty. In order to fill it with individuals, a method to generate the initial population P_0 has to be defined. There is no standard method to initialize the population of an EA and usually P_0 is randomly generated. Also, an old population or a population from another heuristic could be used as P_0.

1.3.4.3. Variation Operators

The recombination and mutation operators are defined with the recombination (P_c) and mutation (P_m) rates, respectively. Through the use of the right values of P_c and P_m, the search space would be efficiently and extensively explored. A low P_c will not allow to explore intensely the search space, while a high P_m will avoid the convergence of the EA.

1.3.4.4. Fitness Function

The fitness function indicates the differences in quality among the individuals of the population. It gives a punctuation to each individual of the population. Given a minimization (or maximization) function, an individual x^q will get a lower (or greater) punctuation than other x^j if x^q is a better individual.

1.3.4.5. Selection Operator

The selection operator selects the fittest or the best punctuated individuals, which will be part of the population of the next generation P_{t+1}. Moreover, P_{t+1} must meet certain requirements, such as diversity and elitism.

Diversity The diversity of the population is a very important fact in complex optimization problems such as the one presented in this work. If all individuals in the population were located in the same space, for example if P_{t+1} were composed only of the fittest individuals, the procedure could converge prematurely to local optima. On the other hand, if P_{t+1} were composed of bad individuals, it would not converge at all. The selection operator controls the commitment between quality and diversity among individuals in the population in order to ensure a proper convergence. The fittest individuals are given a higher probability to take part in P_{t+1} than the worst individuals. Nevertheless, bad individuals also have a chance of being in P_{t+1}.

Elitism Since EAs are stochastic, the best individual found so far, x^{best}, may be lost during the evolving procedure. EAs introduce elitism to guarantee the presence of x^{best} in P_{t+1}. During the evolving procedure and at the end of the execution, x^{best} is always available.

1.3.4.6. Stop Condition

Another critical parameter in the EA definition is to decide when to stop it. For that purpose, one the following criteria should be fulfilled:

- *Global optimum solution achieved.* In this case, it makes no sense to continue searching for a better solution.
- *CPU cost.* In order to minimize the computational time, the EA execution can be restricted to a limited number of generations and evaluations of the fitness function.
- *Stagnation of the search.* The EA execution can be stopped after a limited number of generations if there is no improvement in the population. In this case, the population should be restarted, but keeping x^{best}.

1.3.5. Multi-objective Problems

In most practical situations, problems have several conflicting objectives. Parameter extraction procedure is only one of them. Problems of this kind are known as multi-objective problems (MOPs) [23]. The greatest difference between single objective problems and MOPs is the arrangement of the set of potential solutions. In a problem with n_{obj} competing objectives, each one of them is measured by an objective function $f_i(i = 1, \ldots, n_{obj})$. We can define a global objective function f that meets the following relations for two potential solutions for the problem s_1 and s_2

$$\begin{aligned} &f(s_1) = f(s_2) \Leftrightarrow f_i(s_1) = f_i(s_2)\ \forall i \in 1, 2, ..., n_{obj} \\ &f(s_1) \leq f(s_2) \Leftrightarrow f_i(s_1) \leq f_i(s_2)\ \forall i \in 1, 2, ..., n_{obj} \\ &f(s_1) < f(s_2) \Leftrightarrow f(s_1) \leq f(s_2) \wedge f(s_1) \neq f(s_2) \end{aligned} \tag{1.2}$$

Taking into account the above relations, the Pareto-dominance criterion can be used to establish an order between the individuals of the population [24]:

$$\begin{aligned} &s_1 \prec s_2 \Leftrightarrow f(s_1) < f(s_2) \\ &s_1 \preceq s_2 \Leftrightarrow f(s_1) \leq f(s_2) \\ &s_1 \sim s_2 \Leftrightarrow f(s_1) \not\leq f(s_2) \wedge f(s_2) \not\leq f(s_1) \end{aligned} \tag{1.3}$$

where $s_1 \prec s_2$ (s_1 dominates s_2) means that s_1 is a better solution than s_2, $s_1 \preceq s_2$ (s_1 weakly dominates s_2) means that s_1 is a better or equal solution than s_2, and $s_1 \sim s_2$ (s_1 is indifferent to s_2) means that

both solutions are not comparable. A Pareto-optimum solution s_{opt} [24] is defined as a solution which cannot be dominated by any other solution in the solution set S:

$$\nexists s_i \in S : s_i \prec s_{\text{opt}} \tag{1.4}$$

All Pareto-optimum solutions compose the Pareto front. The solutions of the Pareto front are indifferent to each other and equally valid. Thus, the criteria of the final users or experts will decide which solutions from the Pareto front are the best.

1.3.6. Multi-objective Evolutionary Algorithms

The combined use of EAs and the Pareto-dominance criterion gives rise to a special type of EAs, called Multi-objective Evolutionary Algorithms (MOEAs), capable of managing MOPs. MOEAs follow the same principles of EAs (described in Fig. 1.1) but including the mechanisms needed to operate with MOPs.

There are many ways of implementing a MOEA [25–28]. The Non-dominated Sorting Genetic Algorithm II (NSGA-II) [25] has been used successfully in a wide variety of problems and also employed in this thesis. The main objective of NSGA-II is to find a generation P_{t+1} of N individuals from a previous population P_t of N individuals also. The evolution between generations is developed with the selection, recombination and mutation operators and other criteria defined below.

- *Non-Dominated sort.* The population is sorted with the non-domination criterion. The individuals of the population are grouped in different fronts $F_i (i = 0, 1, ...)$, where i indicates the non-domination level, F_0 is the front of individuals dominating the rest of solutions, F_1 is the next front, only dominated by F_0, and so on.

- *Crowding distance.* It measures how close to its neighbors an individual is. In order to reduce the agglomeration of individuals, a large crowding distance is necessary. The control of this distance is used to improve the diversity of the population.

- *Selection operator.* NSGA-II uses the tournament selection operator [29]. This operator chooses randomly k individuals from P_t, and from these k individuals the one situated in the best front is selected. In the case that the k individuals are located in the same front, the one with the highest crowding distance is selected. This process is repeated until a population Q_t of N individuals is available. The population Q_t is transformed with the recombination and mutation operators. Finally a population R_t is built by joining P_t and Q_t, $R_t = P_t \cup Q_t$.

- *Elitism and population of the next iteration.* The population of the next generation P_{t+1} is formed with the individuals of the best fronts of R_t (truncating the number of individuals to N).

1.4. Structure of the Thesis

This thesis is divided in four main chapters that follow this introduction (Chapters 2-5). Each chapter can be read independently from each other and is provided with its own conclusion section. However, it is highly recommended to read first Chapter 2, since the rest of chapters mention it. In doing so, the reader can get a full understanding of the remaining chapters.

The first two chapters (Chapters 2 and 3) are focused on the definition of the evolutionary parameter extraction procedure applied to a generic compact model for OTFTs. Chapter 4 focus on compact modeling of organic phototransistors (OPTs). Finally, Chapter 5 is centered in the modeling of the contact region of OTFTs.

In Chapter 2 an evolutionary parameter extraction procedure is proposed. This procedure employs both a MOEA and a compact model, which in turn includes a model for the contact region, to extract the model parameters from the OTFT output characteristics. This evolutionary procedure always reaches a parameter set, provided that the search space of every parameter has been correctly defined.

In Chapter 3 the evolutionary procedure is extended in order to fulfill OTFT conductance requisites. These requisites are included in the extraction procedure in form of objectives and constraints, giving rise to a constrained many-objective evolutionary procedure. Again, this procedure is employed to extract the model parameters from experimental OTFT output characteristics, estimating a reliable parameter set capable of reproducing the device $I - V$ characteristics.

In Chapter 4, the compact model and the model of the contact region are extended to consider the effects of illumination on organic phototransistors (OPTs). The study of two devices under different illumination conditions confirms that the contact region of phototransistors is very sensitive to the photovoltaic and photoconductive effects. Due to this fact, not only the contact effects must be considered when a parameter extraction is performed, but also the effect of illumination on the contact region.

In Chapter 5, the functionality of the contact region model is fully expanded, giving rise to a standard semi-empirical contact model. Originally, the contact model was applied to devices in which the contacts are space-charge limited. By enlarging the range of values of a single parameter of this contact model, we can also extend the applicability of this model (and the evolutionary procedure) to devices in which the contacts are Schottky limited.

The memory ends with the global conclusions and recommendations for future work.

2

Evolutionary Parameter Extraction for an OTFT Compact Model including Contact Effects

2.1. Introduction

Organic thin-film transistors (OTFTs) have attracted considerable research interest because of the advantages associated to the materials used, such as flexibility, low fabrication costs and weight, and their potential applications in large-area, flexible electronics, such as displays and sensors [1]. Nevertheless, they also have important limitations, for example a low carrier mobility compared to inorganic TFTs ([1, 30, 31]), high process variability [32, 33], or degraded performance characteristics due to contact effects. Contact effects, specifically, have been extensively studied in order to introduce them in transistor compact models [2–4, 18, 34–38].

Compact models are analytical models that are able to reproduce the electrical behavior of a given device in all regions of operation. They are usually based on physical principles, with some free parameters that are used to stitch the transition between regions, or to improve the needed mathematical simplification of the underlying device physics. Thus, these models must be associated with methods to extract their respective parameters from the electrical characteristics of a transistor [3–5, 18, 34]. Parameter extraction procedures must assign a correct physical value to each parameter in order to keep their meaning. An invalid value would cause the parameter extraction procedure to fail or the achievement of an unphysical parameter set. Finally, the extracted parameter set has to provide a good agreement between the model and the experimental data. Typically, this parameter extraction is usually a two-step procedure, because the parameters are usually correlated. In a first step, a direct extraction method under some simplifying assumptions is used to obtain a first set of parameters. In a second step, this set may be used in a global optimization procedure.

In this chapter, we consider a compact model [4], which has been successfully tested in the past with different OTFTs operating in different regions [39–41] and even in transistors showing current-voltage curves with hysteresis [42]. The application of this model can also be found in two-dimensional field-effect transistors, in which contact effects degrade the device performance [43, 44]. A procedure that accelerates the extraction of the parameters of this model, or solves some of the problems noted in the past [45], would be very helpful. For this reason, in this chapter a multi-objective evolutionary parameter extraction procedure is proposed, solving the extraction shortcomings or weaknesses of the procedure proposed in [4].

Our procedure is based on a special kind of heuristic and optimization search technique called Evolutionary Algorithms (EAs) (introduced in Chapter 1, Section 1.3.4). EAs are employed in a broad range of engineering disciplines [46] such as architecture [47, 48], electrical [49, 50], chemical [51, 52] and mechanical engineering [53, 54]. EAs are also employed in other important fields as computer science [55], control [56] and signal processing [57]. Moreover, EAs have been previously used to extract the parameters of semiconductor devices, such as MOSFETs [50, 58–61], photovoltaic (PV) modules [62, 63], or solar cells [54, 62, 64]. They have even been used to extract parameters for simple OTFTs models [65–67], gaining in accuracy and speed. For these reasons, we propose to use EAs in combination with the procedure introduced in [4]. Nevertheless, the main novelty of our procedure is not only to extract the parameters of an OTFT's compact model, but to additionally obtain an adequate physical evolution of the contact current-voltage characteristics. The addition of this second objective into our

evolutionary procedure is what makes it different from previous algorithms in OTFTs.

This chapter is organized as follows. In Section 2.2, the features and possible limitations of the direct parameter extraction procedure proposed in [4], when applied to experimental data, are shown. Then, in Section 2.3, the evolutionary procedure is developed for the compact model [4]. In Section 2.4, the evolutionary procedure is tested with experimental data. Finally, the conclusions are presented in Section 2.5.

2.2. Theory

In [68, 69], a compact model was developed for OTFTs which includes the voltage drop at the source contact ($V_S \equiv V_C$) and electric field dependent mobility $\mu = \mu_0(V_G - V_T)^\gamma$:

$$\begin{aligned} I_D &= -k_0 \frac{W}{L} \frac{[(V_G - V_T - V_S)^{\gamma+2} - (V_G - V_T - V_D)^{\gamma+2}]}{\gamma + 2}, \\ k_0 &= \mu_0 C_{ox}, \end{aligned} \tag{2.1}$$

where V_G is the gate voltage, V_D is the drain voltage, V_T is the threshold voltage, γ is the mobility enhancement factor, μ_0 is the mobility-related parameter and its dimension is expressed as $\mathrm{cm}^2/(\mathrm{V}^{1+\gamma}\mathrm{s})$, C_{ox} is the capacitance per unit area of the oxide and W and L are the channel width and length, respectively.

Later on, model (2.1) was redefined with the inclusion of a model for the contact region [4]:

$$V_S = \left(\frac{I_D}{M_C}\right)^{\frac{1}{m_k}}, \tag{2.2}$$

where the parameter M_C is usually gate voltage dependent and m_k indicates the grade of the observed trend (from linear to quadratic, $1 \leq m_k \leq 2$) in the triode region of the OTFT. In the case of a linear trend ($m_k = 1$), M_C would be equivalent to the inverse of a contact resistance R_C. When this occurs, the $I_D - V_S$ relation can be approximated by the usual linear relation

$$V_S = I_D R_C. \tag{2.3}$$

The more general expression (2.2) for the $I_D - V_S$ relation was proposed in order to include linear and non-linear relations as observed experimentally in OTFTs [70] and after theoretical studies on metal-organic contacts in which the transition from linear to quadratic trends was analyzed [3, 71].

Along with (2.1) and (2.2), the authors proposed a method to extract the parameters of (2.1) and the voltage drop at the contact $I_D - V_S$ from experimental $I_D - V_D$ curves [4]. The method makes use of the so-called H_{VG} function [68, 69], with the objective of getting an initial estimation of the values of γ and V_T. It is defined as the ratio of the integral of the drain current (I_D) over the gate bias divided

by the drain current

$$H_{VG}(V_G) = \frac{\int_{<V_T}^{V_G} I_D(V_G)\, dV_G}{I_D(V_G)}. \tag{2.4}$$

The H_{VG} function can be evaluated from experimental data measured in the linear and saturation regimes. Combining (2.1) and (2.4), a linear function with V_G is obtained for the saturation regime [69]

$$H_{VG}(V_G) = (V_G - V_T - V_S)/(\gamma + 3). \tag{2.5}$$

The linear expression (2.5) can be used to get an initial estimation of the values of γ and V_T incorporating the experimental values of H_{VG} and assuming V_S as a constant value, usually $V_S = 0$. However, V_S is a function of I_D and V_G ($V_S = V_S(I_D, V_G)$). Thus, the values of γ and V_T incorporate any inaccuracy coming from the assumed value of V_S. After this initial estimation of γ and V_T, if k_0 is also known, the voltage in the contacts $V_S(I_D, V_G)$ can be extracted by introducing the values of the experimental data I_D and the values of γ, V_T and k_0 in (2.1):

$$V_S = V_G - V_T - \left[I_D(\gamma + 2)L/(Wk_0) + (V_G - V_T - V_D)^{\gamma+2}\right]^{1/(\gamma+2)}. \tag{2.6}$$

Since the k_0 value is unknown, various values are tested and introduced in (2.6) to find the relation $I_D - V_S$. The initial range of values for k_0 can vary by two orders of magnitude over and below the value obtained with the ideal MOS model applied to the experimental $I_D - V_G$ data in the saturation regime. The obtained relation $I_D - V_S$ must have physical meaning according to (2.2). Only the values of k_0 that make the relation $I_D - V_S$ follow (2.2) are considered. An averaged value of the contact voltage obtained from this relation $I_D - V_S$ must be consistent with the initially assumed value of V_S in the above paragraph. Otherwise, this new averaged value of V_S must be inserted in (2.5) and the process must be repeated until these conditions are fulfilled.

Although the compact model along with the parameter extraction procedure have been successfully used in the past [4, 39–42], it has been noticed that the H_{VG} function may not always perform under certain circumstances:

- The values of γ and V_T extracted from (2.5) are inaccurate if $V_C \neq 0$.
- As initially defined in [72], the integral (2.4) must necessarily be evaluated from a gate voltage under the threshold voltage. Otherwise, the extracted values of γ and V_T will differ from the actual ones.
- The integral (2.4) performed with very few points (very few output characteristic curves) also leads to inaccurate values of γ and V_T.

In these cases, the errors in the values of V_T and γ can propagate through the next steps of the extraction procedure, providing a non-optimized parameter set $(k_0, \gamma, V_T, m_k, M_C)$.

An example of misuse of the H_{VG} function can be seen in the analysis of the output characteristics $I_D - V_D$ of Fig. 2.1. These curves have been generated using the compact model (2.1), the relation (2.2)

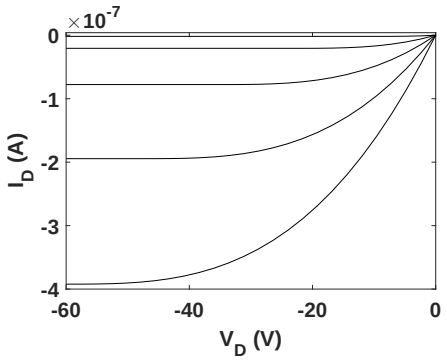

Figure 2.1: Output characteristics generated using the compact model (2.1) and the relation (2.2) at gate voltages V_G from 0 to $-50\,\mathrm{V}$ with a $-12.5\,\mathrm{V}$ step (from top to bottom). V_D is swept from 0 to $-60\,\mathrm{V}$ with a $-2.4\,\mathrm{V}$ step. $k_0 = 1.381 \times 10^{-14}\,\mathrm{A/V^{2+\gamma}}$, $W = 2 \times 10^{-1}\,\mathrm{cm}$, $L = 5.0 \times 10^{-4}\,\mathrm{cm}$, $V_T = 10\,\mathrm{V}$, $\gamma = 1$, $M_C(V_G) = \alpha|V_G - V_T|^{(\gamma+1)}\,\mathrm{V}^{m_k}$ with $\alpha = 5 \times 10^{-10}$, and $m_k = 1.2$. The contact voltage V_S in the saturation region at $V_D = -60\,\mathrm{V}$ for each curve is -0.06, -0.12, -0.17, -0.23, -0.28 V (from top to bottom).

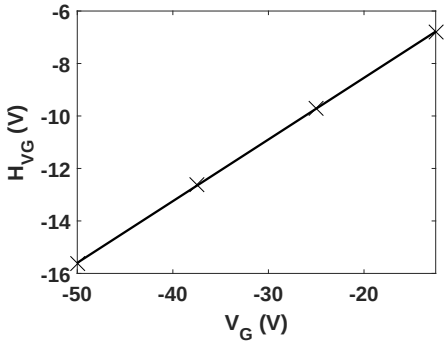

Figure 2.2: H_{VG} function evaluated from the $I_D - V_G$ relation extracted at $V_D = -60$ V from the output characteristics of Fig. 2.1 (symbols). The solid line is the fitting with (2.5) using $V_T = 16.35$ V and $\gamma = 1.25$.

and the bisection method [73]. Once the experimental data is available, H_{VG} is applied to the saturation region ($V_D = -60$ V). The result is represented with crosses in Fig. 2.2. After fitting the experimental H_{VG} function with (2.5), $V_T = 16.35$ V and $\gamma = 1.25$ are obtained. These values do not correspond with the V_T and γ values initially employed in Fig. 2.1, even for this case in which the contact voltage is much smaller than the drain voltage (values of the contact voltage are provided in Fig. 2.1). At this point, the parameter extraction procedure should be aborted since the following steps depend on the values extracted from the H_{VG} function.

It is clear that solutions to solve this problem at the experimental laboratory exist: it is easy to measure transfer curves or more output characteristics, and that some of these curves may correspond to gate voltages below the threshold voltage. However, there may be situations in which these solutions

are no longer possible or difficult to accomplish. In these cases, we propose to adapt the procedure in [4]. As alternative, an evolutionary parameter extraction procedure is proposed in Section 2.3.

2.3. Evolutionary Parameter Extraction Procedure

As stated in the introduction of this chapter, once a set of parameters has been determined by a direct method ([68, 69, 72, 74–76]), the parameter extraction can be improved by a global optimization process that takes into account possible interactions between the parameters. Different techniques can be used for this global optimization, which are usually hampered by the high dimensionality of the problem (the set of parameters to be extracted or optimized are usually composed of tens of elements). Initially, this was dealt with using deterministic methods, based on derivatives and local optimization [77, 78]. Soon after, more efficient techniques based on evolutionary algorithms were proposed ([50, 58–61, 79]). Alternative methods, although less used than evolutionary computing, have also been proposed, such as a procedure that introduces expert knowledge into the parameter extraction for an OTFT compact model [5], or the particle-swarm-optimization method employed to extract the model parameters of the PSP compact MOSFET model [80].

EAs are meta-heuristics based on natural and genetic evolution [21, 22]. In nature, there are entities or populations of individuals with the ability of reproduction. These individuals usually have different characteristics, such as height or strength. The offspring individuals inherit some characteristics of their progenitors. In addition, some of them may mutate acquiring new qualities. As time passes, only the individuals able to adapt to the environment survive, usually the fittest ones. Taking as reference the natural evolution, EAs process at each iteration a population of potential solutions (individuals) for a determined problem (environment). During the EA execution the potential solutions are combined (reproduction) and some of them may be altered (mutation), giving rise to an offspring population, in which the fittest potential solutions have the highest probability of remaining in it (adaptation to the environment).

Since EAs evolve a population or potential solutions for a problem, they are particularly well fitted to solve multi-objective problems (MOPs) [23], i.e., problems where several competing objectives must be optimized simultaneously. In this case, a multi-objective EA (MOEA) will return a set of Pareto-optimum solutions or Pareto front, composed of many solutions which are indifferent to each other and equally valid. Thus, the criteria of final users or experts will be needed in order to decide which solutions from the Pareto front are the best. There are many ways of implementing the MOEA concept [27, 28, 81, 82], with the Non-dominated Sorting Genetic Algorithm II (NSGA-II) [81] being the most widely used. However, since NSGA-II is a generic multi-objective optimization procedure (see Chapter 1, Section 1.3.6) as all MOEAs, it must be adapted to the concrete problem being solved. In our case, its adaptation for extracting the parameters for an organic TFT compact model including the contact effects is detailed below.

2.3.1. Individual Representation

Our procedure is based on a set of experimental data $I_D = I_D(V_{G_i}, V_{D_j})$, where $i \in \mathbb{Z} : 1 \leq i \leq g$ and $j \in \mathbb{Z} : 1 \leq j \leq d$. The numerical estimation of I_D with (2.1)-(2.2), and the voltage drop at the contact region V_S with (2.6) are named $\widehat{I_D}(V_{G_i}, V_{D_j}, x)$ and $\widehat{V_S}(V_{G_i}, V_{D_j}, x)$, respectively, where x refers to the set of parameters needed to compute (2.1), (2.2) and (2.6) and is defined as the individual of the population:

$$x = (k_0, \gamma, V_T, M_C(V_{G_1}), ..., M_C(V_{G_g})), \tag{2.7}$$

where g is the number of different V_G values employed to generate I_D, $M_C(V_{G_i})$ is the estimation of $M_C(V_G)$ at these particular values of V_G and the number of variables l of the individual (2.7) is $p = g+3$ ($l \in \mathbb{Z} : 1 \leq l \leq p$).

The parameter m_k controls the linearity of the $I_D - V_S$ curves and does not depend on the gate voltage [4, 42]. A simple inspection of the output characteristics in the triode region can provide a first estimation of m_k. Intentionally, the parameter m_k does not form part of the individual (2.7), but will be a static predefined parameter of the evolutionary procedure. The reason is that the joint use of m_k and the $M_C(V_G)$ in (2.7) could cause the no-convergence to an acceptable solution.

2.3.2. Recombination Operator

The SBX operator is employed in the recombination operation for its successful performance at continuous search spaces [83, 84]. All individuals of the population Q_t, previously selected from P_t, participate in the recombination process, but only half ($P_c = 0.5$) of the variables of an individual will be recombined. This operator takes randomly from the population $N/2$ pairs of parent individuals x^j and x^q, which give place to two offspring individuals c^j and c^q. Each variable l of both parents is recombined if a random number u taken within [0,1] is greater than P_c. In the opposite case, the variable l of each offspring individual will be a copy of the variable l of a respective progenitor. In the first case, each offspring variable is symmetrically calculated as

$$c_l^j = \bar{x}_l - \frac{1}{2}\beta(x_l^q - x_l^j), \tag{2.8}$$

$$c_l^q = \bar{x}_l + \frac{1}{2}\beta(x_l^q - x_l^j), \tag{2.9}$$

where $\bar{x}_l = (x_l^j + x_l^p)/2$ and β is a polynomial distribution controlled by a parameter η_c. The parameter η_c controls how far the offspring individuals are generated away from its progenitors.

2.3.3. Mutation Operator

After the creation of offspring individuals, they are mutated in order to improve convergence and also to allow escaping from local optima. This mutation is performed with the Polynomial Mutation

operator, successfully used in many problems and easily controlled by its mutation parameters [85, 86]. The generation of a mutated individual x from an offspring individual c is also controlled by a polynomial probability distribution. Each variable l of the mutated individual x is created as

$$x_l = \begin{cases} c_l + \delta_L(c_l - c_l^{(L)}), & \text{if } u \leq 0.5 \\ c_l + \delta_R(c_l^{(U)} - c_l), & \text{if } u > 0.5 \end{cases} \tag{2.10}$$

where u is a random number generated within [0, 1], and δ_L and δ_R are the polynomial distributions, both controlled by a parameter η_m. Both distributions are modified, so that no value outside the specified range $[c_l^{(L)}, c_l^{(U)}]$ is created by this operator.

This operator generates individuals close to the offspring with a higher probability than individuals far away from it. This is done by considering that each variable l of an offspring individual c of length p has a probability $1/p$ of being mutated.

2.3.4. Fitness Function

The fitness function assigns a fitness value to each individual x for each one of the objectives defined in a MOP. In our MOP, two objectives have been defined for the individual (2.7): (i) to minimize the error between the experimental values of $I_D(V_{G_i}, V_{D_j})$ and their estimation from (2.1)-(2.2) $\widehat{I_D}(V_{G_i}, V_{D_j}, x)$, and (ii) to minimize the error between the voltage drops at the contact region $V_S(V_{G_i}, V_{D_j}, x)$ extracted from (2.2) and their estimation $\widehat{V_S}(V_{G_i}, V_{D_j}, x)$ extracted from (2.6).

The *Normalized Root Mean Squared Error* (NRMSE) is used to estimate these errors [87]:

$$\text{NRMSE}(y, \hat{y}) = \sqrt{\frac{\sum_{z=1}^{w}(y_z - \hat{y}_z)^2}{\sum_{z=1}^{w}(y_z - \bar{y})^2}}, \tag{2.11}$$

where y represents the data set that we want to accurately approximate, $\hat{y}$ is the estimation of y, w is the number of data samples in y, and $\bar{y}$ is the mean value of the complete data set y. Thus, the fitness function f is defined as $f = (f_1, f_2)$, where

$$\begin{aligned} f_1(x) &= \text{NRMSE}\left(I_D(V_{G_i}, V_{D_j}), \widehat{I_D}(V_{G_i}, V_{D_j}, x)\right), \\ f_2(x) &= \text{NRMSE}\left(V_S(V_{G_i}, V_{D_j}, x), \widehat{V_S}(V_{G_i}, V_{D_j}, x)\right), \\ &\forall i \in \mathbb{Z} : 1 \leq i \leq g, \forall j \in \mathbb{Z} : 1 \leq j \leq d \end{aligned} \tag{2.12}$$

2.3.4.1. $I_D(V_{G_i}, V_{D_j})$

$I_D(V_{G_i}, V_{D_j})$ is the experimental value of the drain current.

2.3.4.2. $\widehat{I_D}(V_{G_i}, V_{D_j}, x)$

$\widehat{I_D}(V_{G_i}, V_{D_j}, x)$ is the estimation of $I_D(V_{G_i}, V_{D_j})$ extracted from the compact model (2.1)-(2.2) using the bisection method [73]. This procedure starts with an initial interval $[a_i, b_i]$ in which the value of $\widehat{I_D}(V_{G_i}, V_{D_j}, x)$ is expected. This interval may be different for each value of V_{G_i}. The interval is shortened to the half in successive iterations until an adequate value for $\widehat{I_D}(V_{G_i}, V_{D_j}, x)$ is obtained.

Starting at iteration $t = 0$, and assuming that $a_{ij_0} = a_i$ and $b_{ij_0} = b_i$, three values are considered in each iteration t for all possible combinations of i and j:

$$\begin{aligned}
\widehat{I_{D_{a,t}}}(V_{G_i}, V_{D_j}, x) &= a_{ij_t}, \\
\widehat{I_{D_{b,t}}}(V_{G_i}, V_{D_j}, x) &= b_{ij_t}, \\
\widehat{I_{D_{c,t}}}(V_{G_i}, V_{D_j}, x) &= c_{ij_t} = (a_{ij_t} + b_{ij_t})/2.
\end{aligned} \tag{2.13}$$

For each one of these values, V_S is calculated using (2.2) and the different values of $M_C(V_{G_i})$ coded in x:

$$\begin{gathered}
V_{S_{k,t}}(V_{G_i}, V_{D_j}, x) = \left(\frac{\widehat{I_{D_{k,t}}}(V_{G_i}, V_{D_j})}{M_C(V_{G_i})} \right)^{\frac{1}{m_k}}, \\
\forall i \in \mathbb{Z} : 1 \leq i \leq g, \forall j \in \mathbb{Z} : 1 \leq j \leq d, k \in \{a, b, c\}
\end{gathered} \tag{2.14}$$

Then, the differences between each one of the three possible estimations $k \in \{a, b, c\}$ of I_D in the current iteration and the value returned by the compact model (2.1) are calculated:

$$\begin{aligned}
r_{k,ij_t} = \widehat{I_{D_{k,t}}}(V_{G_i}, V_{D_j}) + \\
+ \frac{k_0 W \left(V_{G_i} - V_T - V_{S_{k,t}}(V_{G_i}, V_{D_j}) \right)^{\gamma+2}}{L(\gamma+2)} - \\
- \frac{k_0 W \left(V_{G_i} - V_T - V_{D_j} \right)^{\gamma+2}}{L(\gamma+2)}
\end{aligned} \tag{2.15}$$

As the bisection procedure tries to find a root in (2.15), the interval $[a_{ij_t}, b_{ij_t}]$ is shortened according to the values r_{a,ij_t}, r_{b,ij_t} and r_{c,ij_t} following the rule:

$$[a_{ij_{t+1}}, b_{ij_{t+1}}] = \begin{cases} [c_{ij_t}, b_{ij_t}], & \text{if } \operatorname{sign}(r_{a,ij_t}) = \operatorname{sign}(r_{c,ij_t}) \\ [a_{ij_t}, c_{ij_t}], & \text{otherwise} \end{cases} \tag{2.16}$$

This iterative process continues until the condition $|r_{c,ij_t}| < \varepsilon$ is reached or a maximum number of iterations are executed ($t = n_{\text{bisec}}$). In any case, the drain current is estimated as $\widehat{I_{D_{c,t}}}(V_{G_i}, V_{D_j}, x) = c_{ij_t}$.

2.3.4.3. $V_S(V_{G_i}, V_{D_j}, x)$

$V_S(V_{G_i}, V_{D_j}, x)$ is the voltage drop at the contact introducing in (2.2) the experimental value $I_D(V_{G_i}, V_{D_j})$ and the parameter $M_C(V_{G_i})$ coded in x:

$$V_S(V_{G_i}, V_{D_j}, x) = \left(\frac{I_D(V_{G_i}, V_{D_j})}{M_C(V_{G_i})}\right)^{\frac{1}{m_k}}. \tag{2.17}$$

2.3.4.4. $\widehat{V_S}(V_{G_i}, V_{D_j}, x)$

$\widehat{V_S}(V_{G_i}, V_{D_j}, x)$ is the voltage drop at the contact introducing in (2.6) the experimental value $I_D(V_{G_i}, V_{D_j})$ and the parameters k_0, γ and V_T coded in x:

$$\begin{aligned}\widehat{V_S}(V_{G_i}, V_{D_j}) = \; & V_{G_i} - V_T - \\ & - \left[I_D(V_{G_i}, V_{D_j})\frac{(\gamma+2)L}{Wk_0} + (V_{G_i} - V_T - V_{D_j})^{\gamma+2}\right]^{1/(\gamma+2)}.\end{aligned} \tag{2.18}$$

2.4. Results

In this section, two sets of experiments (A and B; and C_1, C_2 and D) are presented. These experiments have been carried out using an open source evolutionary tool called ECJ (A Java-based Evolutionary Computation Research System) [88]. Experiments A, B and C_2 have been executed in a CentOS cluster with 19 computation nodes, each one with two Intel Xeon E5520 processors at 2.7 GHz. Each execution set for a determined m_k was executed sequentially using only one node. Experiments C_1 and D have been executed in an Ubuntu laptop with an Intel i5-3320M processor at 2.6 GHz.

In the experiments A and B, the evolutionary parameter extraction procedure is applied to solve the problem presented at the end of Section 2.2 and Figs. 2.1 and 2.2, in which the H_{VG} function was not provided with the appropriate input data. In experiment A a parameter set is extracted from Fig. 2.1, while in experiment B this extracted parameter set is optimized. Since the parameter set employed to generate the curves from Fig. 2.1 is known, it can be used along with the fulfillment of $f(x)$ (2.12) to verify the validity of the evolutionary procedure as a parameter extraction method in OTFTs. Experiments C_1, C_2 and D, on the other hand, deal with the optimization and extraction of parameters of real OTFT devices [40, 89, 90]. In Experiments C_1 and C_2, a solution for the parameter set is also known [40, 90], which can be compared against our results to test the effectiveness of our procedure.

2.4.1. Experiment A: Parameter Extraction

Once the set of experimental data is available (curves in Fig. 2.1), the parameters of the evolutionary procedure are defined.

First. As seen in Fig. 2.1, V_D is swept from 0 to -60 V with a -2.4 V step and V_G is swept from 0 to -50 V with a -12.5 V step. That is, $V_{G_1} = 0$ V, $V_{G_2} = -12.5$ V, $V_{G_3} = -25$ V, $V_{G_4} = -37.5$ V and $V_{G_2} = -50$ V.

Second. The search space is defined in order to guide the search to an optimum solution. For this problem, the parameter ranges of each individual x of the population are:

Table 2.1: NSGA-II execution parameters used in the different experiments.

	Experiment				
Parameter	A	B	C_1	C_2	D
N	500	500	500	500	500
n_{job}	10	10	10	10	10
n_{iter}	50000	50000	5000	5000	50000
p	8	8	9	8	9
P_m	0.125	0.125	0.1111	0.125	0.1111
P_c	0.5	0.5	0.5	0.5	0.5
η_c	20	20	20	20	20
η_m	20	20	20	20	20

Table 2.2: Bisection method parameters used in the different experiments.

	Experiment			
Param.	*A and B*	C_1	C_2	D
ε	10^{-15}	10^{-15}	10^{-15}	10^{-15}
n_{bisec}	1000	1000	1000	1000
$[a_1, b_1]$ (A)	$[0, -10^{-6}]$	$[0, -10^{-8}]$	$[0, -10^{-8}]$	$[0, -10^{-6}]$
$[a_i, b_i]$ (A), $i \neq 1$	$[0, -10^{-6}]$	$[0, -10^{-8}]$	$[0, -10^{-6}]$	$[0, -10^{-6}]$

$$\begin{gathered} k_0 \in [10^{-16}, 10^{-10}]\,\mathrm{A/V}^{(2+\gamma)};\ \gamma \in [0, 2]; \\ V_T \in [-30, 30]\,\mathrm{V};\ M_C(V_{G_i}) \in [10^{-10}, 10^{-4}]\,\mathrm{A/V}^{m_k}. \end{gathered} \tag{2.19}$$

As justified in Section 2.3.1, the parameter m_k is considered a static predefined parameter. Eleven cases are analyzed, in which m_k is swept from 1.0 to 2.0 with a 0.1 step.

Third. Since EAs are meta-heuristics, each execution of our evolutionary procedure to extract the device parameters may return a different result, thereby the NSGA-II is executed n_{job} times for every m_k value, delimiting each one of them to n_{iter} iterations, being the initial N individuals randomly generated. In order to define the value of N, n_{job} and n_{iter} (Table 2.1) several trial-and-error tests are carried out. A compromise between the quality of the result and the computational cost needed to obtain it must be achieved. We observed that increasing the value of the parameters N and n_{iter} accurate results are obtained. However, it increases considerably the computational cost and in addition, the increment of the values of N or n_{iter} does not always ensure a quality increment of the final result, since for example the evolutionary procedure might converge to a local optimum. In those cases in which the evolutionary procedure always tends to converge to a local optimum, the mutation operators will help escaping from it, but with an increased execution time.

The values of η_c and η_m (Table 2.1) are standard values that have been tested successfully, and also

Table 2.3: Mean ± standard deviation of f_1 and f_2 objectives for each Pareto front related to a different m_k value.

m_k	f_1	f_2
1.0	$1.18 \times 10^{-2} \pm 8.0 \times 10^{-4}$	$3.38 \times 10^{-1} \pm 7.06 \times 10^{-2}$
1.1	$2.98 \times 10^{0} \pm 2.2 \times 10^{+1}$	$3.42 \times 10^{-1} \pm 1.24 \times 10^{-1}$
1.2	$7.00 \times 10^{-4} \pm 1.0 \times 10^{-4}$	$9.75 \times 10^{-1} \pm 5.19 \times 10^{-1}$
1.3	$1.19 \times 10^{-2} \pm 4.0 \times 10^{-3}$	$4.35 \times 10^{-1} \pm 2.07 \times 10^{-1}$
1.4	$1.26 \times 10^{-2} \pm 4.1 \times 10^{-3}$	$1.51 \times 10^{0} \pm 0.84 \times 10^{-1}$
1.5	$1.20 \times 10^{-2} \pm 4.2 \times 10^{-3}$	$1.72 \times 10^{0} \pm 1.07 \times 10^{0}$
1.6	$6.20 \times 10^{-3} \pm 3.9 \times 10^{-3}$	$2.16 \times 10^{0} \pm 1.19 \times 10^{0}$
1.7	$1.01 \times 10^{-2} \pm 6.3 \times 10^{-3}$	$1.76 \times 10^{0} \pm 9.73 \times 10^{-1}$
1.8	$1.19 \times 10^{-2} \pm 6.3 \times 10^{-3}$	$1.37 \times 10^{0} \pm 7.20 \times 10^{-1}$
1.9	$5.30 \times 10^{-3} \pm 3.7 \times 10^{-3}$	$2.24 \times 10^{0} \pm 1.16 \times 10^{0}$
2.0	$1.08 \times 10^{-2} \pm 8.9 \times 10^{-3}$	$1.86 \times 10^{0} \pm 1.01 \times 10^{0}$

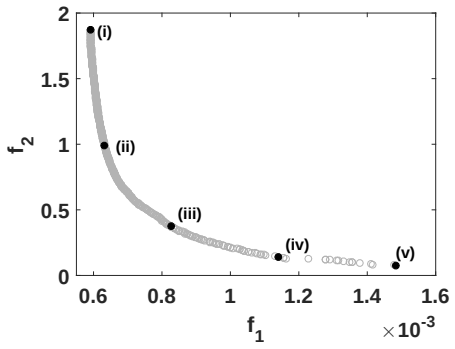

Figure 2.3: Pareto front selected as best result of the evolutionary procedure execution. It corresponds to $m_k = 1.2$. The parameters of the Pareto-optimum solutions enumerated from (i) to (v) and marked in black are found in Table 2.5. The current-voltage curves corresponding to these five solutions are represented in Fig. 2.4.

incorporated in the ECJ evolutionary tool.

Fourth. The parameters needed to carry out the bisection method for the computation of the fitness function are presented in Table 2.2. For this experiment, we use the same initial interval $[a_i, b_i]$ for each V_{G_i}.

Fifth. The evolutionary parameter extraction procedure is finally executed. At the end of the evolutionary process execution, a set of n_{job} Pareto fronts are obtained for every m_k value. In order to discard non-optimum solutions, the expert or final user should choose the best Pareto front associated with each m_k value, discarding the remaining $(n_{job} - 1)$ Pareto fronts. At this point, there should be as

Table 2.4: Mean ± standard deviation of the estimated parameters which compose the Pareto front represented in Fig. 2.3. (k_0 is in A/V$^{2+\gamma}$, V_T in V and $M_C(V_G)$ in A/V^{m_k})

x	Value
k_0	$1.59 \times 10^{-14} \pm 8.84 \times 10^{-29}$
γ	$9.65 \times 10^{-1} \pm 1.50 \times 10^{-3}$
V_T	$9.55 \times 10^{0} \pm 2.07 \times 10^{-2}$
$M_C(0V)$	$9.86 \times 10^{-5} \pm 2.63 \times 10^{-6}$
$M_C(-12.5V)$	$1.24 \times 10^{-6} \pm 8.88 \times 10^{-7}$
$M_C(-25V)$	$9.90 \times 10^{-7} \pm 4.28 \times 10^{-7}$
$M_C(-37.5V)$	$2.21 \times 10^{-6} \pm 1.17 \times 10^{-6}$
$M_C(-50V)$	$8.65 \times 10^{-6} \pm 8.54 \times 10^{-6}$

many Pareto fronts as different m_k values are available, being each one of them associated with its own m_k value. In order to have an idea about the distribution of the different Pareto-optimum solutions, their mean and standard deviation are calculated and shown in Table 2.3. Table 2.3 shows that in most of the cases the procedure finds accurate solutions for f_1 while the results for f_2 cannot be considered as accurate as expected. Analyzing the mean and standard deviation values calculated for the f_2 objective, the m_k cases from 1.4 to 2.0 (both included) are discarded as possible search starting points because of their high f_2 mean and standard deviation values. The $m_k = 1.1$ case is also discarded because the f_1 mean and standard values are not as accurate as expected. All the rest m_k cases have similar f_2 mean values. Among these three last cases, $m_k = 1.2$ is the best option as the search starting point, since it has the most accurate f_1 mean value. In order to confirm whether this decision is correct or not, we use graphical representations and distributed statistics to study the obtained parameter sets. The Pareto front associated with the chosen m_k value is represented in Fig. 2.3 while the statistics associated with its estimated parameter sets are represented in Table 2.4.

Since the Pareto front from Fig. 2.3 is composed by too many Pareto-optimum solutions, only five of them are selected (enumerated black points in Fig. 2.3) (note that all the Pareto-optimum solutions that compose a determined Pareto front are indifferent to each other and equally valid). The $I_D - V_D$ and $I_D - V_C$ curves associated to these five solutions are represented in Fig. 2.4 . As we can see in Fig. 2.3, each Pareto-optimum solution returns a different couple of values for the fitness function $f = (f_1, f_2)$. If we explore the different Pareto-optimum solutions from left to right along their Pareto front, the f_1 values worsen while the f_2 values improve. Solution (i) has the best f_1 value (minimization), however it has the worst f_2 value of the Pareto front. In the opposite case, solution (v) has the best f_2 value but the worst f_1 value of the complete Pareto-optimum solution set.

In order to confirm the differences between the different Pareto-optimum solutions of the Pareto front, the estimated parameters of the Pareto-optimum solutions from Fig. 2.4 are represented in Table 2.5. This table shows that the different values of the parameters k_0, γ and V_T are very close to each other. This fact along with the good agreement shown with the $I_D - V_D$ curves help us to confirm that in these

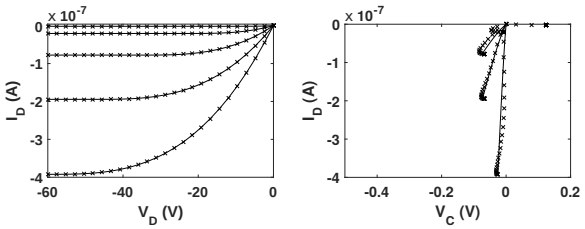

(I) $f = (5.90 \times 10^{-4}, 1.86)$

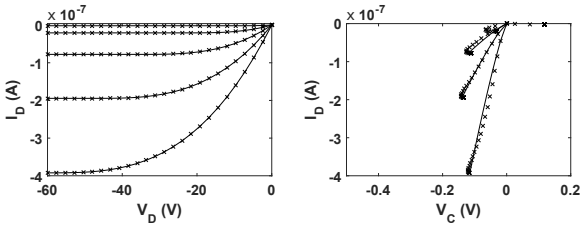

(II) $f = (6.32 \times 10^{-4}, 9.9 \times 10^{-1})$

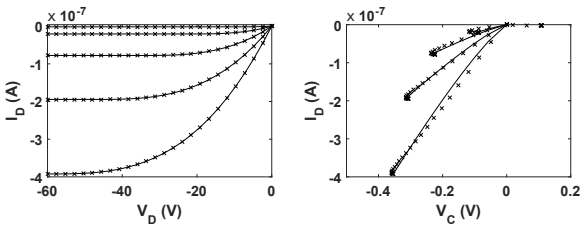

(III) $f = (8.26 \times 10^{-4}, 3.78 \times 10^{-1})$

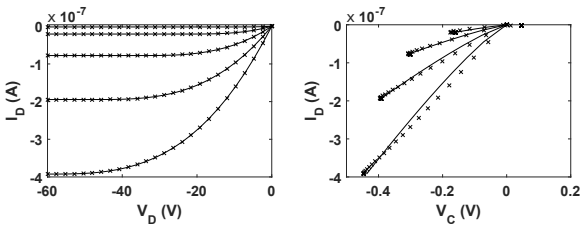

(IV) $f = (1.14 \times 10^{-3}, 1.41 \times 10^{-1})$

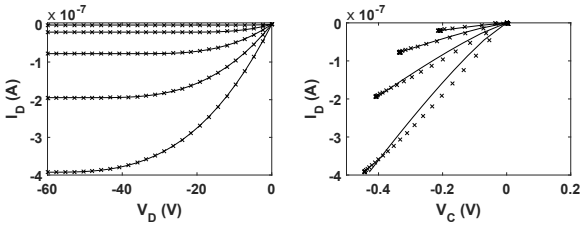

(V) $f = (1.48 \times 10^{-3}, 7.83 \times 10^{-2})$

Figure 2.4: Output characteristics and contact $I-V$ curves for the five Pareto-optimum solutions marked in Fig. 2.3. I_D and $\widehat{V_C}$ are represented with symbols and $\widehat{I_D}$ and V_C in solid lines. V_G is swept from 0 to $-50\,\mathrm{V}$ with a $-12.5\,\mathrm{V}$ step (from top to bottom in each figure).

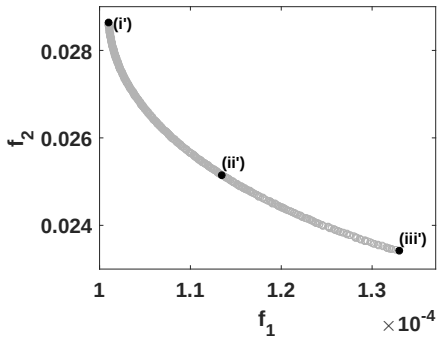

Figure 2.5: Pareto front selected as best result of the optimization execution. The parameters of the Pareto-optimum solutions enumerated from (*i'*) to (*iii'*) and marked in black are found in Table 2.8. The current-voltage curves corresponding to these three solutions are represented in Fig. 2.6.

cases the evolutionary procedure converges. However, the solutions (*i*), (*ii*) and (*iii*) provide a poor agreement with the $I_D - V_C$ curves, which is directly related with $M_C(V_G)$. Note that both positive and negative values for the contact voltage are obtained at low currents for the (*i*), (*ii*) and (*iii*) cases of Fig. 2.4, while only negative values are allowed.

Since all the solutions are considered equivalent in the Pareto-optimum solution set, an expert opinion is compulsory. Based on our expert judgment, together with the facts exposed previously, solution (*v*) with $f = (1.48 \times 10^{-3}, 7.83 \times 10^{-2})$ has been selected as final solution. This solution is represented in Fig. 2.4v and its estimated parameter set is shown in Table 2.6 along with its relative error (RE). Comparing the values of the estimated parameter set shown in Table 2.6 and the original values, we conclude that the procedure is able to find accurate values for V_T and γ, solving the problem that appears when the H_{VG} function is provided with an improper set of experimental data. Also, the extracted value of k_0 is considered as valid. However the extracted $M_C(V_G)$ set differs considerably from the original $M_C(V_G)$ set despite a good agreement with the $I_D - V_S$ curves is apparently obtained.

A further study of Fig. 2.3 shows that the obtained solutions are not spread evenly along the Pareto front, observing empty areas. This fact together with the low quality of some solutions (reasons exposed previously for solutions (*i*), (*ii*) and (*iii*)), make us think that a new search around a better known starting point could help us to get to a more accurate parameter set. In the next section, the evolutionary procedure is again executed, but this time using solution (*v*) as initial starting point, and applying the evolutionary procedure as optimization method.

2.4.2. Experiment B: Parameter Optimization

The use of the evolutionary procedure as an optimization method implies to work with an initial set of values for the fitting parameters. The search space domain must be defined around these initial values. The previous analysis showed that the f_2 function is more sensitive to variations of the fitting parameters, i.e. the $I_D - V_S$ curves are more sensitive than the $I_D - V_D$ curves to variations in the

Table 2.5: Estimated parameters of the Pareto-optimum solutions marked with black points in Fig. 2.3 and represented in Fig. 2.4 (k_0 is in $\mathrm{A/V^{2+\gamma}}$, V_T in V and $M_C(V_G)$ in $\mathrm{A/V^{m_k}}$).

	Pareto-optimum Solutions				
x	(i)	(ii)	(iii)	(iv)	(v)
k_0	1.5×10^{-14}	1.5×10^{-14}	1.5×10^{-14}	1.5×10^{-14}	1.5×10^{-14}
γ	9.6×10^{-1}	9.6×10^{-1}	9.6×10^{-1}	9.6×10^{-1}	9.6×10^{-1}
V_T	9.5×10^{0}	9.5×10^{0}	9.5×10^{0}	9.5×10^{0}	9.6×10^{0}
$M_C(0V)$	9.9×10^{-5}	9.9×10^{-5}	9.9×10^{-5}	9.9×10^{-5}	9.9×10^{-5}
$M_C(-12.5V)$	3.4×10^{-6}	1.0×10^{-6}	3.5×10^{-7}	1.7×10^{-7}	1.3×10^{-7}
$M_C(-25V)$	1.7×10^{-6}	9.9×10^{-7}	4.4×10^{-7}	3.1×10^{-7}	2.8×10^{-7}
$M_C(-37.5V)$	4.4×10^{-6}	2.0×10^{-6}	7.7×10^{-7}	5.9×10^{-7}	5.7×10^{-7}
$M_C(-50V)$	3.1×10^{-5}	5.2×10^{-6}	1.3×10^{-6}	1.0×10^{-6}	1.0×10^{-6}

Table 2.6: Final solution of the evolutionary procedure, original parameter set employed and the RE of the chosen final solution, (v) in Fig. 2.4 (k_0 is in $\mathrm{A/V^{2+\gamma}}$, V_T in V and $M_C(V_G)$ in $\mathrm{A/V^{m_k}}$).

x	Original Value	Estimated Value	RE (%)
k_0	1.38×10^{-14}	1.59×10^{-14}	$1.57\times10^{+1}$
γ	1.00×10^{0}	9.67×10^{-1}	3.22×10^{0}
V_T	$1.00\times10^{+1}$	9.65×10^{0}	3.40×10^{0}
$M_C(0V)$	5.00×10^{-8}	9.99×10^{-5}	$1.99\times10^{+5}$
$M_C(-12.5V)$	2.53×10^{-7}	1.34×10^{-7}	$4.70\times10^{+1}$
$M_C(-25V)$	6.12×10^{-7}	2.88×10^{-7}	$5.28\times10^{+1}$
$M_C(-37.5V)$	1.12×10^{-6}	5.78×10^{-7}	$4.87\times10^{+1}$
$M_C(-50V)$	1.80×10^{-6}	1.08×10^{-6}	$3.97\times10^{+1}$

transistor parameters, in particular the M_C set. Then, the search space domains for the k_0, γ and V_T parameters are reduced, but not for the $M_C(V_G)$ set. This will prevent the search from falling into a local optimum solution. The value of m_k is also fixed to 1.2 (as above). Thus, the parameter ranges are

$$\begin{gathered} k_0 \in [10^{-14}, 10^{-13}]\,\mathrm{A/V^{(2+\gamma)}};\ \gamma \in [0.8, 1.1]; \\ V_T \in [8.5, 11.0]\,\mathrm{V};\ M_C(V_{G_i}) \in [10^{-10}, 10^{-4}]\,\mathrm{A/V^{m_k}}. \end{gathered} \tag{2.20}$$

Once the evolutionary procedure is executed with these new parameter ranges, a new set of n_{job} Pareto fronts is obtained, and the best one is selected (Fig. 2.5). The mean and standard deviation of the estimated parameters of the Pareto-optimum solutions of Fig. 2.5 are shown in Table 2.7. The optimization execution improves clearly the previous solution, confirming that the evolutionary procedure helps to optimize previous OTFT parameter sets by exploring the search space around them. In particular, there is a noticeable improvement in the standard deviation of the $M_C(V_G)$ set (compare

Table 2.7: Mean ± standard deviation of the estimated parameters which compose the Pareto-optimum solutions in Fig. 2.5 (k_0 is in A/V$^{2+\gamma}$, V_T in V and $M_C(V_G)$ in A/V^{m_k}).

x	Value
k_0	$1.41 \times 10^{-14} \pm 1.40 \times 10^{-21}$
γ	$9.93 \times 10^{-1} \pm 3.55 \times 10^{-10}$
V_T	$9.91 \times 10^{0} \pm 2.97 \times 10^{-3}$
$M_C(0V)$	$1.32 \times 10^{-7} \pm 1.65 \times 10^{-8}$
$M_C(-12.5V)$	$2.88 \times 10^{-7} \pm 8.96 \times 10^{-9}$
$M_C(-25V)$	$6.41 \times 10^{-7} \pm 1.25 \times 10^{-8}$
$M_C(-37.5V)$	$1.19 \times 10^{-6} \pm 1.77 \times 10^{-8}$
$M_C(-50V)$	$1.98 \times 10^{-6} \pm 2.41 \times 10^{-8}$

Tables 2.4 and 2.7). This improvement is also seen in the current-voltage curves generated with the new solution.

As it happened before, the Pareto Front of Fig. 2.5 is composed by many Pareto-optimum solutions. Once again, the graphical representation of some of the solutions helps to select the best one. The current-voltage curves of three solutions extracted from Fig. 2.5 (black points and enumerated from (*i*') to (*iii*')) are represented in Fig. 2.6. Their estimated parameters are found in Table 2.8. Following the expert criteria and examining the information provided by Table 2.8 and Fig. 2.6, solution (*i*') is selected as the final solution of the evolutionary procedure, with $f = (1.01 \times 10^{-4}, 2.86 \times 10^{-2})$ (along with $m_k = 1.2$). The estimated parameter set of this solution is represented in Table 2.9 along with the original parameter set and its RE. If Tables 2.6 and 2.9 are compared, the solution in Table 2.9 is closer to the original parameter set than the one in Table 2.6.

The improvement shown in Table 2.9 is confirmed in the representation of the output characteristics and contact current-voltage curves of Fig. 2.6i', in which a better agreement between experimental and estimated curves is observed. In addition, for this selected solution (i'), transfer characteristics are calculated in saturation and in triode regions (solid lines in Fig. 2.6i'), and compared with the original values (symbols). Since the values of the contact parameter M_C are extracted for discreet values V_{G_i} (estimated M_C values from Table 2.9) a $M_C(V_G)$ relation is necessary to calculate the transfer characteristics shown in Fig. 2.6i'. Unless another relation is proposed, this relation is defined by carrying out a linear interpolation of the extracted $M_C(V_G)$ values. The resulting fittings of the output and transfer characteristics shown in Fig. 2.6i' confirm the success of the evolutionary procedure to optimize a previous solution.

2.4.3. Experimental Application

In the preceding sections, our evolutionary procedure has been successfully applied as a parameter extraction and as an optimization method to $I_D - V_D$ curves generated with model (2.1). In this section, these parameter optimization and parameter extraction methods are tested with three sets

Table 2.8: Estimated parameters of the Pareto-optimum solutions marked with black points in Fig. 2.5 and represented in Fig. 2.6 (k_0 is in A/V$^{2+\gamma}$, V_T in V and $M_C(V_G)$ in A/V^{m_k}).

	Pareto-optimum Solutions		
x	(i')	(ii')	(iii')
k_0	1.41×10^{-14}	1.41×10^{-14}	1.41×10^{-14}
γ	9.93×10^{-1}	9.93×10^{-1}	9.93×10^{-1}
V_T	9.91×10^{0}	9.91×10^{0}	9.92×10^{0}
$M_C(0V)$	1.63×10^{-7}	1.23×10^{-7}	1.04×10^{-7}
$M_C(-12.5V)$	3.03×10^{-7}	2.84×10^{-7}	2.72×10^{-7}
$M_C(-25V)$	6.61×10^{-7}	6.34×10^{-7}	6.16×10^{-7}
$M_C(-37.5V)$	1.22×10^{-6}	1.18×10^{-6}	1.15×10^{-6}
$M_C(-50V)$	2.01×10^{-6}	1.96×10^{-6}	1.93×10^{-6}

Table 2.9: Final solution of the optimization execution, original parameter set employed and RE of the chosen final solution, (i') in Fig. 2.6 (k_0 is in A/V$^{2+\gamma}$, V_T in V and $M_C(V_G)$ in A/V^{m_k}).

x	Original Value	Estimated Value	RE (%)
k_0	1.38×10^{-14}	1.41×10^{-14}	2.66×10^{0}
γ	1.00×10^{0}	9.93×10^{-1}	6.18×10^{-1}
V_T	1.00×10^{1}	9.91×10^{0}	8.71×10^{-1}
$M_C(0V)$	5.00×10^{-8}	1.63×10^{-7}	2.26×10^{2}
$M_C(-12.5V)$	2.53×10^{-7}	3.03×10^{-7}	2.00×10^{1}
$M_C(-25V)$	6.12×10^{-7}	6.61×10^{-7}	8.01×10^{0}
$M_C(-37.5V)$	1.12×10^{-6}	1.22×10^{-6}	8.21×10^{0}
$M_C(-50V)$	1.80×10^{-6}	2.01×10^{-6}	1.22×10^{1}

of experimental data measured in different OTFTs.

2.4.3.1. Parameter Optimization. Experiments C_1 and C_2

The objective of this subsection is to optimize previously extracted parameters of two OTFTs, an octadecyl substituted copper tetrabenzotriazaporphyrin (10CuTBTAP) OTFT [40] and a 1,4,8,11,15,18,22,25-octakis(hexyl)palladium phtalocyanine ($PdPc_6$) OTFT [90].

Experiment C_1: The 10CuTBTAP bottom-gate, bottom-contact OTFT was fabricated on octadecyltrichlorosilane treated 250-nm-thick SiO_2 gate insulator on the highly doped (resistivity 1 to 5 Ωcm) Si(110) substrate. A 70-nm-thick film of 10CuTBTAP was spin-coated onto photolithographically prepatterned 200-nm-thick gold source-drain electrodes in an interdigitated configuration with channel width $W = 2mm$ and length $L = 5\mu m$. The full protocols of the electrode deposition, substrate cleaning, and surface passivation were given in [40]. The electrical measurements were performed at room

Table 2.10: Parameter values of the previous and optimized solutions of the 10CuTBTAP OTFT (k_0 is in A/V$^{2+\gamma}$, V_T in V and $M_C(V_G)$ in A/V^{m_k}).

x	Previous Solution [40]	Optimized Solution
k_0	2.98×10^{-16}	2.75×10^{-16}
γ	1.63×10^{0}	1.99×10^{0}
V_T	$4.32 \times 10^{+1}$	$3.43 \times 10^{+1}$
$M_C(0V)$	$1.13 \times 10^{+9}$	$1.07 \times 10^{+9}$
$M_C(-10V)$	$6.05 \times 10^{+8}$	$6.95 \times 10^{+8}$
$M_C(-20V)$	$5.40 \times 10^{+8}$	$6.52 \times 10^{+8}$
$M_C(-30V)$	$5.70 \times 10^{+8}$	$6.84 \times 10^{+8}$
$M_C(-40V)$	$5.50 \times 10^{+8}$	$6.59 \times 10^{+8}$
$M_C(-50V)$	$4.90 \times 10^{+8}$	$5.75 \times 10^{+8}$

Table 2.11: Parameter values of the previous and optimized solutions of the $PdPc_6$ OTFT (k_0 is in A/V$^{2+\gamma}$, V_T in V and $M_C(V_G)$ in A/V^{m_k}).

x	Previous Solution [90]	Optimized Solution
k_0	3.00×10^{-12}	8.37×10^{-12}
γ	$1.60 \times 10^{+0}$	1.00×10^{0}
V_T	$9.44 \times 10^{+0}$	$1.08 \times 10^{+1}$
$M_C(-10V)$	2.50×10^{-9}	2.00×10^{-9}
$M_C(-20V)$	1.50×10^{-8}	1.37×10^{-8}
$M_C(-30V)$	3.70×10^{-8}	3.82×10^{-8}
$M_C(-40V)$	4.90×10^{-8}	5.28×10^{-8}
$M_C(-50V)$	6.80×10^{-8}	7.59×10^{-8}

temperature in air under ambient conditions.

The experimental $I_D - V_D$ curves of this transistor are represented with crosses in Fig. 2.7a. The optimization procedure defined for experiment C_1 is applied to the experimental data of Fig. 2.7a. The NSGA-II execution parameters are shown in Table 2.1 and the parameters of the bisection method in Table 2.2. The parameter set extracted in [40] is shown in Table 2.10 and is considered as the initial solution in the optimization procedure. In this case, $m_k = 1.0$ and the range defined for each parameter is

$$\begin{gathered} k_0 \in [2.5 \times 10^{-17}, 2.5 \times 10^{-15}]\ \mathrm{A/V}^{(2+\gamma)};\ \gamma \in [1.0, 2.0]; \\ V_T \in [25, 45]\ \mathrm{V};\ M_C(V_{G_i}) \in [10^8, 2 \times 10^9]\ \mathrm{A/V}^{m_k}. \end{gathered} \tag{2.21}$$

Once the evolutionary procedure is executed, the different Pareto fronts are analyzed and the best

solution (following an expert criteria) is selected. The values of the parameters which compose the chosen solution are shown in Table 2.10 (optimized solution). The fitness function of the result obtained in [40] is $f = (6.58 \times 10^{-2}, 9.92 \times 10^{-2})$ while the fitness function obtained with the evolutionary procedure is $f = (5.4 \times 10^{-2}, 7.1 \times 10^{-2})$. This means an improvement over the previous solution of 18.15 % for the f_1 objective ($I_D - V_D$ agreement) and 28 % for the f_2 objective ($I_D - V_S$ agreement). Although these percentages may not seem large enough, the improvement on the values of the transistor parameters is enormous. Note simply the variation in the threshold voltage of around 9 V from an initial value of 43 V. This optimization effort means a great advance in the accurate characterization of OTFTs.

The evolutionary procedure is also validated by comparing calculated $I_D - V_G$ curves in triode and saturation (solid lines in Fig. 2.7c) and experimental data ($\times$). A good agreement is observed. The $M_C(V_G)$ relation is built using the extracted M_C values from table Table 2.10.

Experiment C_2: The $PdPc_6$ transistor is a bottom gate bottom contact (inverted) OTFT with aspect ratio $W/L = 200$. It was fabricated using a 70nm thick spin coated film of $PdPc_6$ and 250nm thick silicon dioxide (SiO_2) as the active layer and the gate dielectric layer, respectively, on the highly doped Si (110) gate electrode. Titanium/gold thin films were used for the source/drain electrodes. The gate SiO_2 dielectric was passivated with an octadecyltrichlorosilane (OTS) self-assembled monolayer. The protocols of the substrate cleaning, electrode deposition, and surface passivation were given in [91].

The optimization procedure defined for experiment C_2 is applied to the experimental $I_D - V_D$ curves of Fig. 2.7d (crosses). The NSGA-II execution parameters are shown in Table 2.1 and the parameters of the bisection method in Table 2.2

The previous extracted parameter set [90] is shown in Table 2.11. Like in *Experiment* C_1, the search space will be defined around this known set of values. In this case, $m_k = 1.32$ and the range defined for each parameter is

$$\begin{aligned} &k_0 \in [6 \times 10^{-12}, 6 \times 10^{-8}]\,\mathrm{A/V}^{(2+\gamma)};\ \gamma \in [1.0, 2.0]; \\ &V_T \in [0, 20]\,\mathrm{V};\ M_C(V_{G_i}) \in [2 \times 10^{-9}, 10^{-7}]\,\mathrm{A/V}^{m_k}. \end{aligned} \tag{2.22}$$

Once the evolutionary procedure is executed, the best solution is selected. The values of the parameters that compose the chosen solution are shown in Table 2.11 (optimized solution). The fitness function of the result obtained in [90] is $f = (4.32 \times 10^{-2}, 1.52 \times 10^{-1})$ while the fitness function obtained with the evolutionary procedure is $f = (2.37 \times 10^{-2}, 1.46 \times 10^{-1})$. This means an improvement over the previous solution of 45 % for the f_1 objective ($I_D - V_D$ agreement) and 4 % for the f_2 objective ($I_D - V_S$ agreement). In this case, the improvement is reflected in a better estimation of the carrier mobility, which is almost three times greater than the original solution [90].

In this experiment, a very good agreement is also observed between experimental ($\times$) and estimated (solid lines) $I_D - V_G$ curves (Fig. 2.7f). The $M_C(V_G)$ relation is built from the extracted $M_C(V_G)$ values of Table 2.11.

2.4.3.2. Parameter Extraction. Experiment D

A parameter extraction procedure is now applied to current-voltage characteristics of a [poly(9,9-dioctylfluorene-co-bithiophene)] (F8T2) based OTFT designed as phototransistor [89]. The structure

used by these authors corresponds to an inverted, defined-gate, gate-planarized, coplanar TFT. The source and drain contacts were made of indium tin oxide (ITO), the channel length $L = 56\mu m$ and the channel width $W = 116\mu m$. Benzocyclobutene (BCB) was used as the gate-planarization layer, also acting as a gate insulator. PECVD hydrogenated amorphous silicon nitride (a-SiN:H) was used as a second gate insulator layer. The effective insulator thickness is 270 nm and the effective relative dielectric constant 2.3. Chromium (Cr) was used for the patterned gate electrode. The device was fabricated on a silicon substrate. A 1-wt % solution of F8T2 alternating copolymer dissolved in either xylenes or mesitylenes was used. A 1000-$\mathring{A}$-thick polymer film was spin-coated and was cured in a vacuum oven at 90^{o}C. The output and transfer characteristics measured by these authors in the phototransistors at 2.9 W/cm^2 illumination [89] are represented with crosses in Fig. 2.8a and 2.8b, respectively.

The aim of this experiment is not to analyze the effect of illumination but to extend the validity of our method to experimental data in different transistors operating in different conditions. The incorporation of the subthreshold region shown in the transfer characteristics (Figure 2.8b) adds complexity to the procedure. In order to reproduce the subthreshold region of Figure 2.8b, Equations (9)-(10) in [68] must be used instead of model (2.1). These equations are an asymptotically interpolation function of (2.1), and include a new parameter V_{SS} that controls the subthreshold slope.

The NSGA-II execution parameters defined for this experiment D are shown in Table 2.1 and the parameters of the bisection method are in Table 2.2. As in experiment A, values of m_k from 1.0 to 2.0 with a 0.1 step are tested, but only the m_k value that produces the best parameter set is selected. For the remaining parameters, the search space is defined as:

$$\begin{aligned} k_0 \in [10^{-12}, 10^{-8}]\,\mathrm{A/V}^{(2+\gamma)};\ \gamma \in [0.0, 2.0];\ V_T \in [-25, 15]\,\mathrm{V}; \\ V_{SS} \in [0, 20]\,\mathrm{V}\ ;\ M_C(V_{G_i}) \in [10^{-10}, 10^{-4}]\,\mathrm{A/V}^{m_k}. \end{aligned} \tag{2.23}$$

Again, the respective analysis of the obtained Pareto front set is conducted selecting as final result its best solution, or Pareto solution, $f = (4.46 \times 10^{-2}, 7.54 \times 10^{-2})$. The solution is represented in Fig. 2.8 and its estimated parameter set in Table 2.12. A good agreement between the experimental and estimated $I_D - V_D$ and $I_D - V_S$ curves is observed in Fig. 2.8a and 2.8c respectively. The carrier mobility used in the fitting is $\mu_0 = 3.14 \times 10^{-2}$ cm^2/Vs, one order of magnitude greater than the one obtained if using the ideal MOS model and ignoring the contact effects [89].

The transfer characteristics of Fig. 2.8b are an additional test of our procedure, showing a very good agreement between experimental (symbols) and estimated (solid line) $I_D - V_G$ curves, always within the measurement error range. Note that the four points shown with circles in Fig. 2.8b correspond to values taken from the output characteristics. These points are represented to indicate the possible error ranges in these measurements or other factors not considered in the model, such as dynamic or hysteresis effects. The values of the contact parameter M_C, which are extracted for discreet values V_{G_i}, are represented with symbols in Fig. 2.8d. They follow the relation: [4])

$$M_C = \alpha_2 (V_G - V_T')^{(1+\gamma)}, \tag{2.24}$$

Table 2.12: Extracted parameter set for the F8T2 OPTFT (k_0 is in A/V$^{2+\gamma}$, V_T in V, V_{SS} in V, and $M_C(V_G)$ in A/V^{m_k}).

x	Value
m_k	1.00×10^{0}
k_0	2.37×10^{-10}
γ	8.81×10^{-2}
V_T	-9.94×10^{0}
V_{SS}	$-5.34 \times 10^{+1}$
$M_C(-10V)$	1.20×10^{-10}
$M_C(-20V)$	2.44×10^{-10}
$M_C(-30V)$	5.60×10^{-10}
$M_C(-40V)$	1.02×10^{-09}

shown in solid line in 2.8d, with $\alpha_2 = 1.57 \times 10^{-10}$ and $V_T' = -8$ V, which is consistent with the value of V_T in Table 2.12, and thus, the solution can be considered physically acceptable. This relation $M_C(V_G)$ is used to calculate the transfer characteristics shown in Fig. 2.8b.

2.4.4. Computation costs

Since the main aim of this work is to prove that our evolutionary procedure can be employed as both, a parameter extraction method and an optimization procedure, the computation time is not considered a critical point in the EA definition. Even so, our evolutionary procedure reduces the time needed to find a solution with regard to previous extraction procedures. The evolutionary procedure could be used to optimize the solutions presented in this work even further, at the cost of increasing the number of iterations, and thus the computational time. Nevertheless, this effort is unnecessary when the error between the calculated and experimental data, is equal or lower than the measurement error, as shown in Fig. 2.8b.

After the evolutionary procedure execution, it was estimated that for the experiment A each job took 3.5 ± 1.4 hours, for the experiment B, 2.4 ± 0.7 hours, for experiment C_1, 28 ± 3 minutes and for experiment C_2, 45 ± 4 minutes. Finally for experiment D each job took 3.3 ± 1.4 hours. The difference in the execution time is mainly caused by the different number of points used to evaluate the fitting function.

It is very difficult to quantify the amount of time employed to find an acceptable solution with previous extraction procedures. In the situations in which the V_T and γ values estimated by the H_{VG} function are invalid, the previous extraction procedures may not find a solution (case exposed in Section 2.2). In other cases, the search of the remaining parameters by previous extraction procedures could start from an invalid or bad seed, taking too much time to converge or even not converging at all. On the contrary, the convergence of our evolutionary procedure is ensured for the exposed cases, even starting from a bad or invalid seed (initial population randomly generated).

2.5. Conclusion

We have used a multi-objective evolutionary parameter extraction procedure to extract device parameters of both a compact model for the current-voltage characteristics of OTFTs and a contact model. This procedure extends the applicability of compact models in TFTs as it provides solutions to some of the limitations of previous parameter extraction procedures, mainly imposed by the presence of contact effects that require the use of elaborate equations.

Once the free parameters of the algorithm have been fixed (number of individuals in each generation, the mutation rate, etc.), the process is fixed, and avoids the use of painstaking equations and procedures. Also complex expert knowledge is not required to determine a starting point, since the evolutionary procedure is capable of converging from a random point (random initial population), being necessary to define an acceptable physical margin for each parameter. Thus, the use of the evolutionary procedure ensures the extraction of reliable and accurate solutions since the evolutionary procedure explores completely its defined search space and will always reach an estimation of an OTFT parameter set.

Also, by exploring the search space defined around a previously known solution, estimated by evolutionary or other heuristic procedures, the proposed evolutionary procedure is capable of optimizing it. The evolutionary procedure has been successfully employed as extraction and optimization method for OTFTs, providing accurate model parameters.

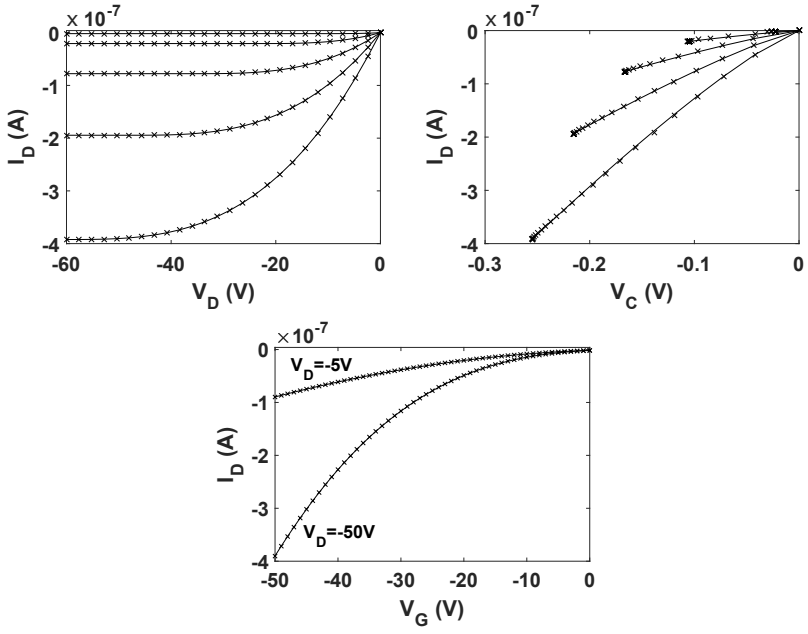

(I') $f = (1.01 \times 10^{-4}, 2.86 \times 10^{-2})$

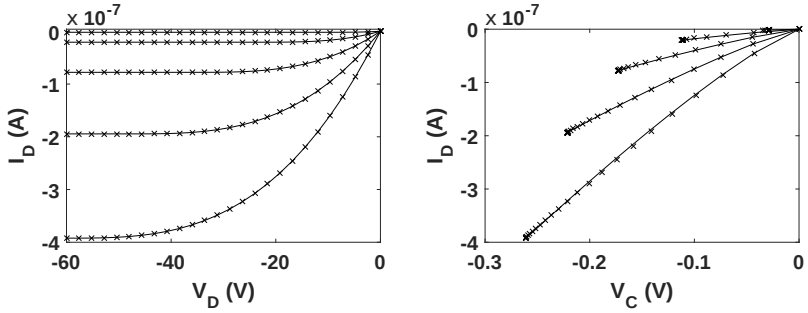

(II') $f = (1.13 \times 10^{-4}, 2.51 \times 10^{-2})$

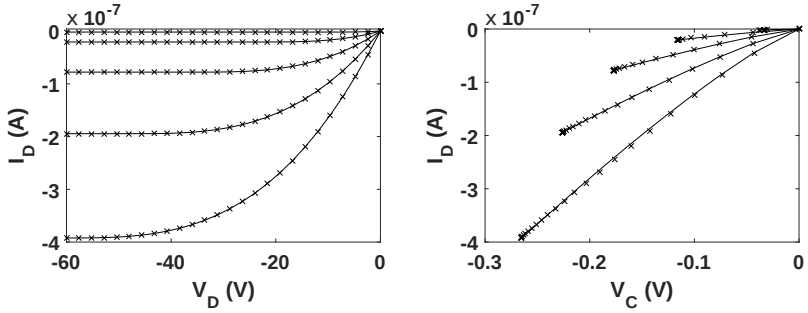

(III') $f = (1.32 \times 10^{-04}, 2.34 \times 10^{-2})$

Figure 2.6: Output characteristics and contact $I - V$ curves for the three Pareto-optimum solutions marked in Fig. 2.5. I_D and $\widehat{V_C}$ are represented with symbols and $\widehat{I_D}$ and V_C in solid lines. V_G is swept from 0 to $-50\,\mathrm{V}$ with a $-12.5\,\mathrm{V}$ step (from top to bottom in each figure). Transfer characteristics are added for the solution (i').

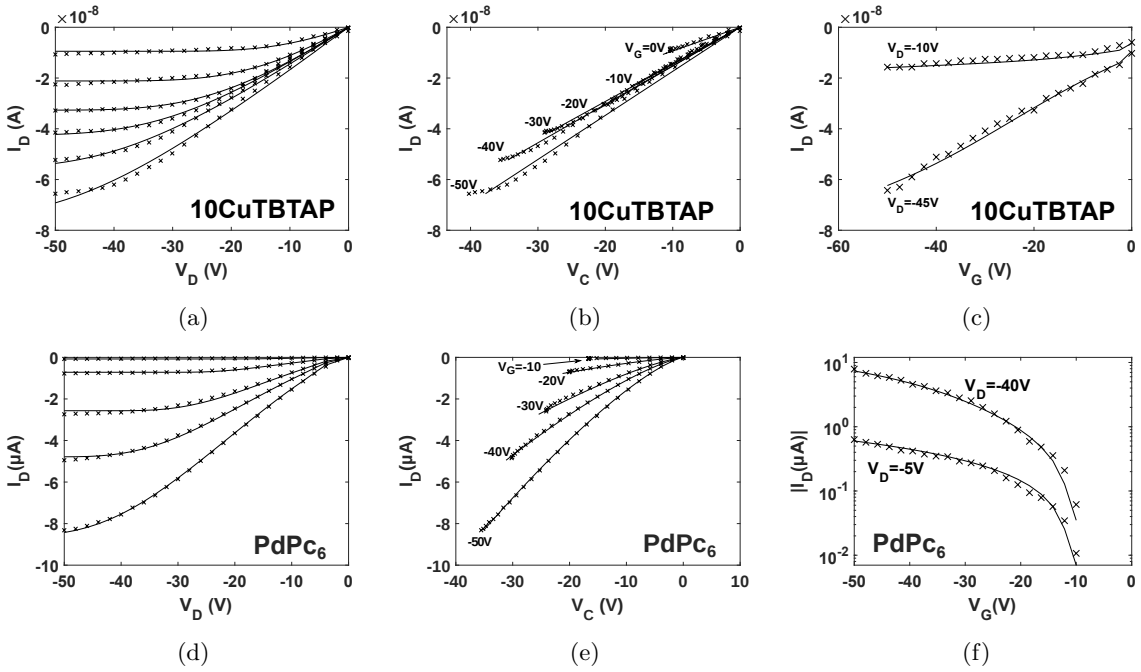

Figure 2.7: Experiments C_1 and C_2. Comparison of experimental ($\times$) and our calculations with (2.1) (solid lines) of, (a) and (d) output characteristics, and (c) and (f) transfer characteristics in 10CuTBTAP and $PdPc_6$ OTFTs. (b) and (e) Current–voltage curves extracted from (2.6) using the experimental output characteristics at different gate voltages ($\times$). The solid lines are the fittings using (2.2) and the respective estimated parameter sets for each transistor. In (a) and (b), V_G is swept from 0 (top) to $-50\,\mathrm{V}$ (bottom) with a $-10.0\,\mathrm{V}$ step. In (d) and (e), V_G is swept from -10 (top) to $-50\,\mathrm{V}$ (bottom) with a $-10.0\,\mathrm{V}$ step.

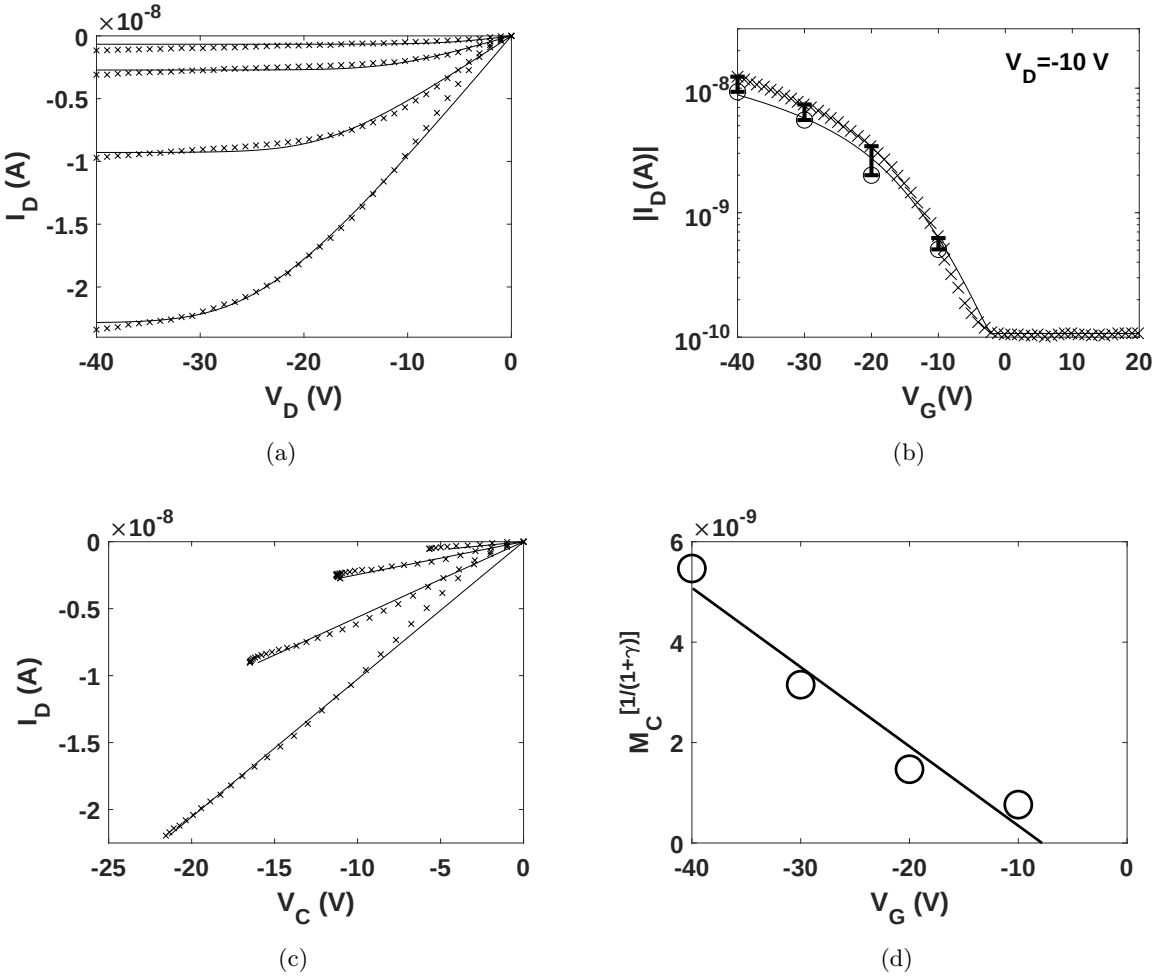

Figure 2.8: Experiment D. (a), (b) Comparison of experimental output and transfer characteristics, respectively, (symbols) and the numerical evaluation of (2.1) (modified to include the subthreshold region [68]) and including the parameter set of Table 2.12 (solid lines). (c) Current–voltage curves at the contact extracted from (2.6) and the experimental output characteristics (×). The solid lines are the fittings using (2.2) and the estimated parameter set of Table 2.12. (d) Extracted values of M_C. The solid line show the trend that the M_C set follows according to (2.24), with $V_T' = -8\,\mathrm{V}$. In (a) and (c) V_G is swept from -10 to $-40\,\mathrm{V}$ with a $-10.0\,\mathrm{V}$ step (from top to bottom). In (b), $V_D = -10$ V.

3

Constrained Many-Objective Evolutionary Extraction Procedure for an OTFT Compact Model including Contact Effects

3.1. Introduction

In this chapter, a constrained many-objective evolutionary parameter extraction procedure is formulated. It improves the parameter search process of the unconstrained multi-objective procedure defined in Chapter 2 [92].

This chapter is organized as follows. In Section 3.2, the OTFT compact model, in which the evolutionary procedure is executed, is presented. Then, in Section 3.3, the many-objective evolutionary procedure for the compact model is formulated. In Section 3.4, the evolutionary procedure is tested with experimental data. Finally, the conclusions are presented in Section 3.5.

3.2. Theory

A compact model for OTFTs including the voltage drop at the source contact ($V_S \equiv V_C$) and electric field dependent mobility $\mu = \mu_0(V_G - V_T)^\gamma$ was developed in [68, 69]:

$$\begin{aligned} I_D &= -k_0 \frac{W}{L} \frac{[(V_G - V_T - V_S)^{\gamma+2} - (V_G - V_T - V_D)^{\gamma+2}]}{\gamma + 2}; \\ k_0 &= \mu_0 C_{ox}, \end{aligned} \tag{3.1}$$

where V_G is the gate voltage, V_D is the drain voltage, V_T is the threshold voltage, γ is the mobility enhancement factor, μ_0 is the mobility-related parameter and its dimension is expressed as $\mathrm{cm}^2/(\mathrm{V}^{1+\gamma}\mathrm{s})$, C_{ox} is the capacitance per unit area of the oxide and W and L are the channel width and length, respectively.

If the values of γ, V_T and k_0 are known, the voltage in the contacts $V_S(I_D, V_G)$ can be extracted by introducing the values of the experimental data and the values of γ, V_T and k_0 in (3.1):

$$V_S = V_G - V_T - \left[I_D(\gamma + 2)L/(Wk_0) + (V_G - V_T - V_D)^{\gamma+2} \right]^{1/(\gamma+2)}. \tag{3.2}$$

Model (3.1) can be reinforced with the inclusion of an electrical model for the contact region that accounts for the observed trends (from linear to quadratic, $1 \leq m_k \leq 2$) in the triode region of OTFTs [4, 93]:

$$V_S = \left(\frac{I_D}{M_C} \right)^{\frac{1}{m_k}} \tag{3.3}$$

where the parameter M_C is usually gate voltage dependent:

$$M_C = \alpha(V_G - V_T)^{(1+\gamma)}, \tag{3.4}$$

and α is a parameter that includes proportionality constants appearing in the relation between the carrier mobility and the electric field and the relation between the conductance of the contact region, $\sigma_{contact}$, and the conductance of the channel $\sigma_{channel}$ [$\sigma_{contact} = \kappa\sigma_{channel}$ with $\sigma_{channel} = C_{ox}(V_G - V_T)$] [4, 42]. M_C coincides with the conductance of the contact region when $m_k = 1$.

3.3. Constrained Many-Objective Evolutionary Parameter Extraction Procedure

In Chapter 2, the compact model presented in Section 3.2 was complemented with a multi-objective evolutionary parameter extraction procedure [92]. This multi-objective evolutionary procedure was successfully employed to extract the parameters of different OTFTs. In this chapter, some changes are implemented to improve the evolutionary procedure search process, conducting a more efficient exploration of the areas where more promising solutions are allocated.

New objectives are added to the original Multi-Objective Problem (MOP) giving place to a Many-Objective Problem (MaOP) with four objectives [94]. Along with the MaOP definition, a set of constraints are defined for the solution pool, including the random initial one. The remaining characteristics of the evolutionary procedure are maintained as detailed in Chapter 2 [92], including the use of ECJ [88].

Like in the original version, the extended evolutionary procedure is based on a set of experimental data $I_D = I_D(V_{G_i}, V_{D_j})$, where $i \in \mathbb{Z} : 1 \leq i \leq g$ and $j \in \mathbb{Z} : 1 \leq j \leq d$. The numerical estimation of I_D with (3.1) and (3.3), and the numerical estimation of the voltage drop at the contact region V_S with (3.2) are named $\widehat{I_D}(V_{G_i}, V_{D_j}, x)$ and $\widehat{V_S}(V_{G_i}, V_{D_j}, x)$, respectively, where x refers to the rest of parameters needed to compute (3.1)-(3.3) and is defined as the individual of the population:

$$x = (k_0, \gamma, V_T, m_k, M_C(V_{G_1}), ..., M_C(V_{G_g})) \tag{3.5}$$

where g is the number of different V_G values employed to generate I_D.

3.3.1. Fitness Function

A total of four objectives applied to the individual (3.5) define the MaOP: (f_1) to minimize the error between the experimental values of $I_D(V_{G_i}, V_{D_j})$ and their estimation from (3.1) and (3.3), $\widehat{I_D}(V_{G_i}, V_{D_j}, x)$; (f_2) to minimize the error between the voltage drops at the contact region $V_S(V_{G_i}, V_{D_j}, x)$ extracted from (3.3) and their estimation $\widehat{V_S}(V_{G_i}, V_{D_j}, x)$ extracted from (3.2); (f_3) to maximize the standard determination coefficient $R^2(V_{G_i}, x)$ of the linear fit of ${M_C}^{1/(1+\gamma)}$ with V_G (3.4):

$${M_C}^{1/(1+\gamma)}(V_G) = \alpha^{1/(1+\gamma)} V_G - \alpha^{1/(1+\gamma)} \widehat{V_T}; \tag{3.6}$$

(f_4) to minimize the difference between V_T coded in x an its estimation $\widehat{V_T}(V_{G_i}, x)$ extracted from the linear fit (3.6).

The *Normalized Root Mean Squared Error* (NRMSE) is used to estimate errors (f_1) and (f_2)[87]:

$$\text{NRMSE}(y, \hat{y}) = \sqrt{\frac{\sum_{z=1}^{w} (y_z - \hat{y}_z)^2}{\sum_{z=1}^{w} (y_z - \bar{y})^2}} \tag{3.7}$$

where y represents the data set that we want to accurately approximate, $\hat{y}$ is the estimation of y, w is the number of data samples in y, and $\bar{y}$ is the mean value of the complete data set y.

Thus, the minimization fitness function f is defined as $f = (f_1, f_2, f_3, f_4)$, where

$$\begin{aligned} f_1(x) &= \text{NRMSE}\left(I_D(V_{G_i}, V_{D_j}), \widehat{I_D}(V_{G_i}, V_{D_j}, x)\right), \\ f_2(x) &= \text{NRMSE}\left(V_S(V_{G_i}, V_{D_j}, x), \widehat{V_S}(V_{G_i}, V_{D_j}, x)\right), \\ f_3(x) &= 1.0 - R^2(V_{G_i}, x), \\ f_4(x) &= \left|\widehat{V_T}(V_{G_i}, x) - x_3\right| = \left|\widehat{V_T}(V_{G_i}, x) - V_T\right|, \\ &\forall i \in \mathbb{Z} : 1 \leq i \leq g, \forall j \in \mathbb{Z} : 1 \leq j \leq d \end{aligned} \tag{3.8}$$

3.3.2. Constraints

In order to prevent the procedure to converge to physically unacceptable solutions, such as negative contact voltages or negative conductances, when positive ones are expected, some simple constraints are incorporated:

1. $\widehat{V_S}(V_{G_i}, V_{D_j}, x) \geq 0$
2. $M_C(V_{G_i}) > 0$.

Other constraints are implicit in the search space definition, which are consistent with the physical meaning of each parameter.

3.3.3. Variables

Once the objectives and constraints are defined, the procedure works with the following variables:

3.3.3.1. $I_D(V_{G_i}, V_{D_j})$

$I_D(V_{G_i}, V_{D_j})$ is the experimental value of the drain current.

3.3.3.2. $\widehat{I_D}(V_{G_i}, V_{D_j}, x)$

$\widehat{I_D}(V_{G_i}, V_{D_j}, x)$ is the estimation of $I_D(V_{G_i}, V_{D_j})$ extracted from the compact model (3.1) and (3.3) using the bisection method [73]. This procedure starts with an initial interval $[a_i, b_i]$ in which the value of $\widehat{I_D}(V_{G_i}, V_{D_j}, x)$ is expected. This interval may be different for each value of V_{G_i}. The interval is shortened to the half in successive iterations until an adequate value for $\widehat{I_D}(V_{G_i}, V_{D_j}, x)$ is obtained.

Starting at iteration $t = 0$, and assuming that $a_{ij_0} = a_i$ and $b_{ij_0} = b_i$, three values are considered in each iteration t for all possible combinations of i and j:

$$\begin{aligned}
\widehat{I_{D_{a,t}}}(V_{G_i}, V_{D_j}, x) &= a_{ij_t}, \\
\widehat{I_{D_{b,t}}}(V_{G_i}, V_{D_j}, x) &= b_{ij_t}, \\
\widehat{I_{D_{c,t}}}(V_{G_i}, V_{D_j}, x) &= c_{ij_t} = (a_{ij_t} + b_{ij_t})/2
\end{aligned} \tag{3.9}$$

For each one of these values, V_S is calculated using (3.3) and the values of $M_C(V_{G_i})$ and m_k coded in x:

$$\begin{gathered}
V_{S_{k,t}}(V_{G_i}, V_{D_j}, x) = \left(\frac{\widehat{I_{D_{k,t}}}(V_{G_i}, V_{D_j})}{M_C(V_{G_i})} \right)^{\frac{1}{m_k}}, \\
\forall i \in \mathbb{Z} : 1 \leq i \leq g, \forall j \in \mathbb{Z} : 1 \leq j \leq d, k \in \{a, b, c\}
\end{gathered} \tag{3.10}$$

Then, the differences between each one of the three possible estimations $k \in \{a, b, c\}$ of I_D in the current iteration and the value returned by the compact model (3.1) are calculated:

$$\begin{aligned}
r_{k,ij_t} = \widehat{I_{D_{k,t}}}(V_{G_i}, V_{D_j}) + \\
+ \frac{k_0 W \left(V_{G_i} - V_T - V_{S_{k,t}}(V_{G_i}, V_{D_j}) \right)^{\gamma+2}}{L(\gamma+2)} - \\
- \frac{k_0 W \left(V_{G_i} - V_T - V_{D_j} \right)^{\gamma+2}}{L(\gamma+2)}
\end{aligned} \tag{3.11}$$

As the bisection procedure tries to find a root in (3.11), the interval $[a_{ij_t}, b_{ij_t}]$ is shortened according to the values r_{a,ij_t}, r_{b,ij_t} and r_{c,ij_t} following the rule:

$$[a_{ij_{t+1}}, b_{ij_{t+1}}] = \begin{cases} [c_{ij_t}, b_{ij_t}], & \text{if } \operatorname{sign}(r_{a,ij_t}) = \operatorname{sign}(r_{c,ij_t}) \\ [a_{ij_t}, c_{ij_t}], & \text{otherwise} \end{cases} \tag{3.12}$$

This iterative process continues until the condition$|r_{c,ij_t}| < \varepsilon$ is reached or a maximum number of iterations are executed ($t = n_{\text{bisec}}$). In any case, the drain current is estimated as $\widehat{I_{D_{c,t}}}(V_{G_i}, V_{D_j}, x) = c_{ij_t}$.

3.3.3.3. $V_S(V_{G_i}, V_{D_j}, x)$

$V_S(V_{G_i}, V_{D_j}, x)$ is the voltage drop at the contact introducing in (3.3) the experimental value $I_D(V_{G_i}, V_{D_j})$ and the parameter $M_C(V_{G_i})$ and m_k coded in x:

$$V_S(V_{G_i}, V_{D_j}, x) = \left(\frac{I_D(V_{G_i}, V_{D_j})}{M_C(V_{G_i})} \right)^{\frac{1}{m_k}}. \tag{3.13}$$

3.3.3.4. $\widehat{V_S}(V_{G_i}, V_{D_j}, x)$

$\widehat{V_S}(V_{G_i}, V_{D_j}, x)$ is the voltage drop at the contact introducing in (3.2) the experimental value $I_D(V_{G_i}, V_{D_j})$ and the parameters k_0, γ and V_T coded in x:

$$\widehat{V_S}(V_{G_i}, V_{D_j}) = V_{G_i} - V_T - \\ - \left[I_D(V_{G_i}, V_{D_j}) \frac{(\gamma+2)L}{W k_0} + (V_{G_i} - V_T - V_{D_j})^{\gamma+2} \right]^{1/(\gamma+2)} \tag{3.14}$$

3.3.3.5. $R^2\,(V_{G_i}, x)$

$R^2\,(V_{G_i}, x)$ is the standard determination coefficient r-squared, measuring the goodness of the linear fit of ${M_C}^{1/(1+\gamma)}(V_{G_i})$ according to (3.6), being $M_C(V_{G_i})$ and γ coded in x.

3.3.3.6. $\widehat{V_T}(V_{G_i}, x)$

$\widehat{V_T}(V_{G_i}, x)$ is the threshold voltage estimation extracted from the linear relation of ${M_C(V_{G_i})}^{1/(1+\gamma)}$ with V_{G_i} according to (3.6), with $M_C(V_{G_i})$ and γ coded in x.

3.4. Results

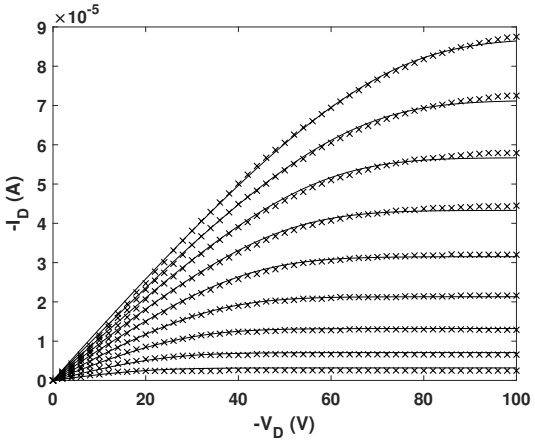

Figure 3.1: Comparison of experimental output characteristics of a DHα6T OTFT ($\times$) and our calculations introducing the parameters of Table 3.1 in (3.1) (solid lines). V_G is swept from -20 V to -100 V in steps of -10 V (from bottom to top).

Once the compact model and its associated evolutionary procedure have been presented, they are applied to experimental $I_D - V_D$ curves of an α,ω-dihexylsexithiophene (DHα6T) OTFT [95]. The output characteristics measured by the authors are represented with crosses in Fig. 3.1. The $I_D - V_D$ curves are analyzed with the evolutionary procedure, extracting the parameters coded in (3.5) that makes our model (3.1) and (3.3) best fit the experimental data. The resulting values are in Table 3.1.

An excellent agreement between the experimental and estimated $I_D - V_D$ curves is observed in Fig. 3.1. In Fig. 3.2, a very good agreement is also observed for the $I_D - V_C$ curves calculated from (3.2) and

(3.3). They both show a linear trend ($m_k = 1.0$). In Fig. 3.3, the estimated values of $M_C(V_{G_i})^{1/(1+\gamma)}$ (circles) are represented and compared with the solid line defined by (3.6), with $\alpha = 1.17 \times 10^{-08}$ A/V$^{2.07}$. Note how the line crosses the V_G-axis at $\widehat{V_T} = -5.4$ V, value very close to the extracted V_T.

Table 3.1: Extracted DHα6T OTFT parameters values (k_0 is in A/V$^{2+\gamma}$, M_C is in A/V^{m_k} and V_T in V).

x	$Value$
k_0	$5.45E-09$
γ	$7.00E-02$
V_T	$-5.30E+00$
m_k	$1.00E+00$
$M_C(-20V)$	$1.75E-07$
$M_C(-30V)$	$3.32E-07$
$M_C(-40V)$	$5.22E-07$
$M_C(-50V)$	$7.09E-07$
$M_C(-60V)$	$8.93E-07$
$M_C(-70V)$	$1.05E-06$
$M_C(-80V)$	$1.20E-06$
$M_C(-90V)$	$1.34E-06$
$M_C(-100V)$	$1.46E-06$

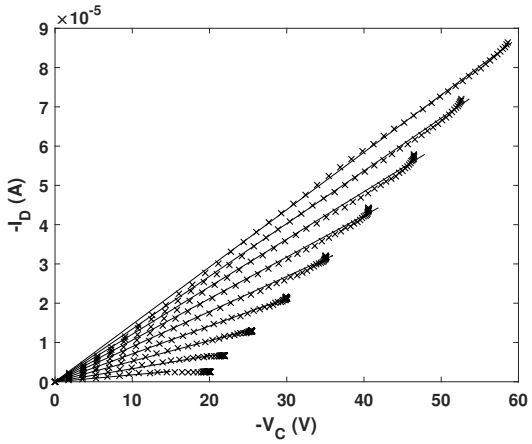

Figure 3.2: Contact $I-V$ curves of a DHα6T OTFT. $I_D - V_C$ curves extracted from (3.2) using the experimental output characteristics at different V_G values ($\times$). The solid lines are the fittings using (3.3) and the parameters of Table 3.1. V_G is swept from -20 V to -100 V in steps of -10 V (from bottom to top).

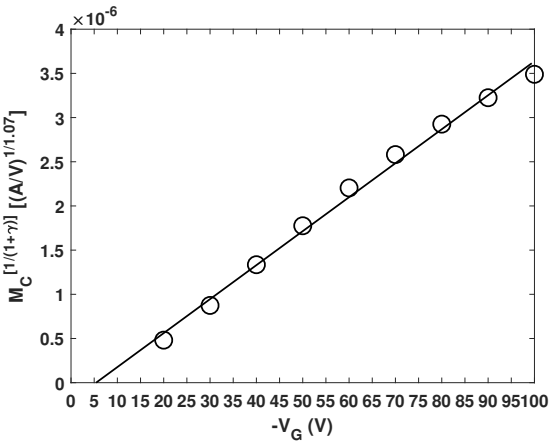

Figure 3.3: Estimated values of $M_C(V_{G_i})^{1/(1+\gamma)}$ (circles). The solid line shows the trend according to (3.6), crossing the V_G-axis at $\widehat{V_T} = -5.4$ V.

3.5. Conclusion

In this chapter, we have modified a parameter extraction method used in combination with a compact model for OTFTs. An initially unconstrained multi-objective evolutionary parameter extraction procedure has given place to a constrained many-objective version. In comparison with it predecessor, this constrained many-objective evolutionary procedure reduces the range of values of the parameters in which the search process takes place, thus carrying out a more specific exploration of the search space. In this sense, more promising parameter sets (including contact resistances values) are achieved.

In particular, the addition of constraints is a way of including expert knowledge into the evolutionary procedure. In this chapter, constraints help the evolutionary procedure user to save analysis time, since the user will not have to run a comprehensive search looking for solutions generating valid $I_D - V_C$ curves. Moreover, the inclusion of two more objectives with regard to the initial evolutionary procedure version also helps the evolutionary procedure user. In the previous version of the evolutionary procedure, the user should check the complete final solution set looking for a solution with $V_T \approx \widehat{V_T}$ and following the linear trend of ${M_C}^{1/(1+\gamma)}(V_G)$. With the proposed evolutionary procedure this is not necessary since an objective value describes both situations.

It is worth mentioning that the extracted parameter set meets the quality expert requirements established in the MaOP definition. More accurate parameter extractions are conducted using the many-objective procedure. By using the many-objective evolutionary procedure, $f_1 < 0.02$ and $f_2 < 0.04$ values are achieved, while they are not reachable using the multi-objective version (both procedures executed under the same circumstances). Also by using the many-objective procedure, parameter sets with $0.00 \leq f_3 \leq 0.01$ and $f_4 < 0.01$ are obtained. These values are far from being achieved using the previous multi-objective version, which does not guide the search towards those solutions.

Despite the obtained result is satisfactory, recent studies prove that MOEAs such as NSGA-II have some limitations to manage MaOPs. Since the number of objectives can be increased in the future,

different alternatives to take on the challenges of MaOPs should be considered. Some of these alternatives are discussed in Section 6.2.

4

Compact modeling of the effects of illumination on the contact region of organic phototransistors

4.1. Introduction

Over the past two decades, the organic (polymeric) semiconductor technology has attracted considerable research interest [1, 30, 96]. Many efforts have been made to develop different kinds of organic devices that cover a wide range of industrial and commercial applications, such as organic light-emitting diodes (LEDs), organic photovoltaic cells (OPVs) and organic thin-film transistors (OTFTs) [1, 30, 96]. OTFTs are particularly interesting since they are the basis of other devices, such as memories and sensors.

Organic phototransistors (OPTs) are a particular case of transistors and sensors in which light detection and signal amplification are combined together in a single component. Like the rest of organic devices, OPTs show great advantages with regard to their inorganic counterparts, such as light-weight, low-cost, easy solution processing and flexibility [96]. Nevertheless, they also show common performance disadvantages, such as a low carrier mobility [1, 30, 31] or high process variability [32, 33, 97–99].

Currently, the OPTs' photosensitivity and photoresponsivity are also inferior to those in inorganic phototransistors, although novel strategies are developed to enhance these properties, such as blending p-type and n-type semiconductors as donor-acceptor channel layers [100, 101]. A key issue in the OPTs' performance is the contact quality at the semiconductor channel/electrode interfaces [102–105]. In fact, attempts to monitor the way the contact region in an OPT evolves with illumination were studied in the past [102, 104, 106–108]. Contacts play a main role in the exciton dissociation and extraction of charge, which are essential mechanisms in OPTs' performance [109]. Also, contact effects degrade the performance of OTFTs. For this reason, they have been extensively studied and even incorporated in OTFT compact models [2, 4, 18, 34–37, 68, 69, 110]. However, from the our knowledge, the way the contact region evolves with illumination has not been introduced specifically in compact models for OPTs. The incorporation of this dependence of the contact region with illumination in a compact model would provide a better characterization of the device and would establish new optimization pathways. The resulting model would include more accurate values of the main parameters that control the current-voltage characteristics of the OPT: charge carrier mobility, threshold voltage and the contact resistance itself.

In order to fill this gap, a compact model that describes the current-voltage characteristics of OPTs is presented in this chapter. The model includes the dependence of the voltage drop at the contact regions with illumination, and it is sensitive to the photoconductive and photovoltaic effects. The model is validated applying the evolutionary procedure defined in Chapter 3 to experimental data.

This chapter is organized as follows. In Section 4.2, the applicability of a widely known compact model in OTFTs including contact effects [4, 68, 69] is extended to OPTs, in which the photoconductive and photovoltaic mechanisms are incorporated in the model. In Section 4.3, the evolutionary parameter extraction procedure [111] presented in Chapter 3 is summarized and adapted to the model. In Section 4.4, the proposed model is validated with published experimental data in OPTs under different illumination conditions. Finally, the conclusions are presented in Section 4.5.

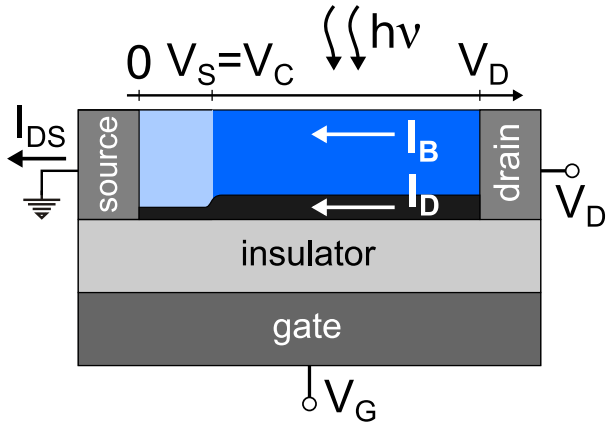

Figure 4.1: Cross-sectional view of an OPT structure with the bottom-contact configuration.

4.2. Theory

Figure 4.1 shows a cross sectional view of an OPT structure. The source terminal voltage is zero and V_D and V_G are the drain and gate terminal voltages, respectively. V_S (or V_C) is the voltage drop at the contact (the contact region is exaggerated for clarity). The electric current flowing between drain and source terminals I_{DS} is composed of the field-effect (channel) current I_D flowing in the accumulation layer and the bulk current I_B [112]:

$$I_{DS} = I_B + I_D. \tag{4.1}$$

In the depletion (cut-off) region, $I_D \ll I_B$ and $I_{DS} \simeq I_B$. In sub-threshold or over threshold conditions, $I_B \ll I_D$ and $I_{DS} \simeq I_D$. In order to ensure a smooth transition from depletion to conduction, (4.1) can be written as:

$$I_{DS} = I_B \left[1 + \left(\frac{I_D}{I_B}\right)^s\right]^{1/s}, \ \forall s \in \mathbb{Z} : s > 0 \tag{4.2}$$

where s is a free parameter employed to control the transition smoothness [113].

4.2.1. Dark

The objective of this chapter is to develop a compact model for the current-voltage characteristics of an OPT that incorporates the evolution of the contact region with the intensity of the light. Since the OPT is a particular case of OTFT, then, as a starting point, we consider a well-established compact model for the OTFT [68, 69]:

$$\begin{aligned} I_D &= k' \frac{W}{L} \frac{V_{EODR}(V_S)^{(2+\gamma)} - V_{EODR}(V_D)^{(2+\gamma)}}{2+\gamma}, \\ k' &= \mu_0 C_{ox}; \ V_{EODR}(V) = V_{SS} \ln\left[1 + \exp\left(\frac{V_G - V_T - V}{V_{SS}}\right)\right], \end{aligned} \tag{4.3}$$

which includes the voltage drop at the source contact, $V_S \equiv V_C$, and electric field-dependent mobility [114],

$$\mu = \mu_0 (V_G - V_T)^{\gamma}, \tag{4.4}$$

with V_T being the threshold voltage, C_{ox} the capacitance per unit area of the oxide, and W and L the channel width and length, respectively. V_{SS} is a voltage parameter related to the steepness of the subthreshold characteristics of the TFT, μ_0 is the mobility-related parameter expressed as $\mathrm{cm}^2/(\mathrm{V}^{1+\gamma}\mathrm{s})$, and $\gamma = 2(T_0/T - 1)$ is the mobility enhancement factor, which is a semi-empirical parameter that depends on the temperature T. It is associated to the width of the band tail distribution of the density of states (DOS) that is represented as a characteristic temperature T_0. In order to provide a single value for the voltage dependent mobility, the mobility is evaluated at $V_{GT} = V_G - V_T = 1$ V, thus $\mu(V_{GT} = 1\ \mathrm{V}) = \mu_0$ in $\mathrm{cm}^2/(\mathrm{Vs})$. This compact model is able to describe all operation modes of the transistor: triode, saturation, subthreshold or even reverse biasing. The depletion region would require the use of (4.2).

In case the parameters γ, V_T, V_{SS} and k' are known, the voltage in the contacts $V_S(I_D, V_G)$ would be extracted by introducing the values of the experimental data (I_D, V_G, V_D) and the values of γ, V_T, V_{SS} and k' in (4.3):

$$\begin{aligned} V_S = {} & V_G - V_T - V_{SS} \\ & \times \ln \left[\exp \left(\frac{\left(\frac{I_D L(\gamma+2)}{W k'} + V_{EODR} (V_D)^{(\gamma+2)} \right)^{\frac{1}{\gamma+2}}}{V_{SS}} \right) - 1 \right]. \end{aligned} \tag{4.5}$$

However, as these parameters are not known *a priori*, model (4.3) was lately redefined with the inclusion of a model for the contact region [4]:

$$V_S = \left(\frac{I_D}{M_C} \right)^{\frac{1}{m_k}}, \tag{4.6}$$

where m_k is a constant that indicates the grade of the observed trend (from linear to quadratic, $1 \leq m_k \leq 2$) in the triode region of the OTFT [93] and the parameter M_C is usually gate voltage dependent:

$$M_C = \alpha (V_G - V_T)^{(1+\gamma)}. \tag{4.7}$$

The subthreshold regime is not considered in (4.7), but it can be easily added by an asymptotically interpolation function, similar to that used in (4.3) for other field effect transistors [115–117]. The result is:

$$M_C = \alpha V_{SS} \ln \left[1 + \exp \left(\frac{V_G - V_T}{V_{SS}} \right) \right]^{1+\gamma}. \tag{4.8}$$

M_C coincides with the conductance of the contact region when $m_k = 1$. The dependence of M_C with the threshold voltage comes from two facts. The first one is through the gate voltage dependent carrier mobility (4.4), which is controlled with the parameter γ. The second one considers that the free charge

density per unit area in the contact region $\sigma_{contact}$ is lower but proportional to the free charge density in the active channel $\sigma_{channel}$ ($\sigma_{contact} = \kappa\sigma_{channel}$) with $\sigma_{channel} = C_{ox}(V_G - V_T)$. The proportionality between the free charge densities at these two adjacent regions is assumed, since there is no physical reason to believe that the mobile charges in these two regions start appearing at very different gate voltages, or follow very different trends, unless local non-uniformities were present just at the contact region. The value of the proportionality constant between these two charge densities κ, implicit in the value of α, was tested to be sensitive to the contact material and temperature [4]. Overall, the application of the combined model (4.3), (4.6) and (4.7) can be found in different kinds of OTFTs [39–44, 90, 92, 118]. Nevertheless, neither the model nor the sensitivity of the parameter M_C to illumination were previously tested.

4.2.2. Illumination

The current-voltage characteristics of OPTs under illumination are controlled by the photoconductive and photovoltaic mechanisms. The photoconductive effect is detected when the transistor operates in the depletion region. The photovoltaic effect is observed in on-state and can be detected by a modification of the value of the threshold voltage. The extension of model for OPTs in dark (4.3)-(4.8) to illumination conditions needs to include the influence of the incident light P on the parameters I_B, V_T and α.

Bulk current, I_B

In cut-off operation, the gate no longer controls the transistor and the device performs as an organic semiconductor sandwiched between two contacts. In this region, the photoresponse of the device is similar to that of photoresistors. The device current $I_{DS} \simeq I_B$ and the photo-generated charge carriers enhance the conductivity of the bulk. Experimentally, it was shown that the photocurrent in the off state is directly proportional to the incident light intensity [106, 107, 109, 119], and it can be described with the expression [102, 103, 106, 107, 120]:

$$I_B - I_{B_0} = (qn\mu F)WD = \beta_I P, \tag{4.9}$$

where I_{B_0} is the bulk current in dark, n is the carrier density, F is the electric field in the semiconductor, W is the gate width, D is the depth of absorption region, and β_I is a fitting parameter that controls the observed linear relation between the bulk current and the light intensity P. An increment of the conductivity can be directly originated by an increment of the carrier density and indirectly by a modification of the mobility as a function of the carrier density. Nevertheless, this last hypothesis can be discarded since previous studies show that the carrier mobility does not increase linearly with the carrier density [121, 122]. In this regard, an almost invariant value of the carrier mobility with illumination might be expected. In Section 4.4, we will check whether this hypothesis is valid by analyzing the extracted values of the carrier mobility as a function of the illumination intensity P.

Threshold voltage, V_T

When the OPT operates in conduction, including both sub-threshold and over-threshold regions, the increase of the drain current with illumination is linked to a modification of the threshold voltage ΔV_T. This modification can be associated to an accumulation of trapped photogenerated charges at the organic-insulator interface [89, 123, 124] or in layers close to the contact regions [125], with a high concentration of defects and traps, in which excitons are photogenerated and subsequently free charges are separated. In the semiconductor bulk, far from these layers and interfaces, the exciton recombination is high due to the absence of high electric fields. For this reason, recent OPT topologies involving bulk heterojunction (BHJ) composite of p-type and n-type materials as channel layers provide additional dissociation sites for the photogenerated excitons [100, 101]. The variation ΔV_T is usually modeled as [126, 127]:

$$V_T = V_{Td} - \Delta V_T;\ \Delta V_T = \frac{AkT}{q} \ln\left(1 + \frac{\eta q P}{I_{Dd} h\nu}\right), \tag{4.10}$$

where V_{Td} and I_{Dd} are the threshold voltage and the channel current at dark conditions, respectively, k is the Boltzmann constant, T is the temperature, q is the magnitude of the electron charge, η is the quantum efficiency associated with the absorption process in the channel, $h\nu$ is the photon energy and A is an empirical constant. The parameter A was first introduced in [126] for studying High-Electron Mobility Transistors (HEMTs) under illumination. It was defined as the ratio of the variation of the threshold voltage in the transistor under illumination and the variation of the barrier seen by free carriers at the source. The lowering of the energy barrier at the source contact is attributed to an accumulation of trapped photogenerated carriers in this region, that was previously modeled for photodiodes [128].

It is remarkable how model (4.10), which initially was proposed as a link between the variation of the threshold voltage of the HEMT and the barrier lowering at the source region, has been applied successfully to their organic counterparts [102, 103, 106, 107, 119, 120, 129, 130]. If such an important connection exists between the variation of the threshold voltage of the device and a possible barrier lowering at the contact region, then the transistor models should include the dependence of the contact region with illumination. In our model, it should be included in the contact conductance M_C.

Contact conductance, M_C

We mentioned above that the free charge density in the contact region is proportional to the free charge density in the channel ($\sigma_{contact} = \kappa\sigma_{channel}$) and also lower than it. On the one hand, this means that both follow the same trend with $V_G - V_T$, and thus, the photovoltaic effect is implicit in the model of the contact region (4.6)-(4.8). On the other hand, the constant κ being less than one means that there is margin for the conductivity of the contact region to be increased by modifying the temperature [4], the light intensity P, or any other physical or chemical external variable. Intuitively, since the bulk of the organic material is affected by the photoconductive effect, the contact region might also be affected. The photoconductive effect can be clearly distinguished in the cut-off region when the conducting channel and the photoconductive effect are negligible. However, this does not mean that the photoconductivity effect cannot affect other operating regions of the device. As the proportionality constant κ, which is

implicit in α [4], relates the conductivity of the contact region and that of the channel, both κ and α might be modulated by a linear function as described by the photoconductive effect. In this regard, the parameter α in (4.7)-(4.8) can be written as:

$$\alpha = \beta_\alpha P + \alpha_0, \tag{4.11}$$

where α_0 is the value of α in dark and β_α controls the linear evolution of α with the light intensity.

4.3. Evolutionary Parameter Extraction Procedure

Once the model for OPTs is described, in which both photoconductive and photovoltaic effects are included in the contact model, a validation of this theory is necessary. For that purpose, output and transfer characteristics are evaluated with our model, aiming to reproduce published experimental measurements of OPTs. In order to compare experimental and numerical results, we will make use of the evolutionary parameter extraction procedure [111] defined in Chapter 3.

Despite Chapter 3 was completely dedicated to the many-objective evolutionary parameter extraction procedure definition, in this section a small description of the procedure, along with the changes needed to adapt it to (4.3), is given subsequently. The procedure is based on a set of experimental data $I_D = I_D(V_{G_i}, V_{D_j})$, where $i \in \mathbb{Z} : 1 \leq i \leq g$ and $j \in \mathbb{Z} : 1 \leq j \leq d$, and g and d are the total number of discrete values of V_G and V_D, respectively. The numerical estimation of I_D with (4.3) and (4.6), and the numerical estimation of the voltage drop at the contact region V_S with (4.5) are named $\widehat{I_D}(V_{G_i}, V_{D_j}, x)$ and $\widehat{V_S}(V_{G_i}, V_{D_j}, x)$, respectively, where x refers to the set of parameters needed to compute (4.3)-(4.7), and is defined as an individual of the population:

$$x = (k', \gamma, V_T, V_{SS}, m_k, M_C(V_{G_1}), \ldots, M_C(V_{G_g})), \tag{4.12}$$

where x_l ($l \in \mathbb{Z} : 1 \leq l \leq p$) is a variable of an individual and $p = g + 5$ is the length or number of variables of an individual (4.12).

The evolutionary parameter extraction procedure solves a many-objective problem (MaOP). In our MaOP, four objectives have been defined for an individual (4.12):

(O_1) to minimize the error between the experimental values of $I_D(V_{G_i}, V_{D_j})$ and their estimation from (4.3) and (4.6) $\widehat{I_D}(V_{G_i}, V_{D_j}, x)$;

(O_2) to minimize the error between the voltage drops at the contact region $V_S(V_{G_i}, V_{D_j}, x)$ described by (4.6) and their estimation $\widehat{V_S}(V_{G_i}, V_{D_j}, x)$ extracted from (4.5);

(O_3) to maximize the standard determination coefficient $R^2(V_{G_i}, x)$ of the linear fit of ${M_C}^{1/(1+\gamma)}$ with V_G, which extracted from (4.7) is:

$${M_C}^{1/(1+\gamma)}(V_G) = \alpha^{1/(1+\gamma)} V_G - \alpha^{1/(1+\gamma)} \hat{V}_T; \tag{4.13}$$

and (O_4) to minimize the difference between V_T coded in x (x_3) and its estimation $\widehat{V_T}(V_{G_i}, x)$ extracted from the linear fit (4.13).

The *Normalized Root Mean Squared Error* (NRMSE) is used to estimate errors (O_1) and (O_2)[87]:

$$\mathrm{NRMSE}(y,\hat{y}) = \sqrt{\frac{\sum_{z=1}^{w}(y_z-\hat{y}_z)^2}{\sum_{z=1}^{w}(y_z-\bar{y})^2}}, \tag{4.14}$$

where y represents the data set that we want to accurately approximate, $\hat{y}$ is the estimation of y, w is the number of data samples in y, and $\bar{y}$ is the mean value of the complete data set y.

Thus our minimization MaOP, named O, is defined as $O = (O_1, O_2, O_3, O_4)$, where

$$\begin{aligned}
O_1(x) &= \mathrm{NRMSE}\left(I_D(V_{G_i},V_{D_j}), \widehat{I_D}(V_{G_i},V_{D_j},x)\right),\\
O_2(x) &= \mathrm{NRMSE}\left(V_S(V_{G_i},V_{D_j},x), \widehat{V_S}(V_{G_i},V_{D_j},x)\right),\\
O_3(x) &= 1 - R^2(V_{G_i},x),\\
O_4(x) &= \left|\widehat{V_T}(V_{G_i},x) - x_3\right| = \left|\widehat{V_T}(V_{G_i},x) - V_T\right|,\\
&\forall i \in \mathbb{Z} : 1 \le i \le g, \forall j \in \mathbb{Z} : 1 \le j \le d
\end{aligned} \tag{4.15}$$

Objective (O_1) allows us to accurately reproduce the experimental output and transfer characteristics with our model, using the parameters coded in (4.12). Objective (O_2) checks whether the trend of the $I_D - V_S$ curves extracted from (4.5) along with the parameters coded in (4.12) are physically valid. Objectives (O_3) and (O_4) are not mandatory [92], but serve as a guide in the search process to those solutions that approach to the trend given in (4.7).

Along with the MaOP definition (4.15), the procedure is composed by some simple constraints (other constraints are implicit in the search space definition) to converge to physically acceptable solutions:

(i) $\widehat{V_S}(V_{G_i},V_{D_j},x) \geq 0$

(ii) $M_C(V_{G_i}) > 0$.

As said previously, a detailed explanation of this evolutionary parameter extraction procedure can be found in Chapter 3 [111].

4.4. Results

Our model for OTFTs under illumination is now tested with two sets of experimental data from different OPTs [107, 129]. Output and transfer characteristics were measured at different light intensities in both sets of transistors. The procedure to analyze the two OPTs is the same and is detailed below.

In the two cases, every set of output characteristics ($I_D - V_D$ curves), measured at a different illumination intensity, is analyzed separately from the rest. First, the values of the parameters included in an individual of the population (4.12), that makes model (4.3)-(4.7) fulfill objectives (O_1), (O_2), (O_3) and (O_4), are extracted. Note (i) that the extraction procedure is independently applied to each set

Table 4.1: Parameter values of the NBBI OPT under different illumination conditions (k' is in A/V$^{2+\gamma}$, V_T and V_{SS} in V and $M_C(V_{G_i})$ in A/V^{m_k}).

x	*dark*	50 mW/cm^2	70 mW/cm^2	80 mW/cm^2
k'	7.25×10^{-12}	3.22×10^{-12}	2.42×10^{-12}	2.29×10^{-12}
γ	2.50×10^{-1}	2.50×10^{-1}	2.50×10^{-1}	2.50×10^{-1}
V_T	$8.57 \times 10^{+0}$	$-3.21 \times 10^{+1}$	$-5.40 \times 10^{+1}$	$-6.58 \times 10^{+1}$
V_{SS}	$2.59 \times 10^{+1}$	$2.85 \times 10^{+1}$	$2.52 \times 10^{+1}$	$2.87 \times 10^{+1}$
m_k	$1.00 \times 10^{+0}$	$1.00 \times 10^{+0}$	$1.00 \times 10^{+0}$	$1.00 \times 10^{+0}$
M_C(20 V)	5.98×10^{-9}	3.43×10^{-8}	–	6.87×10^{-8}
M_C(30 V)	9.68×10^{-9}	4.57×10^{-8}	–	8.30×10^{-8}
M_C(40 V)	1.56×10^{-8}	5.66×10^{-8}	7.79×10^{-8}	9.37×10^{-8}
M_C(50 V)	2.34×10^{-8}	6.64×10^{-8}	8.65×10^{-8}	1.03×10^{-7}
M_C(60 V)	3.22×10^{-8}	7.62×10^{-8}	9.46×10^{-8}	1.13×10^{-7}
M_C(70 V)	4.14×10^{-8}	8.37×10^{-8}	1.07×10^{-7}	1.25×10^{-7}
M_C(80 V)	5.06×10^{-8}	9.27×10^{-8}	1.21×10^{-7}	1.36×10^{-7}

of experimental $I_D - V_D$ curves; (ii) that equations (4.3)-(4.7) alone does not include any information about the light intensity; and (iii) that equations (4.10)-(4.11) are not used in the extraction procedure. The resulting values will be shown in a Table. Second, the values of the parameters V_T, α and $M_C(V_{G_i})$ are represented as a function of the light intensity. Then, we will check whether the evolution of these parameters with light intensity follow the trend proposed in (4.10)-(4.11). As a final test, the results of the model are compared with transfer curves measured at different light intensities.

4.4.1. NNBI OPT

The first set of experimental data correspond to a naphthalene bis-benzimidazole (NBBI) based OTFT designed as a phototransistor [107]. The output and transfer characteristics measured by the authors under dark and at 50, 70 and 80 mW/cm^2 white light intensities [107] are represented with symbols in Figs. 4.2 (top side) and 4.3, respectively. The transistor was fabricated with a top contact/bottom gate geometry in order to detect visible light. The substrate was an indium tin oxide (ITO) coated glass, which was patterned by etching with diluted HCl for a bottom gate electrode. The gate insulator layer was made of divinyl tetramethyl disiloxane-bis (benzo-cyclobutene) (BCB) with a capacitance per unit area $C_{ox} = 1.73$ nF/cm^2. The 60 nm Aluminum (Al) (purity 99.9 %) source and drain electrodes were deposited by thermal evaporation under high vacuum (2×10^{-6} mbar) to obtain high quality ohmic contacts with the NBBI thin films. The channel length is $L = 40$ μm and the channel width $W = 2000$ μm. The full protocols of the electrode deposition, substrate cleaning and surface passivation were given in Ref. [107, 131]. All current–voltage characteristics of the fabricated OTFTs [107] were measured in an inert gas atmosphere inside a glove box using Keithley 2400 source-meters. For electrical measurements under illumination, a solar simulator with a calibrated output light intensity and neutral density filters to change the light intensity were used [131].

Each set of $I_D - V_D$ curves of Fig. 4.2, corresponding to the four different illumination intensities, is

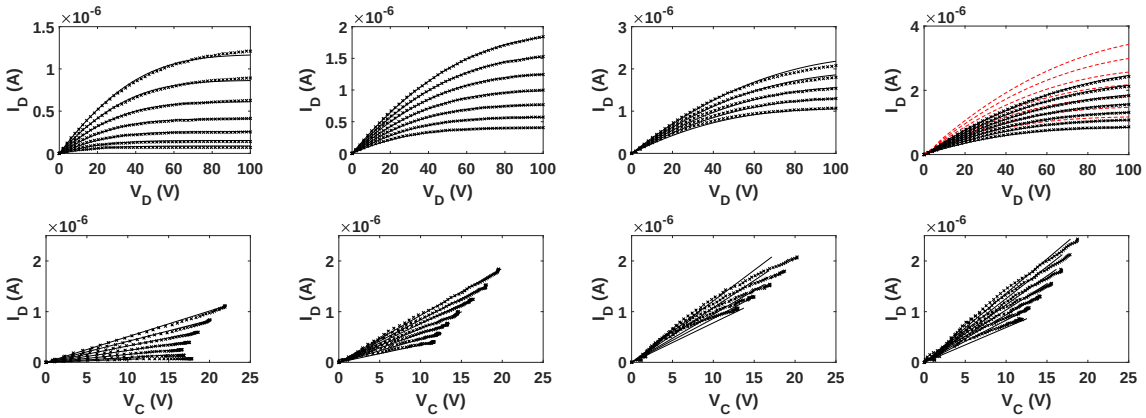

Figure 4.2: Output characteristics and contact $I_D - V_C$ curves in NBBI OPTs: (a) under dark, and under illumination at (b) 50 mW/cm^2, (c) 70 mW/cm^2 and (d) 80 mW/cm^2. Top side: Comparison of experimental $I_D - V_D$ curves ($\times$) and our calculations with (4.3) (solid lines). The red dashed lines in (d) are $I_D - V_D$ curves calculated with (4.3) neglecting the contact region ($V_S = 0$ V). Bottom side: Comparison of $I_D - V_C$ curves calculated with (4.5) ($\times$) and (4.6) (solid lines). In (a), (b) and (d), V_G is swept from 20 (bottom) to 80 V (top) with a 10 V step. In (c), V_G is swept from 40 (bottom) to 80 V (top) with a 10 V step.

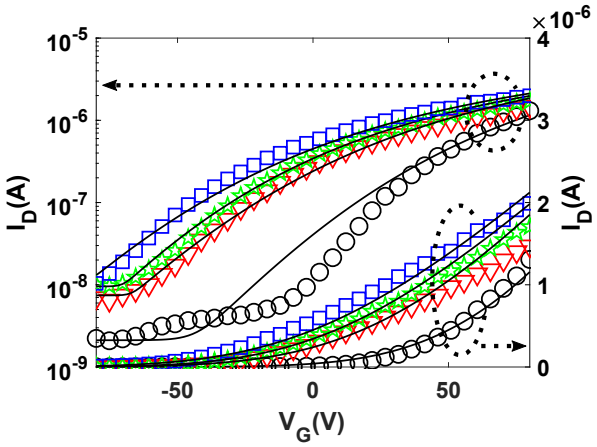

Figure 4.3: Comparison of experimental (symbols) transfer characteristics in saturation regime ($V_D = 80$ V) of NBBI OPTs, and our calculations with (4.3) (solid lines). Symbols: dark (black circles), illumination at 50 mW/cm^2 (red triangles), 70 mW/cm^2 (green stars) and 80 mW/cm^2 (blue squares). Note that the left y-axis is a log scale and the right y-axis is a linear scale for the same I_D values.

analyzed. The values of the parameters included in an individual of the population (4.12), that makes model (4.3)-(4.7) fulfill objectives (O_1), (O_2), (O_3) and (O_4) are extracted and shown in Table 4.1. Figure 4.2 shows the best fittings of objectives (O_1) and (O_2). The carrier mobility used in the fitting

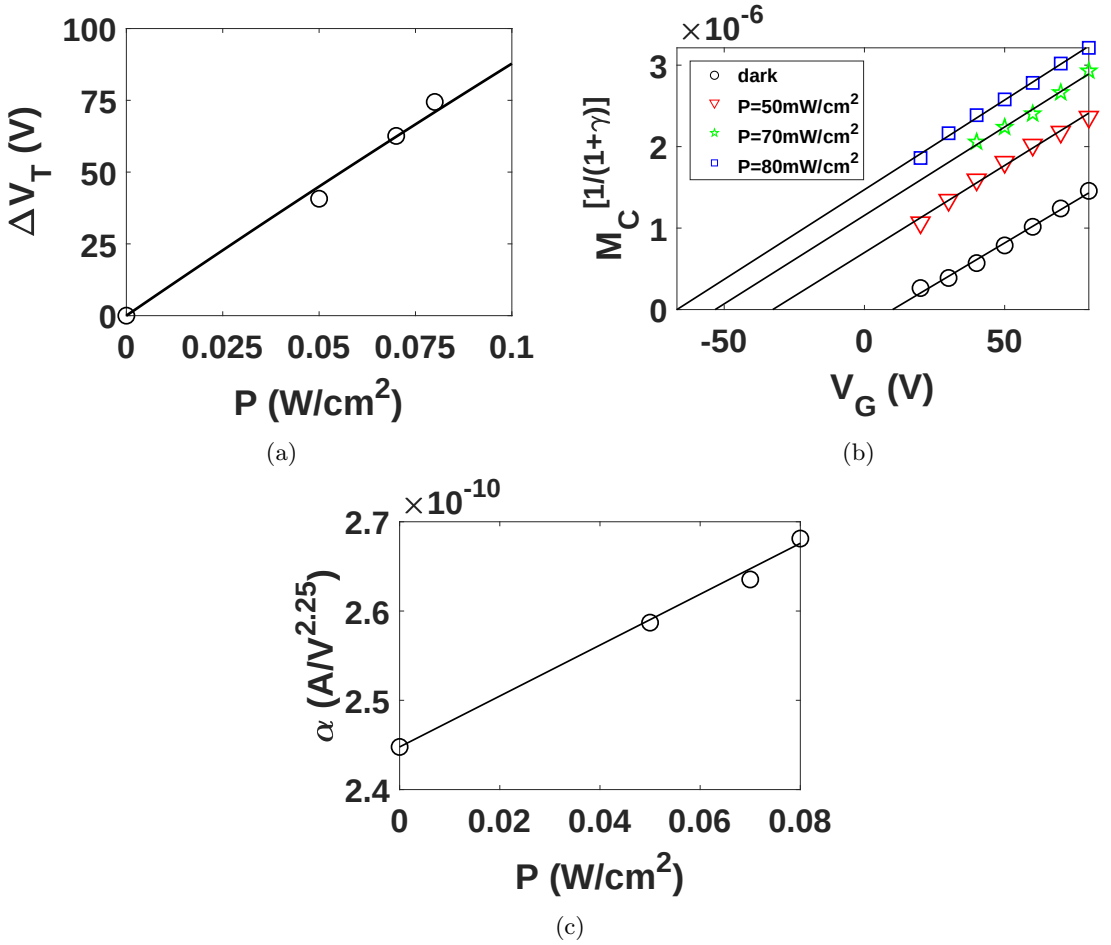

Figure 4.4: (a) Extracted values of ΔV_T (circles) and the trend of ΔV_T with illumination according to (4.10) (solid line). (b) Extracted values of $M_C(V_{G_i})^{1/(1+\gamma)}$ (symbols) and its fitting with (4.13) (solid lines). (c) Extracted values of α from (4.13) (circles) and the trend of α with illumination according to (4.11) (solid line) for the NBBI OPTs.

is $\mu_0 = 4.2{\times}10^{-3}$, $1.9{\times}10^{-3}$, $1.4{\times}10^{-3}$, $1.3{\times}10^{-3}$ cm^2/Vs under dark and at 50, 70 and 80 mW/cm^2 respectively. The values of the carrier mobility extracted with our model are consistent with those obtained in [107]. Our model, which includes the contact effects, provides more realistic values than those obtained with the ideal MOS model [40, 92]. In order to illustrate this fact, $I_D - V_D$ curves were calculated neglecting the contact effects ($V_S = 0V$). Fig. 4.2d shows in red dashed lines the calculated curves without contact effects for the highest illumination case. We have represented these curves only for this case for the sake of clarity of the rest of the figures. Moreover, this case was chosen since its contact effects are the lowest as they diminish with increasing light intensity. The comparison of Fig. 4.2d shows that neglecting the contacts produces a clear overestimation of the drain current, which is much more critical at lower illumination intensities and in dark.

Also note that the value of the mobility μ_0 decreases slightly from dark to illumination conditions

as observed in [89, Fig. 6]. However, the value of the mobility remains almost invariant at different illumination levels, in agreement with the discussion in Sec. 4.2.2. Overall, the value of the mobility does not follow a linear trend with the carrier concentration as proposed in Refs. [121, 122]. The slight decrease from dark to illumination can be linked to an increment of charge carrier concentration with illumination. At high charge carrier concentrations, the effect of the energetic disorder disappears and the mobility decreases slightly due to the lower density of unoccupied states available for the hopping transport [132].

A final comment on the value of the mobility should be focused on the extracted values of γ, which in our case do not depend on the light intensity P. Considering the physical meaning of γ being related to the width of a band tail distribution of the DOS, a variation of the distribution of the DOS would mean a modification of the internal structure or morphology of the semiconductor. In previous publications, some authors found that γ is independent of P [120]. In other cases, an increment of γ with P was determined [133]. The determination of γ using models that do not include the effect of the contacts can lead to errors in the value of γ. This can be seen in [39, Fig. 4a], in which the value of γ, extracted with a model that does not account for contact effects, decreases if the contact resistance increases. Under illumination, the contact resistance decreases. Thus, the apparent value of γ would increase with P if the contact resistance model is not included. At this time, it is recommended that a more detailed study of γ with P using a complete OPT model should be considered in future.

The extracted values of V_T, and the parameters that control the contact region ($M_C(V_{G_i})$ and α) are represented with symbols as a function of the light intensity in Fig. 4.4a, Fig. 4.4b and Fig. 4.4c, respectively. The solid line in Fig. 4.4a represents the fitting with (4.10) with $A = 3.46 \times 10^4$, $\eta/I_{Dd} = 2.57$ A^{-1}, $h\nu = 2.48$ eV. Fig. 4.4b shows the fulfillment of objectives (O_3) and (O_4). The solid lines in Fig. 4.4b are the fittings with (4.13), in which the values of $\hat{V}_T$ are practically the same to those found in Table 4.1. On average, the error between the values of V_T and $\hat{V}_T$ is less than 5.5 %. Finally, the solid line of Fig. 4.4c represents the fitting with (4.11) using $\beta_\alpha = 2.85 \times 10^{-10}$ A cm^2/(V$^{2.25}$ W) and $\alpha_0 = 2.45 \times 10^{-10}$ A/V$^{2.25}$.

The good agreement shown in Fig. 4.2 between the experimental (symbols) and estimated (solid lines) $I_D - V_D$ curves is corroborated in Fig. 4.3 with a good fitting of experimental transfer curves measured at different illumination conditions (symbols) and our estimation (solid lines).

4.4.2. EHPDI OPT

A second test of our model is done with [N,N'-di(2-ethylhexyl)-3,4,9,10-perylene diimide] (EHPDI) based OPTs [129] with a top contact/bottom gate geometry and BCB as gate insulator with a capacitance per unit area $C_{ox} = 1.73$ nF/cm^2. The output and transfer characteristics, measured by the authors under dark and at 70, 79.2 and 91.06 mW/cm^2 white light intensities [129], are represented with crosses in Fig. 4.5 (top side) and Fig. 4.6, respectively. Al metal electrodes (purity 99.9 %) with a thickness 60 nm were deposited on the EHPDI active layer by using the vacuum evaporator under 2×10^{-6} mbar. The channel length is $L = 40$ μm and the channel width $W = 2000$ μm. The full protocols of the substrate cleaning, and surface passivation were given in Ref. [129]. The electrical characterization of

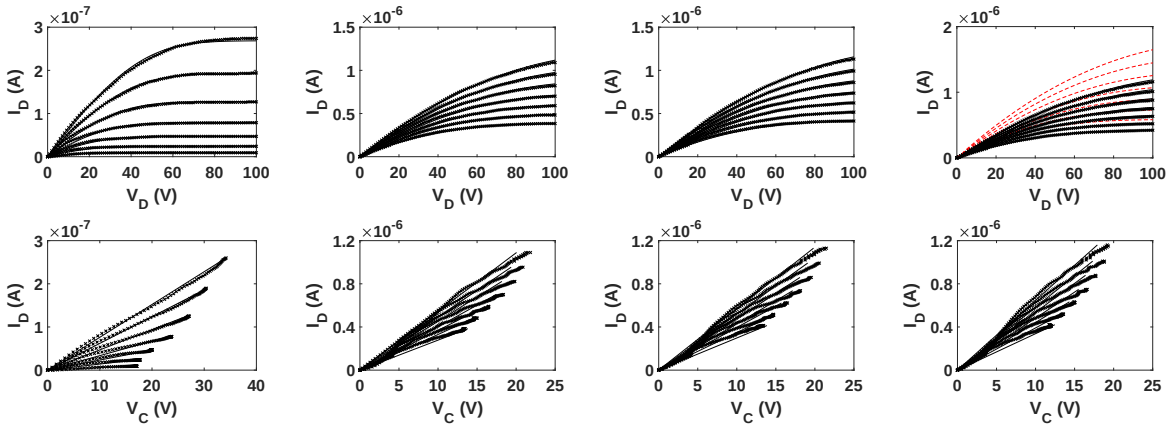

(a) (b) (c) (d)

Figure 4.5: Output characteristics and contact $I_D - V_C$ curves in EHPDI OPTs: (a) under dark, and under illumination at (b) 70 mW/cm^2, (c) 79.2 mW/cm^2 and (d) 91.06 mW/cm^2. Top side: Comparison of experimental $I_D - V_D$ curves ($\times$) and our calculations with (4.3) (solid lines). The red dashed lines in (d) are $I_D - V_D$ curves calculated with (4.3) neglecting the contact region ($V_S = 0$ V). Bottom side: Comparison of $I_D - V_C$ curves calculated with (4.5) ($\times$) and (4.6) (solid lines). In (a)-(d), V_G is swept from 20 (bottom) to 80 V (top) with a 10 V step.

Table 4.2: Parameter values of the EHPDI OPT (k' is in A/V$^{2+\gamma}$, V_T and V_{SS} in V and $M_C(V_G)$ in A/V^{m_k}) under different illumination conditions.

x	*dark*	70 mW/cm^2	79.2 mW/cm^2	91.06 mW/cm^2
k'	4.14×10^{-12}	1.04×10^{-12}	1.04×10^{-12}	1.01×10^{-12}
γ	2.50×10^{-1}	2.50×10^{-1}	2.50×10^{-1}	2.50×10^{-1}
V_T	$1.23 \times 10^{+1}$	$-6.81 \times 10^{+1}$	$-7.06 \times 10^{+1}$	$-7.07 \times 10^{+1}$
V_{SS}	$1.70 \times 10^{+1}$	$2.06 \times 10^{+1}$	$2.26 \times 10^{+1}$	$1.94 \times 10^{+1}$
m_k	$1.00 \times 10^{+0}$	$1.00 \times 10^{+0}$	$1.00 \times 10^{+0}$	$1.00 \times 10^{+0}$
M_C(20 V)	6.08×10^{-10}	2.77×10^{-8}	2.97×10^{-8}	3.37×10^{-8}
M_C(30 V)	1.40×10^{-9}	3.30×10^{-8}	3.47×10^{-8}	3.91×10^{-8}
M_C(40 V)	2.33×10^{-9}	3.68×10^{-8}	3.95×10^{-8}	4.41×10^{-8}
M_C(50 V)	3.36×10^{-9}	4.01×10^{-8}	4.28×10^{-8}	4.82×10^{-8}
M_C(60 V)	4.69×10^{-9}	4.52×10^{-8}	4.74×10^{-8}	5.36×10^{-8}
M_C(70 V)	6.19×10^{-9}	4.92×10^{-8}	5.20×10^{-8}	5.83×10^{-8}
M_C(80 V)	7.60×10^{-9}	5.43×10^{-8}	5.70×10^{-8}	6.47×10^{-8}

the fabricated device was conducted in an inert gas atmosphere inside a glove box.

The evolutionary procedure is applied to each set of $I_D - V_D$ curves of Fig. 4.5, corresponding to the four different illumination intensities. The values of the parameters used in the calculation to fulfill objectives (O_1), (O_2), (O_3) and (O_4) are extracted and shown in Table 4.2. Figure 4.5 shows the best fittings of objectives (O_1) and (O_2), in which a good agreement between the experimental (symbols) and calculated $I_D - V_D$ curves (lines) is observed and the extracted contact curves $I_D - V_C$ (symbols) show

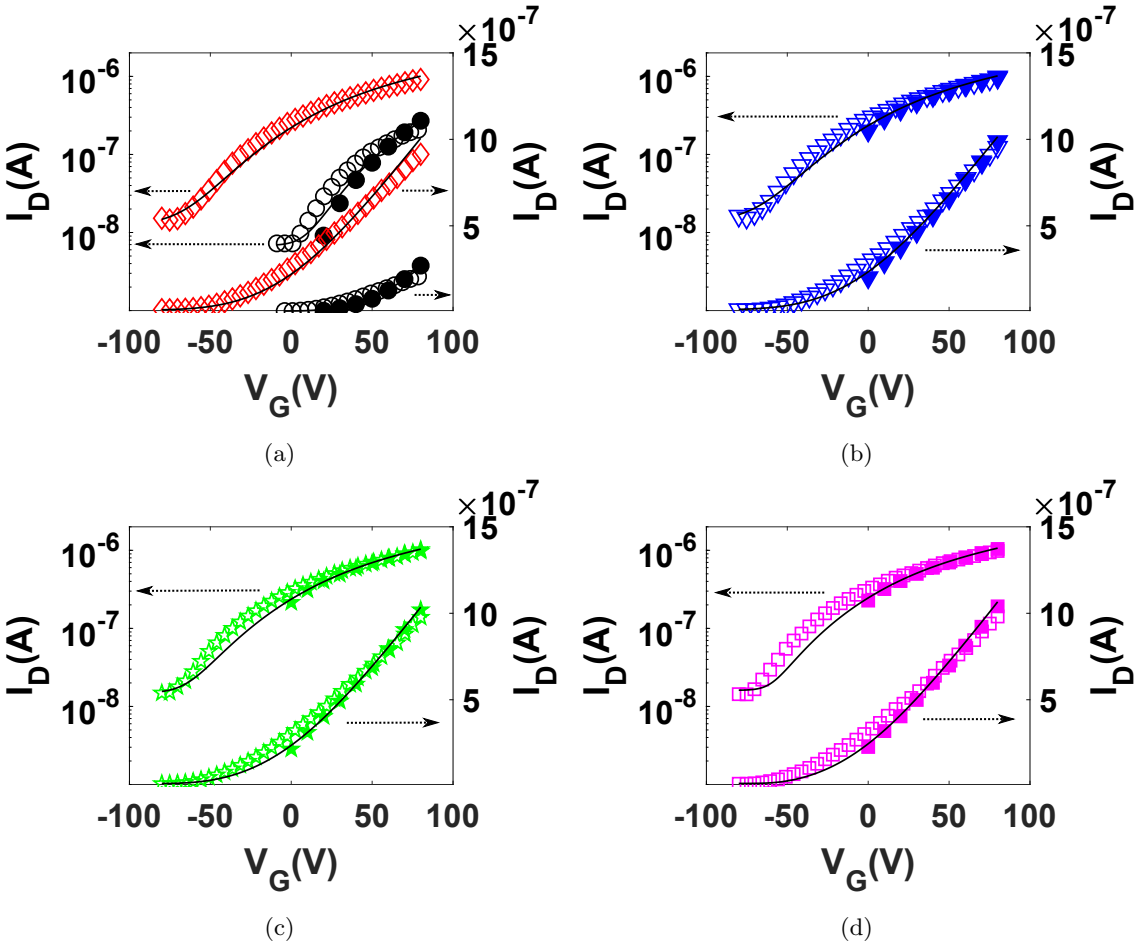

Figure 4.6: Comparison of experimental transfer characteristics in saturation regime ($V_D = 80$ V) of EHPDI OPTs (symbols) and our calculations with (4.3) (solid lines): (a) under dark (circles) and under illumination at 56.4 mW/cm^2 (diamonds), (b) 70 mW/cm^2, (c) 79.2 mW/cm^2 and (d) 91.06 mW/cm^2.The filled symbols correspond to values taken from the output characteristics.

a good physical meaning. In order to quantify the effects of the contacts, Fig. 4.5d also shows calculated $I_D - V_D$ curves neglecting the contact effects (red dashed lines). As in the previous case, neglecting the contact effects produces a clear overestimation of the drain current.

Once again, the good agreement observed in Fig. 4.5 between the experimental (symbols) and calculated (solid lines) $I_D - V_D$ curves is reinforced with the fitting of transfer $I_D - V_G$ curves in Fig. 4.6 (symbols for the experimental data and solid lines for our calculations). The filled symbols correspond to values taken from the output characteristics. These filled symbols are represented to indicate possible errors in the measurements due to factors not considered in the model, such as dynamic or hysteresis effects. It is clear that our calculations fit better the values taken from the output characteristics, in which the extraction procedure is carried out. In any case, it is remarkable how the whole experimental $I_D - V_G$ curves are reproduced with our calculations, including the one shown with diamonds in Fig.

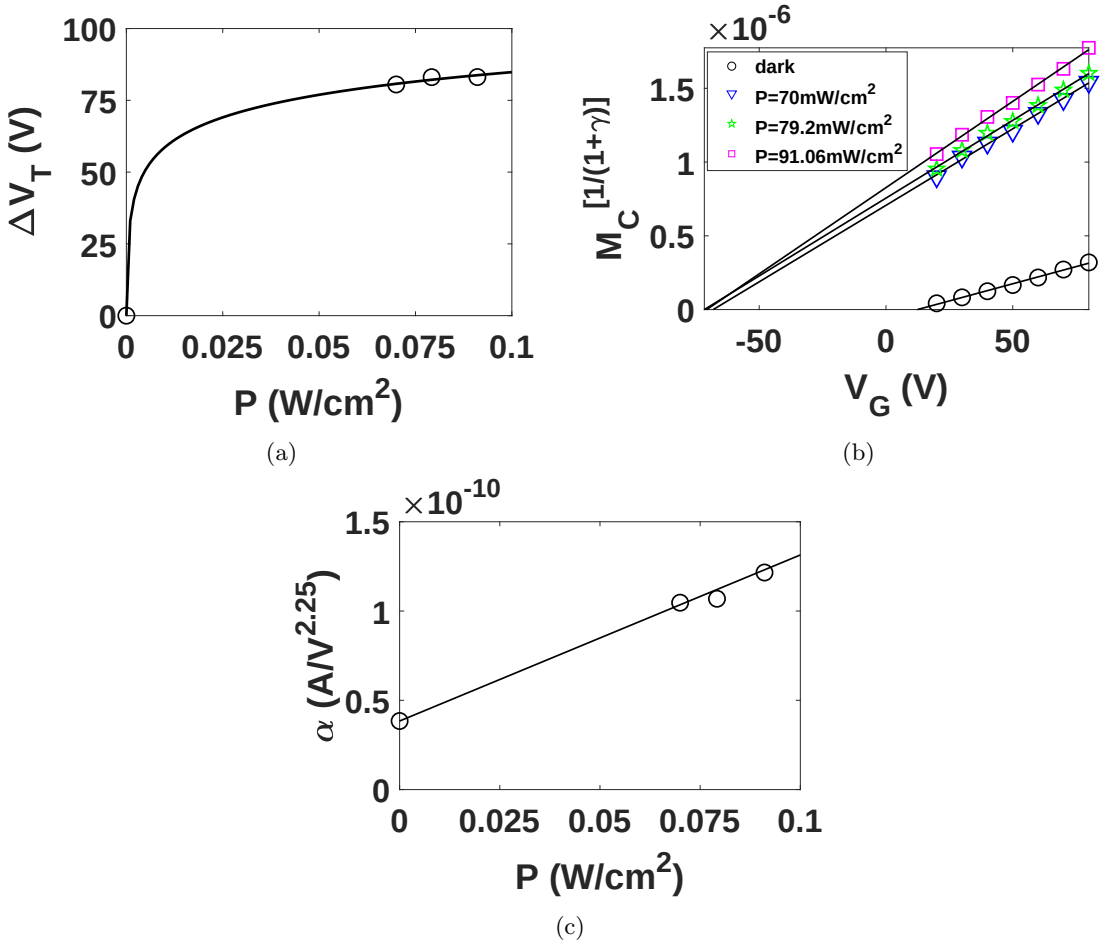

Figure 4.7: (a) Extracted values of ΔV_T (circles) and the trend of ΔV_T with illumination according to (4.10) (solid line). (b) Extracted values of $M_C(V_{G_i})^{1/(1+\gamma)}$ (symbols) and its fitting with (4.13) (solid lines). (c) Extracted values of α from (4.13) (circles) and the trend of α with illumination according to (4.11) (solid line) for the EHPDI OPTs.

4.6(a), which was measured under illumination at 56.4 mW/cm^2 (note that no output characteristics were analyzed at this illumination intensity).

The carrier mobility used in the fittings is $\mu_0 = 2.4\times10^{-3}$, 6.1×10^{-4}, 6.0×10^{-4}, 5.9×10^{-4} cm^2/Vs under dark and at 70, 79.2 and 91.06 mW/cm^2, respectively. These values are determined at $V_{GT} = 1$ V. At other values of V_{GT}, the mobility can increase one order of magnitude, in agreement with values obtained for other PDI based polymers [134, 135]. The evolution of the mobility with P is similar to the naphthalene bis-benzimidazole (NBBI) OPT: a constant value of γ with illumination and a slight decrease of μ_0 from dark to illumination is observed; however, the value of μ_0 remains invariant with further changes of P.

The extracted values of V_T, and the parameters that control the contact region ($M_C(V_{G_i})$ and α) are represented with symbols as a function of the light intensity in Fig. 4.7a, Fig. 4.7b and Fig.

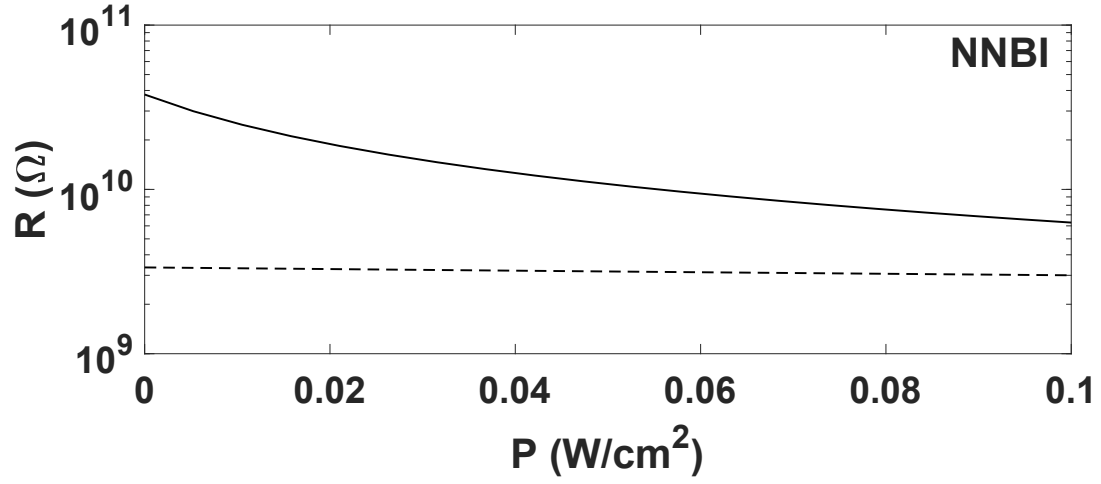

(a)

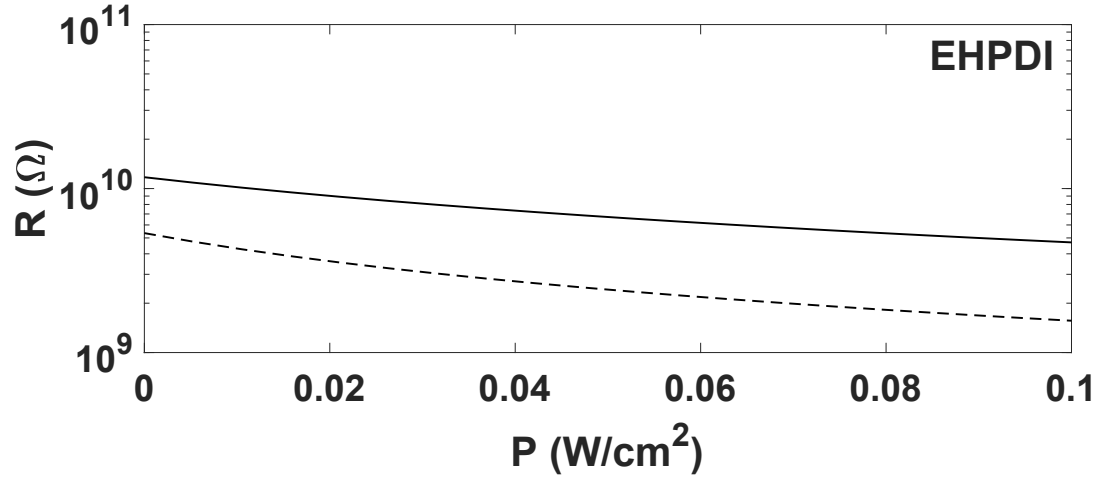

(b)

Figure 4.8: Evolution with illumination of the total resistance between source and drain (contact resistance plus channel resistance) (solid line) and the contact resistance (dashed line) determined in the subthreshold region (V_G = -80 V, V_D = 80 V) for (a) NBBI and (b) EHPDI based OPTs.

4.7c, respectively. The solid line in Fig. 4.7a represents the fitting with (4.10) with $A = 4.41 \times 10^2$, $\eta/I_{Dd} = 4.28 \times 10^4$ A^{-1}, $h\nu = 2.48$ eV. Fig. 4.7b shows the fulfillment of objectives (O_3) and (O_4). The solid lines in Fig. 4.7b are the fittings with (4.13), in which the values of $\hat{V}_T$ are practically the same to those found in Table 4.2. On average, the error between the values of V_T and $\hat{V}_T$ is less than 0.3 %. Finally, The solid line of Fig. 4.7c represents the fitting with (4.11) using $\beta_\alpha = 9.30 \times 10^{-10}$ A cm^2/(V$^{2.25}$ W) and $\alpha_0 = 3.84 \times 10^{-11}$ A / V$^{2.25}$.

4.4.3. Discussion

The excellent fittings of Figs. 4.4a, 4.4b and 4.4c, for the NBBI transistor, and of Figs. 4.7a, 4.7b and 4.7c, for the EHPDI transistor, show that the values extracted for V_T and the parameters that control the contact region ($M_C(V_{G_i})$ and α), which were obtained separately for each value of the illumination intensity, follow the trends predicted with our model. These fittings clearly indicate that the contact region of the phototransistor is highly sensitive to the photoconductive and photovoltaic effects.

The photovoltaic effect controls the electrical performance of both the intrinsic channel and the contact region when an accumulation channel exists along the transistor. It is detected with changes in the value of the threshold voltage. The photoconductive effect controls the conductivity of the contact and bulk regions of the semiconductor. Formerly, it was detected in the cut-off region by measuring the remnant current I_B. In this chapter, we have seen that it can also be detected analyzing the evolution of parameter α with the light intensity. In order to quantify how the photoconductive effect affects the contact region, we determine the value of the contact resistance at the cut-off region from (4.8) ($R_C = 1/M_C$, if $m_k = 1$). Then, this value is compared with the total resistance seen between source and drain also at the cut-off region:

$$R_{Total} = R_{channel} + R_C = \frac{V_D}{I_B} \tag{4.16}$$

where $R_{channel}$ is the equivalent resistance of the intrinsic channel in the subthreshold region. This comparison is carried out at different light intensities, with the transistor in deep subthreshold ($V_G = -80$ V) and the value of V_D is the one used in the transfer characteristics of Figs. 4.3 and 4.6.

The solid lines of Figs. 4.8a and 4.8b show the total resistance R_{Total} of the NBBI and EHPDI transistors, respectively, as a function of the light intensity, introducing the experimental values of I_B and V_D in (4.16). The value of the total resistance is one order of magnitude greater than the value of the contact resistance calculated from (4.8) (dashed lines). A typical contact length below 100 nm, as deduced by noncontact scanning-probe techniques [2], would produce a lower contact resistance. Thus, morphological differences between the bulk and contact region must play an important role in increasing the value of the contact resistance. Also, it is remarkable how the contact resistances decrease with illumination. In Fig. 4.8a, R_C decreases around 12 % from dark to illumination (hard to distinguish in the figure). However, the decrease of R_C in Fig. 4.8b is greater and follows the same trend as the total resistance. This comparison shows how sensitive our model is to determining the value of the contact resistance even in the cut-off regime of the transistor.

4.5. Conclusion

A model that describes how the contact region of organic phototransitors evolves with the incident optical power has been proposed. This model was included into a compact model for the current-voltage characteristics of OPTs, valid for all operation regions. The compact model works in combination with an evolutionary parameter extraction procedure that allows to reach parameter sets with physical

meaning. The model reproduces published experimental current-voltage curves in OPTs at different illumination conditions. Our study shows that the contact region of phototransistors is very sensitive to the photovoltaic and photoconductive effects. Therefore, compact models for phototransistors must include not only information about the contact region, but also how the contact region depends on the illumination intensity.

While contact effect in organic thin film transistor persists as a problem to be solved in these devices, models must incorporate this effect. In this regard, the way other OTFT based sensors react to different physical or chemical variables can be better understood with a better description on how the contact region depends on such variables, being this a topic for a future work.

5

Standard Model for the Contact Region of Organic Thin-Film Transistors

5.1. Introduction

Recently, many efforts have also been done on reducing the contact effects, such as testing different materials as contact electrodes [136, 137], the insertion of layers at the metal-semiconductor interface [138, 139], or the use of molecular doping [140]; and also on working toward an universal compact model of organic transistor technologies that includes the contact effects [20].

In order to examine the effect of the contacts, characterization methods to extract the contact resistance are necessary. These methods must work together with transistor models, which incorporate contact models and describe their current-voltage characteristics. Overall, transistor models must be consistent with the underlying physics. In particular, the contact models must be adapted to different physical mechanisms that limit the charge injection through a metal-organic structure, such as space-charge limited conduction, thermionic emission and the Fowler–Nordheim tunneling [3, 141].

A generic analytical model for the current–voltage characteristics of OTFTs was derived in [68, 69], which allows a functional model of the carrier injection through the source contact. Later works have specified this functional model to situations in which one conduction mechanism is dominant, such as the cases of space charge limited transport in low energy contact-barriers [4] or injection limited transport in Schottky barriers [19, 37, 142, 143]. Despite these previous efforts, there is no standard OTFT compact model that unifies all the different physical phenomena that take place at the contact region of the OTFT. In order to choose the appropriate contact model, the expert user or decision maker (DM) should identify, in the first place, which physical phenomenon is dominant in the contact region of the OTFT. Given this lack of standardization, and in order to guide and automate the decision-making, the main objective to accomplish in this chapter is the proposal of a standard contact model valid for different injection mechanisms. For that purpose, the functionality of the contact model, initially proposed in [4], is extended, giving way to a standard semi-empirical contact model. All this is detailed in Section 5.2.

In Section 5.3, the validity of the model is checked with the evolutionary procedure presented in Chapters 2 and 3, which extracts the parameters of the model and current-voltage ($I_D - V_C$) curves at the contact [92, 111, 144]. The results of the procedure, which analyzes output characteristics measured in transistors with the same channel length, is compared to the results of other methods based on measurements taken in transistors with different lengths. We demonstrate that, even in very-short length transistors, in which the contact resistance may be comparable to or even greater than the channel resistance, our procedure produces results comparable to methods in which a collection of transistors with short and long channels are necessary [19, 145–147]. The conclusions of this chapter are finally presented in Section 5.4.

5.2. Theory

5.2.1. Models for the contact region of OTFTs

The physical mechanisms that take place at the contact region of an OTFT influence the final functional appearance of a model that aims to describe the current-voltage characteristics of the device. This is the case of a widely-used [37, 41, 92, 144, 148–152] generic model for OTFTs [68, 69]:

$$\begin{aligned} I_D &= k_0 \frac{W}{L} \frac{V_{EODR}(V_G, V_S)^{(2+\gamma)} - V_{EODR}(V_G, V_D)^{(2+\gamma)}}{2+\gamma}, \\ k_0 &= \mu_0 C_{ox};\ V_{EODR}(V_G, V) = V_{SS} \ln\left[1 + \exp\left(\frac{V_G - V_T - V}{V_{SS}}\right)\right], \end{aligned} \tag{5.1}$$

which includes an electric field dependent mobility

$$\mu = \mu_0 (V_G - V_T)^{\gamma}, \tag{5.2}$$

with V_T being the threshold voltage, V_D and V_G the drain and gate terminal voltages, respectively, W and L the channel width and length, respectively, and C_{ox} the capacitance per unit area of the oxide. V_{SS} is a voltage parameter related to the steepness of the subthreshold characteristics of the TFT, μ_0 is the mobility-related parameter expressed as $\mathrm{cm}^2/(\mathrm{V}^{1+\gamma}\mathrm{s})$, and $\gamma = 2(T_0/T - 1)$ is the mobility enhancement factor, which is a semi-empirical parameter that depends on the temperature T. In order to provide a single value for the voltage dependent mobility, the mobility is evaluated at $V_{GT} = V_G - V_T = 1$ V, thus $\mu(V_{GT} = 1\ \mathrm{V}) = \mu_0$ in $\mathrm{cm}^2/(\mathrm{Vs})$. This compact model is able to describe all operation modes of the transistor: triode, saturation, subthreshold or even reverse biasing.

The model (5.1) allows for a functional expression of the carrier injection as $V_S \equiv V_C = V_C(I_D, V_G)$. Different expressions have been developed in the past, depending on the dominant conduction mechanism through the contact. The cases controlled by space charge limited transport in low energy contact-barriers [4] or injection limited transport in Schottky barriers [19, 37, 142, 143] are reviewed below.

5.2.1.1. Space-charge limited transport

A simple model for the contact region of OTFTs in which the carrier injection is space charge limited is [4]:

$$\begin{aligned} I_D &= M_C \times {V_C}^{m_k}, \\ \forall m_k &\in \mathbb{Z} : 1 \leq m_k \leq 2. \end{aligned} \tag{5.3}$$

The application of the combined model (5.1) and (5.3) can be found in different kinds of OTFTs [39–44, 90, 92, 118].

The physical origin of model (5.3) lies behind the solution of the transport equations in a metal-organic structure, which provides the following relation between the current density j and the applied voltage V_C [3, 71, 93, 141]:

$$V_C = \left(\frac{2}{3}\right)\left[\frac{2j}{\epsilon\mu\theta}\right]^{1/2}\left[(x_c + x_p)^{3/2} - (x_p)^{3/2}\right]$$
$$x_p \equiv \frac{j\epsilon\theta}{2\mu[\theta qp(0)]^2};\ j = I_D/S, \tag{5.4}$$

where $qp(0)$ is the charge density at the metal-organic interface, θ is the ratio of free to total charge density, $q\theta p$ is the free charge density, S is the cross section of the channel where the drain current I_D flows, x_p is a characteristic length defined as the point from the contact interface towards the organic film, at which the charge density $qp(x_p)$ decays to $qp(0)/\sqrt{2}$, ϵ is the organic dielectric constant and x_C is the length of the contact region in the organic material. Equation (5.4) was demonstrated to have two asymptotic trends: a linear or Ohmic behavior if the characteristic length x_p is a few times larger than the contact length x_C

$$I_D \approx \frac{S\theta qp(0)\mu}{x_C}V_C \equiv \frac{1}{R_C} \times V_C^1, \tag{5.5}$$

and a quadratic behavior (Mott-Gurney law) if x_p is much smaller than x_C [3, 39]

$$I_D \approx \frac{9\epsilon\theta\mu S}{8x_C^3}V_C^2 \equiv M \times V_C^2 \tag{5.6}$$

Equations (5.5) and (5.6) are the limit cases of (5.3) with ($m_k = 1$, $M_C = 1/R_C$) and ($m_k = 2$, $M_C = M$), respectively. The parameter M_C usually shows the following trend with the gate voltage [4]:

$$M_C = \alpha(V_G - V_T)^{1+\gamma}, \tag{5.7}$$

where α is a proportionality constant. The subthreshold regime can be incorporated into (5.7) by an asymptotically interpolation function [144]

$$M_C = \alpha V_{SS} \ln\left[1 + \exp\left(\frac{V_G - V_T}{V_{SS}}\right)\right]^{1+\gamma}. \tag{5.8}$$

The physical origin of this relation is found in the dependence with $(V_G - V_T)$ of both the mobility and the free charge density along the conducting channel, including the contact region [42]. The relation (5.7) has been checked experimentally in OTFTs that are free of hysteresis and free of local non-uniformities in the contact region [39, 40, 42, 90, 92, 144].

5.2.1.2. Schottky-barrier limited injection

Different $I_D - V_C$ contact curves extracted in OTFTs resemble those of a reverse biased leaky diode. For these cases, the $I_D - V_C$ relation can be modeled as a reverse-biased Schottky-diode [19]:

$$I_D = -I_0 \exp\left[\left(\frac{V_C}{V_0}\right)^{\sigma}\right]\left\{\exp\left[-\left(\frac{V_C}{V_N}\right)\right] - 1\right\}, \tag{5.9}$$

where I_0 is a gate-modulated diode-reverse-current, $V_N = (\eta kT)/q$, q is the elementary charge, η is the diode quality factor, k is the Boltzmann constant and T is the absolute temperature. The barrier lowering induced by the Schottky effect is assumed in the term $(V_C/V_0)^\sigma$. The Schottky effect, which depends on the electric field at the junction is assumed to be dependent on the contact voltage V_C, and V_0 and σ are fitting parameters [19]. The assumption of a contact-voltage dependent barrier lowering is also found in the study of different semiconductors, such as Pt/Ga_2O_3 diode contacts [153].

Despite the justified physical origin of the contact model (5.9) and being successfully tested in different OTFTs [19, 37, 143, 148, 154], authors regard it just as a mathematical expression able to reproduce the $I_D - V_C$ curves and, consequently, the extracted diode parameters are considered as effective model parameters [142].

5.2.1.3. Semi-empirical standard contact model

The last statement of the previous section suggests that other functional expressions would also be able to reproduce the $I_D - V_C$ curves of Schottky-barrier limited contacts. In this regard, and in order to incorporate different mechanisms under the same unified standard model, we propose to extend the validity of model (5.3) outside the range $1 \leq m_k \leq 2$, and include the values $0 < m_k < 1$:

$$\begin{aligned} I_D &= M_C \times {V_C}^{m_k}, \\ \forall m_k &\in \mathbb{Z} : 0 < m_k \leq 2. \end{aligned} \tag{5.10}$$

Note that the expression (5.10) is a concave function if $1 \leq m_k \leq 2$, and a convex function if $0 < m_k < 1$. From a mathematical point of view, expression (5.10) with $0 < m_k < 1$ is an option to reproduce $I_D - V_C$ curves in OTFTs dominated by Schottky barriers. Note also that the use of model (5.10) in the range $1 \leq m_k \leq 2$ is physically justified as mentioned above for the space-charge dominated injection. However, since there is no physical justification for Schottky-barrier dominated injection, this would result into a semi-empirical model.

This is not the first time space-charge and injection limited currents in metal-organic contacts are connected under the same model. Previous numerical studies have shown that both currents can be described by exclusively solving the transport equations in the semiconductor with the only difference of specific boundary values of the free charge density at the metal–organic interface. In addition, these boundary values for the free charge density are modeled by a unified analytical expression that relates the charge density at the interface with the current density though the contact [155].

Thus, the objectives of this chapter are to check the validity of this extended model (5.10) and to analyze the advantages of this unified model over the existing ones. The first advantage is that a single expression unifies the different mechanisms related to the injection and transport through the contacts of OTFTs. The second advantage lies behind the parameter extraction procedure that runs parallel to the compact OTFT model (5.1) and (5.10), which is introduced in the next section.

5.2.2. Determination of the voltage drop at the contact

In the past, many research efforts have been made in order to quantify the contact effects of OTFTs, since these effects make difficult the extraction of the intrinsic parameters of the transistor. In order to determine the mobility and the threshold voltage independently of the magnitude of the contact resistance, four-probe measurements are proposed [156]. The parameter extraction techniques vary depending on whether they analyze single or multiple transistors; whether they focus on extracting the contact resistance or the voltage drop at the contact region (note that the voltage drop at the contact region is not necessarily linear, as shown in the previous sections); or whether they extract information of the contact region from current-voltage ($I - V$) characteristics or from the voltage profile along the whole channel, as in the case of surface potentiometry [157]. Some of these procedures are reviewed in [6], including the transmission line method (TLM), which requires multiple devices with different channel lengths to determine the contact resistance [145, 146], or Impedance spectroscopy (IS) [158], which requires a single device and a proper equivalent circuit model for the OTFT in order to determine its contact resistance and evaluate the actual charge carrier mobility.

Other extraction procedures are directly linked to the generic model for OTFTs (5.1). One of these methods determines the channel conductance of long channel devices from experimental transfer characteristics measured at low drain voltages, in which the gradual channel approximation is validated. Then, the channel conductance is used to determine the voltage drop at the source contact in short channel devices [19, 37]. Another parameter extraction procedure was proposed for single OTFTs operating in the linear regime, in which a proper sequence of mathematical functions derived from measured I–V characteristics are used [118].

Once again, in this chapter we use the evolutionary procedure presented in Chapters 2 that analyzes only the output characteristics measured in a single short-length transistor [92]. The choice of this evolutionary procedure is determined firstly by its successful application to different OTFTs [92, 111, 144]. Secondly, the decision making is fully guided. Thus, the extraction procedure is expected to automatically detect the mechanism that dominates the injection through the contact, a Schottky-barrier limitation if $0 < m_k < 1$ or a space-charge limitation if $1 \leq m_k \leq 2$. Finally, as the parameters of the transistor can be extracted from a single device, it can compete with other well known extraction procedures that need multiple transistors with different channel lengths. In the results section, we will check that the parameters extracted from the analysis of a short-channel transistor can be used to reproduce the output characteristics measured in a long-channel device.

It has to be noted that there is no technical difference between the use of (5.1), with (5.3), as it was proposed Chapters 2, or with (5.10), as used in this chapter, or even with (5.9), in case (5.9) would be preferred over (5.10). The number of parameters to be extracted would be the only difference.

5.3. Results and Discussion

In order to validate the versatility of the standard contact model (5.10), it is tested with transistors with Schottky-barrier-limited contacts ($0 < m_k < 1$), space-charge-limited contacts ($1 \leq m_k \leq 2$) and

even in transistors, that exposed to chemical treatments, their contact region is altered in such a way that any of the previous cases can be detected ($0 < m_k \leq 2$). In these situations, the OTFT model (5.1) and (5.10), in combination with the evolutionary procedure defined in Chapter 2 [92], can be seen as an effective diagnose tool.

Four experiments (A, B, C and D) have been defined, being implemented in ECJ [88]. This evolutionary tool has been run in a CentOS cluster with 19 computation nodes, each one with two Intel Xeon E5520 processors at 2.7 GHz. It was executed using only one node (16 threads).

5.3.1. Experiments A: Schottky-barrier-limited contacts

In this first set of experiments, we analyze the experimental output characteristics of 6,13-bis(triisopropyl-silylethynyl) (TIPS) pentacene based OTFTs [19], shown with symbols in Figs. 5.1a and 5.1b. They were measured in OTFTs with staggered top-gate configuration, with a channel width of 2000 μm, and with short and long-channel lengths of 10 and 200 μm, respectively. These OTFTs were fabricated at CEA-LITEN, using printing processes on heat stabilized, low roughness polyethylenenaphtalate PEN foils (125 μm thick). The source and drain gold contacts were defined by laser ablation. The p-type semiconductor is a solution processed TIPS-pentacene. The fluoropolymer gate dielectric (1.2 μm thick) and the Ag gate electrode are both deposited by screen printing. The full protocols of the fabrication process are in [19].

The main objective of this section is to check the suitability of our model (5.1) and (5.10), in combination with our evolutionary algorithm (Chapter 2) [92], to characterize single-channel-length OTFTs with Schottky-barrier-limited contacts. To do this, we propose the following four experiments, grouped into two different evolutionary configurations: (*A1*) the evolutionary procedure uses (5.1) and (5.10), and (*A2*) the procedure uses (5.1) and (5.9). First, these two configurations perform a single-transistor parameter extraction [92] (Experiments *A1-1* and *A2-1*). They extract respective OTFT parameters from the output characteristics of the short-channel transistor shown in Fig. 5.1a (symbols). Subsequently, they check whether the output characteristics of the long channel transistors, shown in Fig. 5.1b, can be reproduced with our calculations. Second, these configurations perform a multiple-transistor parameter extraction [111] (Experiments *A1-2* and *A2-2*). They extract respective OTFT parameters by analyzing simultaneously the output characteristics of both short- and long-channel transistors shown in Figs. 5.1a and 5.1b.

Once the experiments are executed, the values of the parameters of the models are determined. These values are collected in Table 5.1. They are introduced in (5.1) and (5.10) or in (5.1) and (5.9) to calculate the numerical output characteristics. Finally, they are compared to the experimental output characteristics and the NRMSE are computed. The values of the NRMSE are seen in Table 5.2.

No significant differences are found in Table 5.1 for the extracted common parameters (k_0, γ, V_T and V_{SS}), except for γ. The values of γ are different, but $\gamma \ll 1$. From a practical point of view $\gamma \approx 0$. It means that the mobility is almost independent on the gate voltage in the four cases. The fitting errors of the different experiments A shown in Table 5.2 are also very similar. All these facts reinforce the similarity of the contact models (5.9) and (5.10). The error in Experiments *A1* is a bit lower than

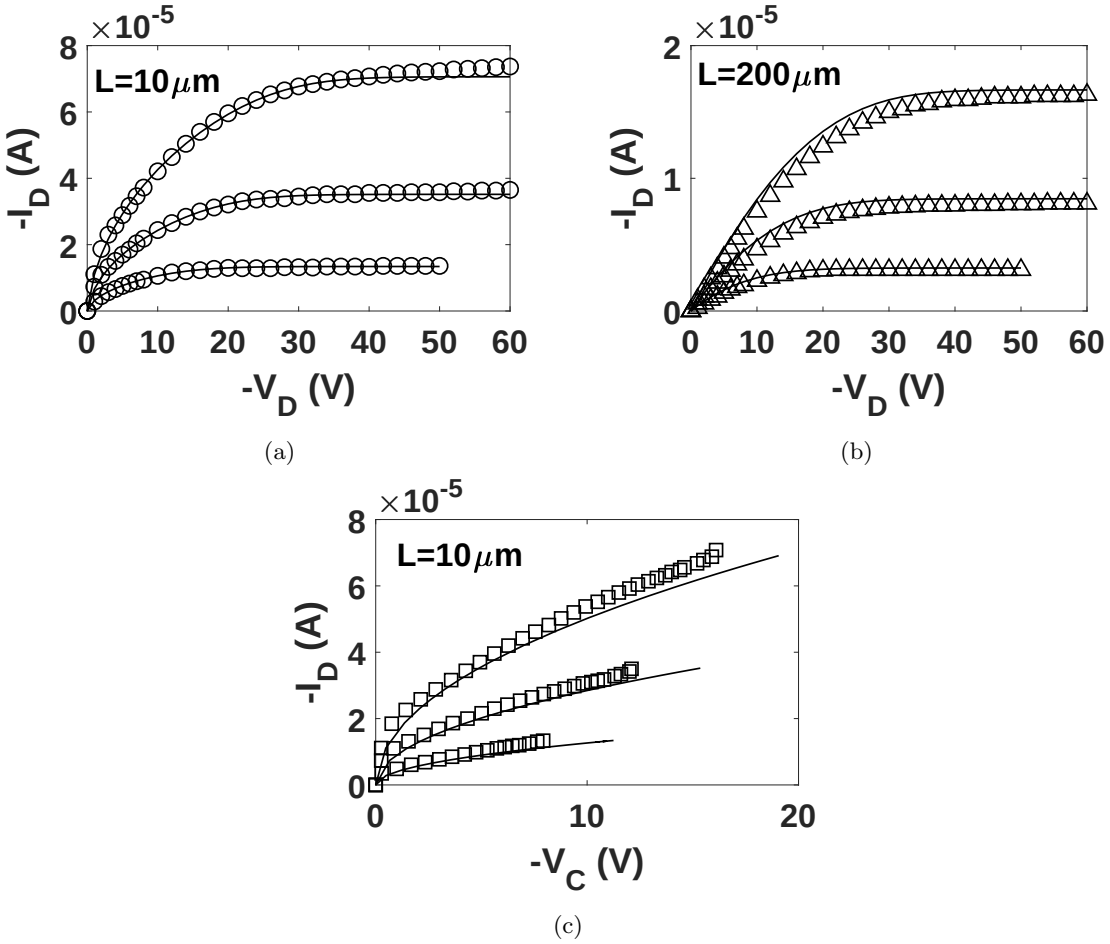

Figure 5.1: Experiment *A1-1*. (a), (b) Comparison of experimental $I_D - V_D$ curves measured at different V_G values [19] (symbols) and our calculations with (5.1) and (5.10) (solid lines). (c) $I_D - V_C$ curves extracted with (5.1) and (5.10) at different V_G (solid lines); the symbols show the results extracted in [19]. $V_G = -30, -40, -50$ V from bottom to top.

the error in experiments *A2*. Also, the error when using multiple transistors is reduced, but not in a significant way. As stated in Chapter 2 [92], the more quantity of data and time are available, the more accurate results will be reached with the evolutionary procedure.

For the sake of clarity, only the results of Experiment *A1-1* are represented in Figs. 5.1a and 5.1b (solid lines). Note that in this experiment *A1-1*, the parameters of the model (5.1) and (5.10) are extracted by analyzing the experimental data of the short-channel transistor, and subsequently used to reproduce the experimental data of the long-channel transistor. A very good agreement between the experimental and calculated data is observed in these figures. The $I_D - V_C$ curves extracted in this experiment are depicted with solid lines in Fig. 5.1c. They are similar to those calculated in [19] (symbols). It is confirmed that the OTFT contact is Schottky-barrier limited, since the evolutionary procedure converged to a parameter set with $m_k < 1$. The extracted value for the carrier mobility is

Table 5.1: Values of parameters extracted in Experiments A (k_0 is in A/V$^{2+\gamma}$, V_T in V, V_{SS} in V, $M_C(V_G)$ in A/V^{m_k}, V_0 in V, V_N in V and I_0 in A).

	Experiment			
x	*A1-1*	*A2-1*	*A1-2*	*A2-2*
k_0	3.0×10^{-09}	2.4×10^{-09}	2.9×10^{-09}	2.3×10^{-09}
γ	3.0×10^{-03}	3.9×10^{-08}	7.8×10^{-09}	7.4×10^{-02}
V_T	$-1.6 \times 10^{+01}$	$-1.9 \times 10^{+01}$	$-1.6 \times 10^{+01}$	$-1.7 \times 10^{+01}$
V_{SS}	$-7.2 \times 10^{+00}$	$-1.0 \times 10^{+01}$	$-9.1 \times 10^{+00}$	$-9.9 \times 10^{+00}$
m_k	4.9×10^{-01}		4.7×10^{-01}	
$M_C(-30V)$	4.0×10^{-06}		4.1×10^{-06}	
$M_C(-40V)$	9.1×10^{-06}		9.6×10^{-06}	
$M_C(-50V)$	1.6×10^{-05}		1.8×10^{-05}	
V_0		3.0×10^{-01}		8.9×10^{-01}
V_N		8.2×10^{-02}		6.7×10^{-01}
σ		2.4×10^{-01}		2.5×10^{-01}
$I_0(-30V)$		1.3×10^{-06}		1.9×10^{-06}
$I_0(-40V)$		3.1×10^{-06}		4.6×10^{-06}
$I_0(-50V)$		5.3×10^{-06}		8.5×10^{-06}

Table 5.2: Errors obtained after fitting the experimental output characteristics in Experiments A.

	NRMSE		Average
Exp.	$L = 10\ \mu m$	$L = 200\ \mu m$	NRMSE
A1-1	3.5×10^{-02}	1.1×10^{-01}	7.1×10^{-02}
A2-1	1.7×10^{-02}	4.3×10^{-01}	2.2×10^{-01}
A1-2	3.2×10^{-02}	3.9×10^{-02}	3.6×10^{-02}
A2-2	6.4×10^{-02}	3.0×10^{-02}	4.7×10^{-02}

$\mu_0 = 1.91$ cm^2/Vs, which is consistent with the result reported in [19], in which a value between 1.4 and 2 cm^2/Vs was estimated. Also the extracted threshold voltage $V_T = -16$ V is consistent with the one given in [19], which was reported in the range -10 and -15 V. This study shows that the procedure *A1-1* based on the analysis of a single short-channel transistor is completely equivalent to other procedures in which multiple-length transistors are needed. Most importantly, the standard model (5.10) is a good solution to model Schottky-barrier-limited contacts.

5.3.2. Experiments B: Schottky-barrier-limited contacts

In order to check that the previous results were not fortuitous, a new test on OTFTs with Schottky-barrier-limited contacts is carried out. In this set of experiments, we analyze the experimental output and transfer characteristics of Lisicon SP500 based OTFTs [143], shown with symbols in Figs. 5.2a-5.2d. They were measured in short- and long-channel OTFTs with a channel width of 1000 μm and lengths of 5 and 800 μm, respectively.

The OTFTs were fabricated in a top-gate staggered-contact configuration with a p-type polymer. The source and drain electrodes were made of 30 nm thick gold patterned directly by photolithography on Gen1-size PEN foils. In order to ensure a clean surface and low contact resistance, a short oxygen plasma treatment was applied prior to the semiconductor deposition. The semiconductor thickness is in the range of 45 nm. A low-k dielectric (Lisicon D320) with a thickness around 500 nm and an approximate capacitance per unit area of 3.7 nF/cm^2 is gravure-printed. Full details about these device fabrication are found in [143].

As in the previous case, four experiments, grouped into two different evolutionary configurations, are considered: (*B1*) the evolutionary procedure uses (5.1) and (5.10), and (*B2*) the procedure uses (5.1) and (5.9).

Experiments *B1-1* and *B2-1* perform a single-transistor parameter extraction [92]. First, they extract respective OTFT parameters from the output characteristics of the short-channel transistor shown in Fig. 5.2a. Then, they check whether the output characteristics of the long-channel transistors, shown in Fig. 5.2c can be reproduced with our calculations. As an additional test, the experimental transfer characteristics of the short- and long-channel transistors shown with symbols in Figs. 5.2b and 5.2d, respectively, are also fitted with our calculations. The solid lines of Figs. 5.2a-5.2d show the results of Experiment *B1-1*. The $I_D - V_C$ curves extracted in Experiment *B1-1* with (5.10) are shown in Fig. 5.2e. The output and transfer characteristics and the $I_D - V_C$ curves calculated in the rest of experiments are very similar (not shown for clarity). The evolutionary procedure converges to a solution with $m_k < 1$.

Experiments *B1-2* and *B2-2* perform a multiple-transistor parameter extraction [111]. They extract respective OTFT parameters by analyzing simultaneously the output characteristics of both short- and long-channel transistors shown in Figs. 5.2a and 5.2c.

The parameters of the transistor and the contact region, extracted in all these experiments, are in Table 5.3. As in Experiments *A*, the values of the common parameters (k_0, γ, V_T and V_{SS}) for both configurations *B1* and *B2* are quite similar. The carrier mobility of these fittings is $\mu_0 = 1.6$ cm^2/Vs, also similar to that reported in [143] (2.2 cm^2/Vs). The value of V_T is in the range [-4.0,-2.8] V, consistent with $V_T = -3.5$ V reported in [143]. The values of the NRMSE of the different comparisons between the experimental output characteristics and our calculations are found in Table 5.4. This table shows again that: Experiment *B1-1* is a very valid option to characterize single short-channel length transistors; the use of (5.10) or (5.9) is indifferent; and the use of multiple channel length transistors improves, but not significantly the fittings with the experimental data.

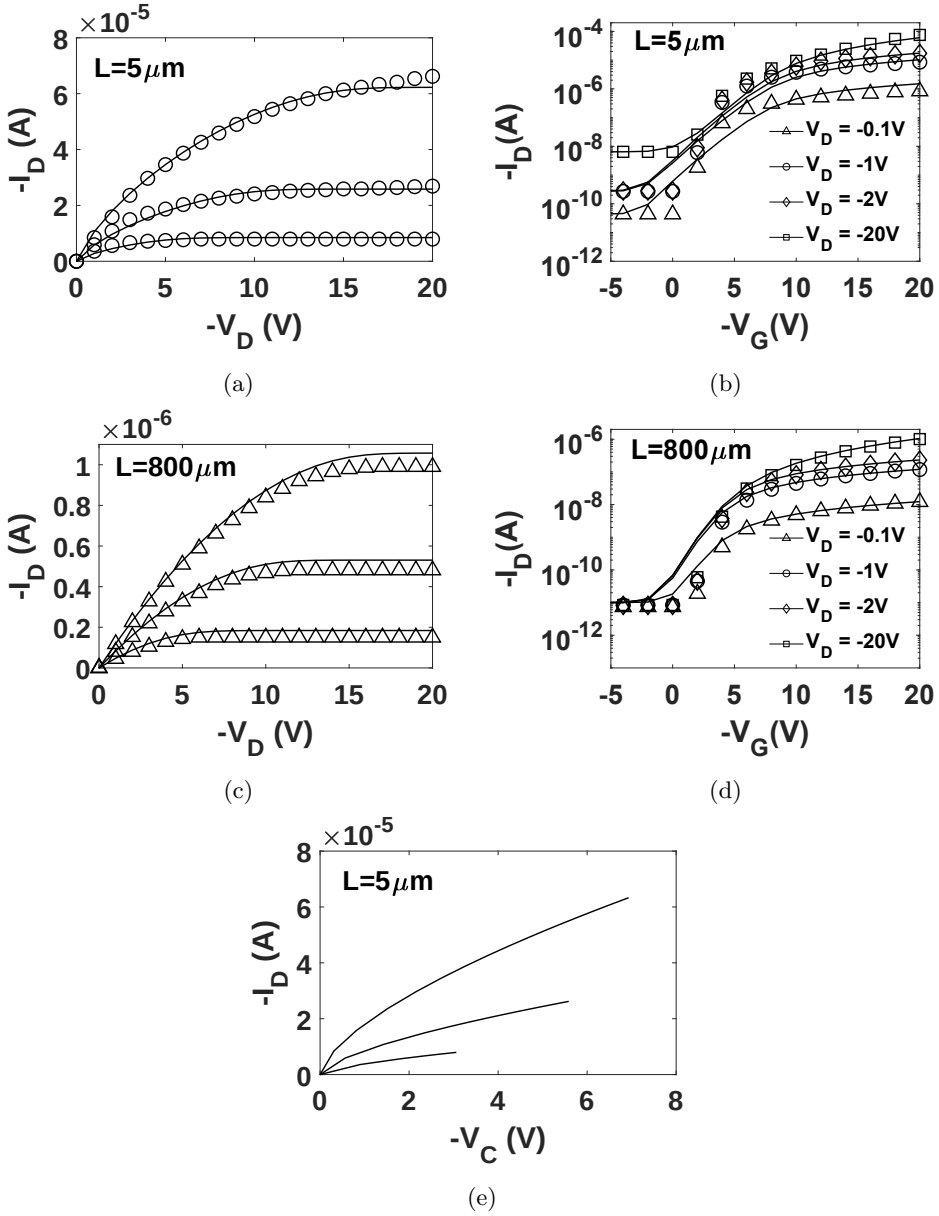

Figure 5.2: Experiment *B1-1*. (a), (c) Comparison of experimental $I_D - V_D$ curves measured at different values of V_G [143] (symbols) and our calculations with (5.1) and (5.10) (solid lines). (b), (d) Comparison of experimental $I_D - V_G$ curves measured at different values of V_D (symbols) and our calculations with (5.1) and (5.10) (solid lines). (e) $I_D - V_C$ curves extracted with (5.1) and (5.10) at different V_G. In (a),(c),(e), $V_G = -10, -15, -20$ V, from bottom to top.

5.3.3. Experiments C: Space-charge-limited contacts

The evolutionary parameter extraction procedure has been tested previously in single channel-length OTFTs in which the injection through the contact is space charge limited [92, 144]. Nevertheless,

Table 5.3: Values of parameters extracted in Experiments B (k_0 is in A/V$^{2+\gamma}$, V_T in V, V_{SS} in V, $M_C(V_G)$ in A/V^{m_k}, V_0 in V, V_N in V and I_0 in A).

	Experiment			
x	*B1-1*	*B2-1*	*B1-2*	*B2-2*
k_0	5.8×10^{-09}	5.8×10^{-09}	5.9×10^{-09}	5.7×10^{-09}
γ	3.5×10^{-10}	1.4×10^{-02}	3.8×10^{-03}	1.5×10^{-02}
V_T	$-2.8 \times 10^{+00}$	$-4.0 \times 10^{+00}$	$-3.6 \times 10^{+00}$	$-3.4 \times 10^{+00}$
V_{SS}	$-1.3 \times 10^{+00}$	$-2.0 \times 10^{+00}$	$-1.4 \times 10^{+00}$	$-1.3 \times 10^{+00}$
m_k	6.5×10^{-01}		7.1×10^{-01}	
$M_C(-10$ V)	3.8×10^{-06}		3.9×10^{-06}	
$M_C(-15$ V)	8.6×10^{-06}		8.3×10^{-06}	
$M_C(-20$ V)	1.8×10^{-05}		1.7×10^{-05}	
V_0		7.1×10^{-01}		9.9×10^{-01}
V_N		3.2×10^{-03}		9.9×10^{-01}
σ		4.1×10^{-01}		4.6×10^{-01}
$I_0(-10V)$		1.6×10^{-06}		1.7×10^{-06}
$I_0(-15V)$		3.1×10^{-06}		3.5×10^{-06}
$I_0(-20V)$		6.0×10^{-06}		6.4×10^{-06}

Table 5.4: Errors obtained after fitting the experimental output characteristics in Experiments B.

	NRMSE		Average
Sub-exp.	$L = 5\ \mu m$	$L = 800\ \mu m$	NRMSE
B1-1	5.1×10^{-02}	1.2×10^{-01}	8.5×10^{-02}
B2-1	5.4×10^{-02}	7.8×10^{-02}	6.6×10^{-02}
B1-2	5.6×10^{-02}	3.1×10^{-02}	4.4×10^{-02}
B2-2	6.2×10^{-02}	7.3×10^{-03}	3.5×10^{-02}

neither the fitting errors between experimental and calculated output characteristics of single-channel-length transistors have been compared with the errors obtained if multiple-channel-length transistors are analyzed; nor this kind of contacts has been assessed with a wider search space for the parameter m_k in (5.10), *i.e.* $0 \leq m_k \leq 2$. In this regard, the $I - V$ characteristics of multiple-length, bottom-gate, bottom-contact TFTs, with dinaphtho[2,3-b:20,30-f]thieno[3,2-b]thiophene (DNTT) as semiconductor, are studied. They were measured in [147] and are represented with symbols in Fig. 5.3. The Au contacts of the transistors were functionalized with pentafluorobenzenethiol (PFBT) to obtain a small contact resistance. All TFTs were fabricated on flexible plastic using aluminum oxide (Al_2O_3) as the gate dielectric (5.3 nm thick). The full protocols of the electrode deposition, substrate cleaning, and surface passivation are in [147, 159]. Short and long-channel TFTs were fabricated with a channel width of 200

Table 5.5: Values of parameters extracted in Experiments *C*.

	Experiment		
x	*C1-1*	*C1-2*	*C1-3*
k_0 [A/V$^{2+\gamma}$]	2.0×10^{-06}	2.2×10^{-06}	1.5×10^{-06}
γ	5.0×10^{-01}	6.6×10^{-02}	4.0×10^{-01}
V_T [V]	$-1.2 \times 10^{+00}$	$-1.1 \times 10^{+00}$	-9.3×10^{-01}
V_{SS} [V]	-6.7×10^{-01}	-2.9×10^{-01}	-1.2×10^{-01}
m_k	$1.6 \times 10^{+00}$	$1.3 \times 10^{+00}$	$1.4 \times 10^{+00}$
$M_C(-1.67$ V) [A/V^{m_k}]	2.0×10^{-04}	6.7×10^{-05}	8.6×10^{-05}
$M_C(-2.00$ V) [A/V^{m_k}]	3.7×10^{-04}	1.2×10^{-04}	2.0×10^{-04}
$M_C(-2.33$ V) [A/V^{m_k}]	3.7×10^{-04}	1.5×10^{-04}	2.5×10^{-04}
$M_C(-2.67$ V) [A/V^{m_k}]	2.7×10^{-04}	1.5×10^{-04}	2.4×10^{-04}
$M_C(-3.00$ V) [A/V^{m_k}]	1.8×10^{-04}	1.2×10^{-04}	1.5×10^{-04}

μm and lengths of 8, 40 and 80 μm.

The evolutionary procedure is used only with (5.1) and (5.10), since model (5.9) is no longer valid in these cases. Three experiments *C-1, C-2* and *C-3* are designed. Experiment *C-1* performs a single-transistor parameter extraction. It extracts the parameters of the transistor and the contact region from the output characteristics of the shortest transistor (circles in Fig. 5.3a). Then, it checks whether the output characteristics of the two longest transistors are reproduced with our calculations. Experiments *C-2* and *C-3* perform a multiple-transistor parameter extraction. Experiment *C-2* extracts the model parameters from the simultaneous analysis of the experimental data of the shortest and longest transistors (symbols in Figs. 5.3a and 5.3e, respectively). Then, it checks whether the output characteristics of the 40 μm length transistor (symbols in Fig. 5.3c) are reproduced with our calculations. Experiment *C-3* extracts the model parameters from the simultaneous analysis of the experimental data (symbols) of Figs. 5.3a, 5.3c and 5.3e.

The values of the parameters extracted with the three experiments are found in Table 5.5. Very small variations are observed among the experiments. The carrier mobility extracted with Experiment *C-1* is $\mu_0 = 2.9$ cm^2/Vs, and the threshold voltage is $V_T = -1.2$ V, in agreement with the respective values extracted with the TLM method in [147]: 3.2 cm^2/Vs and $V_T = -1.3$ V. The value $m_k > 1$ points out that the injection in these TFTs is space charge limited. The errors obtained when fitting the experimental and calculated output characteristics are in Table 5.6. The fitting error is slightly reduced when the amount of available data increases (from Experiment *C-1* to *C-3*). However, the improvement is not significant. As in the previous experiments, only the $I - V$ curves calculated with the single-transistor procedure (Experiment *C-1*) are represented in Fig. 5.3 (solid lines). As an additional test, this figure includes the comparison of experimental (symbols) and calculated (solid lines) transfer characteristics, also showing a very good agreement.

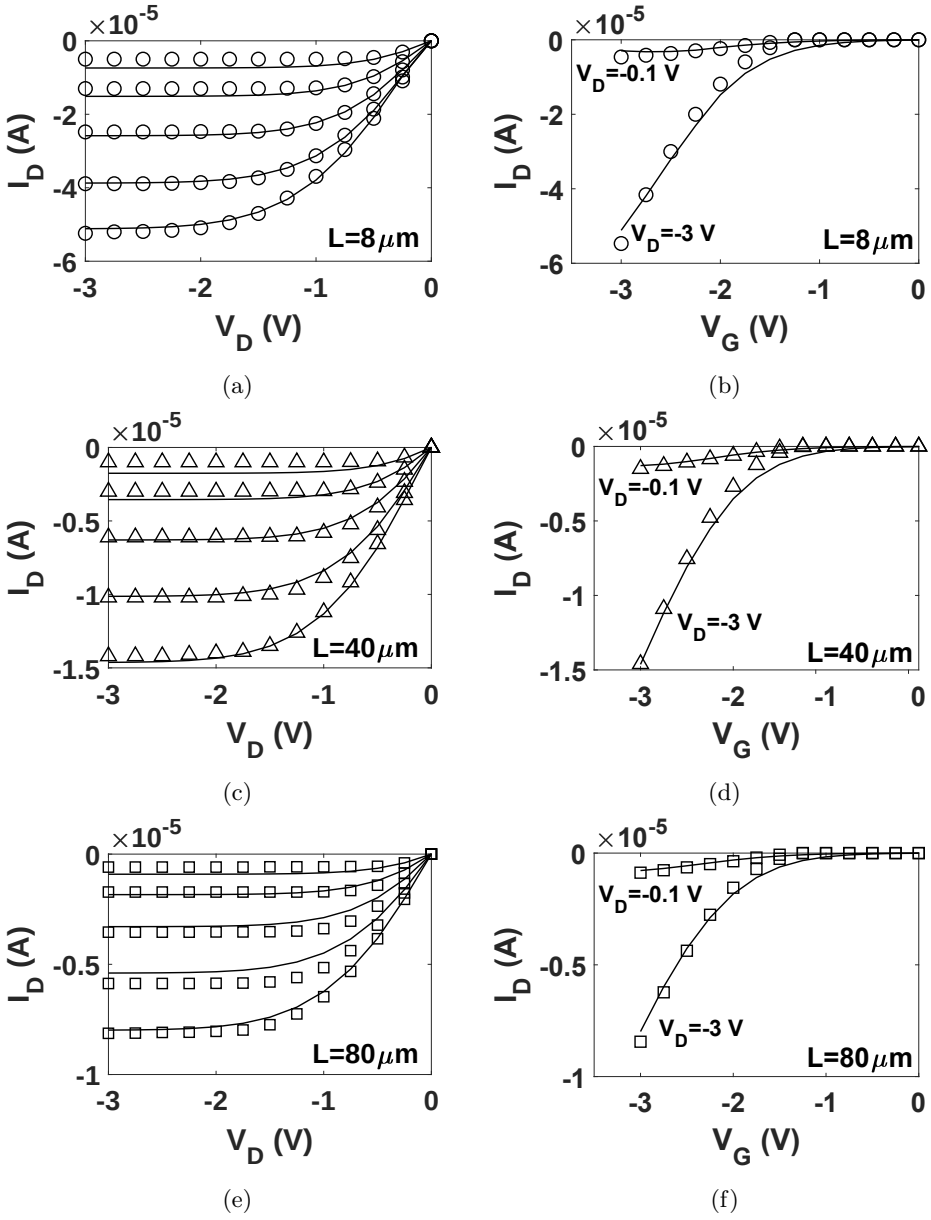

Figure 5.3: Experiment *C-1*. (a), (c), (e) Comparison of experimental $I_D - V_D$ curves measured at different values of V_G [147] (symbols) and our calculations with (5.1) and (5.10) (solid lines). V_G is swept from -1.67 (top) to -3 V (bottom) with a -0.33 V step. (b), (d), (f) Comparison of experimental $I_D - V_G$ curves measured at different values of V_D [147] (symbols) and our calculations with (5.1) and (5.10) (solid lines).

5.3.4. Experiment D: Application to an ammonia sensor

The standard contact model (5.10) takes on a special meaning in situations in which both the active channel and the contact region are affected by an external excitation, and both jointly determine the

Table 5.6: Errors obtained after fitting the experimental output characteristics in Experiments *C*.

	NRMSE			Average
Exp.	$L = 8\ \mu m$	$L = 40\ \mu m$	$L = 80\ \mu m$	NRMSE
C-1	7.8×10^{-02}	8.7×10^{-02}	1.2×10^{-01}	9.5×10^{-02}
C-2	3.4×10^{-02}	1.3×10^{-01}	5.8×10^{-02}	7.4×10^{-02}
C-3	5.3×10^{-02}	5.7×10^{-02}	7.6×10^{-02}	6.2×10^{-02}

electrical behavior of the device. In this sense, we apply the evolutionary procedure to an OTFT detector of ammonia (NH_3) gas [160]. In this publication, authors checked that the ammonia sensor deteriorated its electrical performance under the exposure of different concentrations of ammonia. Here, we check that the incorporation of a standard contact model (5.10) in the compact TFT model (5.1), not only enhances the precision in the determination of the intrinsic parameters of the transistor, but also provides information on how the contact region itself reacts to the ammonia gas. Our evolutionary procedure is applied to the output characteristics of a regioregular poly (3-hexylthiophene) (rr-P3HT) based OFET, which are represented with symbols in Figs. 5.4a (pristine device), 5.4c (gas exposure of 20 ppm) and 5.4e (gas exposure of 40 ppm) [160].

The full fabrication protocols of the rr-P3HT OTFT are detailed in [160]. Briefly, the bottom-gate bottom-contact OFET consists of a heavily doped p-type Si substrate, with a 300 nm thick film of thermally grown SiO_2 on top of it, acting as the gate structure. The capacitance per unit area of the gate dielectric layer is 10 nF/cm^2. The gold source-drain electrodes and the rr-P3HT polymer define a channel length and a width of 30 μm and 1 mm, respectively. Other information about the electrode deposition, substrate cleaning and surface passivation are found in [160].

Since the gas exposure changes the electrical performance of the device, the evolutionary procedure must treat independently each set of experimental $I_D - V_D$ curves (symbols in Figs. 5.4a, 5.4c and 5.4e). The values of the OTFT parameters, extracted in each of the three cases, are in Table 5.7. The $I_D - V_D$ curves calculated with (5.1) and (5.10) are depicted with solid lines in Figs. 5.4a, 5.4c and 5.4e, where a good agreement with the experimental data is shown. The $I_D - V_C$ curves extracted with our procedure for the respective three cases are depicted in Figs. 5.4b, 5.4d and 5.4f.

The exposure to gas ammonia changes the value of the carrier mobility and the threshold voltage of the transistor, as observed in [160]. However, the values of these parameters largely differ because, in our case, the contacts effects are considered during the extraction process. With our evolutionary procedure, V_T varies in the range 7.65 and -12.7 V, for the pristine OTFT and for the 40 ppm gas exposure case, respectively; while the values of μ_0 are 2.9×10^{-4}, 8.2×10^{-5} and 6.3×10^{-5} for the pristine OTFT and under a exposure of 20 and 40 ppm, respectively.

The main contribution of this analysis is the evolution of the current-voltage curves at the contact when the concentration of ammonia gas increases. Fig. 5.4b shows the $I_D - V_C$ curves extracted for the pristine OTFT at different values of V_G. The curves are concave following (5.10) with $m_k = 1.21$. Figs. 5.4d and 5.4f show the $I_D - V_C$ curves extracted for the exposed OTFT under ammonia gas at

Table 5.7: Values of parameters extracted in Experiments D.

	Ammonia Concentration (ppm)		
x	0	20	40
k_0 [A/V$^{2+\gamma}$]	2.9×10^{-12}	8.2×10^{-13}	6.3×10^{-13}
γ	2.9×10^{-01}	8.3×10^{-01}	1.1×10^{-00}
V_T [V]	$3.0 \times 10^{+01}$	$7.7 \times 10^{+00}$	$-1.3 \times 10^{+01}$
V_{SS} [V]	$-1.5 \times 10^{+01}$	$-3.2 \times 10^{+01}$	$-3.1 \times 10^{+01}$
m_k	$1.2 \times 10^{+00}$	6.9×10^{-01}	5.7×10^{-01}
$M_C(-10$ V) [A/V^{m_k}]	1.8×10^{-07}	5.4×10^{-08}	2.7×10^{-08}
$M_C(-20$ V) [A/V^{m_k}]	4.5×10^{-08}	5.3×10^{-08}	4.2×10^{-08}
$M_C(-30$ V) [A/V^{m_k}]	2.4×10^{-08}	5.0×10^{-08}	5.1×10^{-08}
$M_C(-40$ V) [A/V^{m_k}]	1.7×10^{-08}	5.5×10^{-08}	4.7×10^{-08}

different values of V_G. These two sets of curves become convex, also following (5.10) but with $m_k < 1$ ($m_k = 0.69$ and $m_k = 0.57$ for gas concentrations of 20 and 40 ppm, respectively). A clear deterioration of the contact region is observed when the ammonia concentration is increased. This can be attributed to chemical changes at the metal-organic interface that alter the energy barrier that charge carriers must overcome. These changes drastically modify the contact region from a space-charge to a Schottky-barrier limited contact.

5.4. Conclusion

We have proposed a versatile analytical expression that can reproduce the current-voltage curves at the contacts of OTFTs. The expression is controlled exclusively with two parameters. One of them depends on the gate voltage. The other one allows to distinguish between space-charge or Schottky-barrier limited contacts. The contact model has a direct physical justification when space-charge limited contacts are treated. In the case of Schottky-barrier limited contacts, our model is empirical, although it has been successfully compared with other semi-empirical models based on the current transport theory in metal semiconductor barriers.

The contact model is introduced in a generic compact model that describes the current-voltage characteristics of OTFTs. The contact model used in combination with an evolutionary parameter extraction method allows to extract the parameters of short channel OTFTs. We have checked that our procedure obtains similar results to those methods in which multiple transistors with different lengths are necessary in order to characterize the effects of the contact region.

The procedure has been also applied to an ammonia gas sensor in order to determine the effect of the gas, not only in the internal parameters of the transistor, carrier mobility or threshold voltage, but also in the contact region. We have detected that the gas can modify the energy barrier at the contact in such a way that a space-charge limited contact is transformed into a Schottky-limited contact when

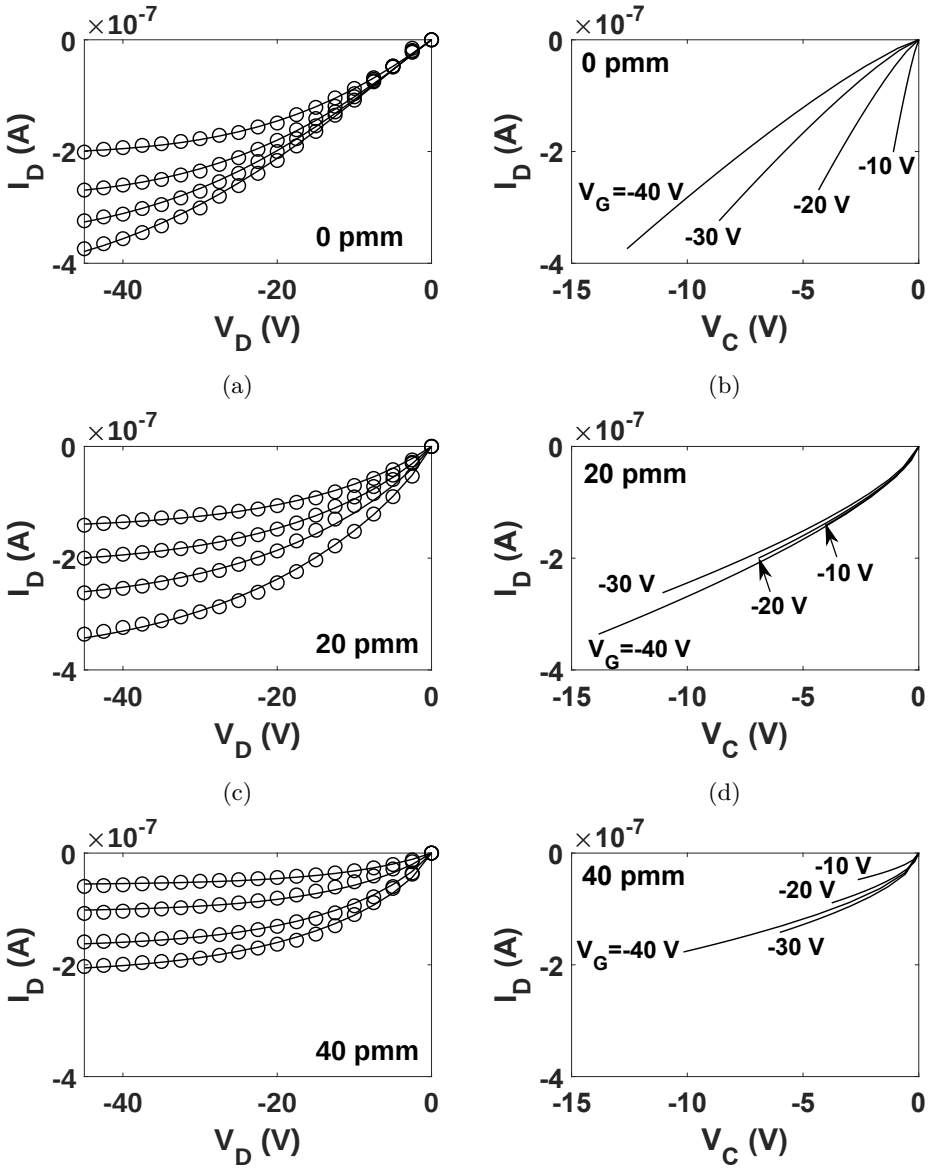

Figure 5.4: Experiment D. (a), (c), (e) Comparison of experimental $I_D - V_D$ curves (symbols) and our calculations with (5.1) and (5.10) (solid lines) at three concentrations of ammonia and different V_G values. V_G is swept from -10 (top) to -40 V (bottom) with a -10 V step. (b), (d), (f) $I_D - V_C$ curves calculated with (5.10) at different V_G values.

ammonia gas is present.

6

Conclusions and future work

6.1. Conclusions

1. An evolutionary parameter extraction procedure has been developed to simultaneously determine the parameters of both a compact model for the current-voltage characteristics of organic thin-film transistors and a contact model. This procedure overcomes shortcomings of previous parameter extraction procedures, for example, in those situations whereby the parameter set extracted by other procedures does not comply its physical meaning, or if a poor agreement between the experimental data and the analytical results exists. In the last case, the evolutionary procedure can be used as a problem optimization method. The evolutionary parameter extraction procedure has been applied to experimental output characteristics measured in different transistors, the results calculated with the model show an excellent agreement with the experimental data.

2. In order to ensure the physical meaning of each parameter of the model, the evolutionary procedure has been extended with additional rules in form of optimization objectives and constrains. These changes has given rise to a Many-Objective Problem (MaOP). Additional sets of experimental data have been used to test these modifications, also obtaining excellent results.

3. A modification of the contact model has been proposed in order to extend its applicability to organic phototransistors. The model for the contact region of these devices incorporates the effects of illumination. This model is valid for all the operation regimes of the transistors. Once again, the compact model and the contact region model are validated with published experimental data from several OPTs under different illumination conditions. The results show that both photoconductive and photovoltaic effects impact the intrinsic region of the transistor, as well as the electrical behavior of the contact region. The parameters used in the contact region model are linked to these photovoltaic and photoconductive effects.

4. A final modification of the contact model has been proposed in order to describe the current-voltage characteristics of different kinds of contacts. In this sense, a standard model for the contact region of OTFTs has been proposed and integrated into the generic compact model for the current voltage characteristics of OTFTs. It is a versatile model that reproduces the behavior of Schottky-barrier or space-charge-limited contacts. It is a simple unified model since only the value of a single parameter is necessary in order to distinguish between both kinds of contacts. The model has been tested with published experimental data of OTFTs with Schottky-barrier or space-charge limited contacts. In particular, we have detected how the contact region of an ammonia sensor is very sensitive to the concentration of gas, in such a way that a space-charge-limited contact is transformed into a Schottky-barrier contact when the gas concentration increases.

6.2. Future Work

Regarding our evolutionary procedure, suggestions for future work are presented in this section. As seen in Chapter 3, the consideration of new requirements made us increase the number of objectives (n_{obj}) from 2 (as originally defined in Chapter 2) to 4. In doing so, our evolutionary procedure had

to solve a MaOP instead of a MOP. Since OTFT compact models are in continuous evolution, new requirements and objectives can be added to the evolutionary procedure. This would add complexity to the evolutionary procedure, and therefore, to the parameter extraction process. For this purpose, in the next section some limitations, and possible solutions, of MaOPs are presented. In case that the evolutionary procedure has any problem dealing with the defined MaOP, the decision maker (DM) or expert will be in charge of choosing the best approach following its expert criteria.

Difficulties to Solve MaOPs

As mentioned in Chapter 3, optimization problems with four or more competing objectives are referred to as many-objective problems (MaOPs) [161]. The main difficulties associated with MaOPs are: (i) high computational cost, (ii) poor scalability of most existing MOEAs, (iii) difficulty in the visualization of a Pareto-optimal front (POF) for problems with more than three objectives [162–164]. These facts make evolutionary many-objective optimization one of the most challenging research areas in the field of evolutionary optimization and explains the growing research emphasis in this direction [163].

(i) The computational cost is difficult to attenuate, unless there are redundant objectives. In this case, they should be removed from the objective set.

(ii) MOEAs have proven their effectiveness and efficiency in solving problems with two or three objectives. However, recent studies show that MOEAs face many difficulties when tackling problems involving a larger number of objectives which deteriorates the search ability of the traditional MOEAs [165, 166]. The most common situation is observed when most individuals are non-dominated with respect to each other. These individuals are the so-called dominance resistant solutions (DRSs) or outliers [164, 167–169]. DRSs are solutions with a poor value in at least one of the objectives, but with near optimal values in the others. In other words, those are non-dominated solutions, but far from the POF.

(iii) Due to the curse of dimensionality, the number of points required to represent accurately a Pareto front increases exponentially with the number of objectives. Formally, the number of points necessary to represent a Pareto front with k objectives and resolution r is bounded by $O(kr^{k-1})$. In addition to the previous problem, clearly, with more than three objectives it is not possible to plot the Pareto front as usual. Due to this fact, different alternatives must be found.

Despite NSGA-II is considered a traditional MOEA, it was used successfully in Chapters 3 and 4 to solve a MaOP with 4 objectives, achieving in both cases high quality results. For this reason, and also for the sake of simplicity, it was subsequently decided that NSGA-II would be the search tool of our evolutionary procedure. It is clear that under certain circumstances (considering 4 or more objectives) it could easily happen that the evolutionary procedure does not converge to a solution as (ii) states. This would mean the failure of the evolutionary procedure, which can not be tolerated.

Since the convergence to an optimum solution is the highest priority, and the visualization is crucial for the decision-making process, some proposals to deal with the previously presented problems are introduced below.

Many-objective evolutionary algorithms

Due to the continued increase of n_{obj}, traditional MOEAs such as NSGA-II do not operate optimally. Actually, traditional MOEAs were reformulated to optimally deal with MaOPs [170]. In addition to these new versions, great advances have been made in the last decade in the development of Many-objective evolutionary algorithms (MaOEAs) [100, 171, 172]. These MaOEAs use special mechanisms to manage MaOPs and preserve diversity among the different objectives. For instance, the NSGA-III was proposed as an improvement of the NSGA-II [171, 172]. The main difference of NSGA-III with its predecessor is that NSGA-III uses a set of reference points to maintain the diversity of the Pareto points during the search. Another example of MaOEA is the MOEA/D, which decomposes a MOP into a number of scalar optimization sub-problems and optimizes them simultaneously [100]. Despite MaOEAs are developed especially to work with MaOPs, they also have limitations. Thus, the following proposals must also be considered.

Preference-ordering approaches

These approaches assume that no objective in the given problem is redundant and aim to counter the low selection pressure for convergence by inducing a preference ordering over the non-dominated solutions [164]. Some of these preference approaches are the average ranking (AR) [173], the maximum ranking (MR) [173], the favor preference relations [174], or the proposals found in [164]. The AR relation computes a different rank for each solution, considering each objective independently. The final rank is obtained by summing up the ranks on each objective. In turn, the MR relation takes the best rank as the global rank. In favor relation, the favored vector is that which outperforms the other one in more objectives.

Objective reduction approaches

These approaches [175–178] assume the existence of redundant objectives in a given problem with n_{obj} competing objectives. Operating on the objective vectors of the non-dominated solutions obtained from a MOEA, these approaches aim to identify a smallest set of n ($n \leq n_{obj}$) conflicting objectives which: (a) generates the same POF as the original problem, or (b) alternatively, preserves the dominance relations of the original problem. Such n objectives are termed essential, and the remaining ones are called redundant. If $n \leq 3$, an otherwise unsolvable problem will become solvable. Even if $4 \leq m \leq n_{obj}$, objective reduction will contribute to higher search efficiency, lower computational cost and ease in visualization and decision-making.

Constraints

There may be situations in which some of the n_{obj} objectives are always accomplished by the whole population. In these cases, instead of carrying out a hard objective reduction, some of the objectives can be reformulated as constraints [179]. By doing this, all the information about the problem is kept during the whole search process.

Goals and priorities

Goal and priority data are naturally available from the problem formulation. In order to differentiate among individuals in a MaOP, goals and priorities should be assigned to each of its n_{obj} [180]. In so doing, DRSs could be removed from the Pareto front and the search could be directed to more promising areas. In addition, better decisions and elections of solutions could be performed, since goals and priorities are used as a form of fitness values. It is clear that goals and priorities must be assigned by the DM, who has a full understanding of the problem.

Pareto front visualization

As mentioned previously, the increment of $n_{obj} \geq 3$ means that the Pareto front can not be plotted as usual. This is a major problem since visualization plays a key role in a proper decision-making process [181, 182]. Thus, different alternatives must be explored. Parallel coordinates [183] and self-organizing maps [184] are some of the methods proposed to ease decision making in high dimensional problems. Despite the progress achieved, Pareto front visualization is a hot topic in the many-objective optimization context, and more research is still required.

Finally, it must be emphasized once again, that the expert or DM is in charge of selecting the most appropriate remedy to any particular problem. There may be cases in which the exposed proposals can be combined, which in turn can help the DM to better address the presented problem/s.

7

Resumen en español/Spanish summary

7.1. Motivación

Los transistores orgánicos de lámina delgada (OTFTs) han despertado un considerable interés en la Electrónica debido a las ventajas asociadas con los materiales orgánicos/poliméricos utilizados, como la flexibilidad, los bajos costos de fabricación y el peso, y sus posibles aplicaciones en dispositivos electrónicos flexibles de gran superficie, como pantallas y sensores [1]. Sin embargo, estos materiales también tienen limitaciones importantes, por ejemplo, una baja movilidad electrónica en comparación con semiconductores cristalinos inorgánicos, alta variabilidad del proceso, o deterioro por efecto de los contactos. En particular, los efectos de los contactos se han estudiado ampliamente con el objeto de incorporarlos en los modelos compactos de los transistores [2–4].

Los modelos compactos son modelos analíticos que pueden reproducir el comportamiento eléctrico de un dispositivo determinado en todas las regiones de operación. Por lo general, se basan en principios físicos, con algunos parámetros libres que se utilizan para asegurar una transición continua entre regiones o para mejorar la simplificación matemática necesaria de la física del dispositivo. Por lo tanto, estos modelos deben estar asociados con métodos para extraer sus respectivos parámetros, usando como base las características eléctricas del transistor deseado [3–5]. Los parámetros extraídos deben de tener un valor físico correcto, ya que un valor no válido causaría la invalidación de dicho resultado, significando esto un fallo en la búsqueda del conjunto de parámetros. Finalmente, el conjunto de parámetros extraídos debe proporcionar un buen acuerdo entre el modelo y los datos experimentales usados para la extracción.

7.2. Objetivos y Metodología

Esta tesis se centra en la definición de un procedimiento para extraer los parámetros de un modelo compacto para OTFTs, que incluye efectos de los contactos, a partir de las curvas de salida del dispositivo. La principal característica de este procedimiento es que garantiza la determinación del valor del conjunto de parámetros del modelo, resolviendo así algunas de las limitaciones presentadas en procedimientos encontrados en la bibliografía. Para este propósito, se presentan una serie de objetivos que tendrán que cumplirse en el orden dado:

1. Describir una metodología eficiente para la extracción de parámetros de diferentes tipos de OTFTs, utilizando como base un modelo compacto para OTFTs que incluya los efectos en los contactos y un algoritmo evolutivo multi-objetivo (MOEA).

2. Validar el conjunto de parámetros extraídos con leyes físicas y eléctricas que describen el comportamiento del dispositivo empleado. La validación del conjunto de parámetros supondrá la validación del procedimiento evolutivo y del modelo compacto, ya que ambos son utilizados para realizar la extracción del conjunto de parámetros.

3. Dotar al procedimiento evolutivo de conocimiento experto. Con esto se persigue que el proceso de búsqueda del procedimiento evolutivo pueda explorar áreas más prometedoras, en las cuales cabe la posibilidad de encontrar conjuntos de parámetros más precisos.

4. Ampliar la funcionalidad del modelo compacto utilizado por el procedimiento evolutivo, y por lo tanto, el alcance del procedimiento evolutivo. El propósito de este objetivo es estandarizar el procedimiento evolutivo, con la finalidad de abarcar la mayor cantidad de fenómenos físicos y dispositivos posibles.

Para llevar a cabo el desarrollo de esta tesis es necesario tener en cuenta las bases de funcionamiento de los OTFTs. Además, también se deben considerar aquellos efectos que degradan el rendimiento de los dispositivos, haciendo hincapié en los efectos de contacto.

7.3. Conceptos generales usados en la tesis

7.3.1. Materiales Orgánicos

Los materiales orgánicos utilizados en dispositivos orgánicos se pueden clasificar en polímeros, moléculas pequeñas, semiconductores orgánicos dopados, complejos de transferencia de carga y compuestos orgánicos semiconductores/aislantes [6].

Los polímeros semiconductores se emplean en conexiones y contactos de dispositivos orgánicos, debido a su idoneidad para ser imprimidos. Sus principales características son: no requieren el uso de disolventes halogenados, los cuales presentan problemas ambientales y regulatorios; son menos susceptibles a problemas de adhesión, sus perfiles de solubilidad permiten el acceso a valores de viscosidad mayores que 200 mPa.s y proporcionan una uniformidad significativamente mayor de dispositivo a dispositivo [7, 8].

Transistores, diodos, sensores [9], transductores y elementos de memoria pueden incorporar semiconductores en forma de sólidos moleculares y/o polímeros semiconductores orgánicos. Las aplicaciones de estos dispositivos se pueden encontrar en circuitos de complejidad moderada, como controladores de pantallas [10], etiquetas de identificación por radio frecuencia (RFID) [11], o sensores de presión.

El orbital molecular desocupado de menor energía (LUMO) de la mayoría de los compuestos orgánicos se encuentra fuera de rango para el transporte de electrones. Esta es la razón por la que hay menos estructuras que se han identificado como semiconductores tipo n en comparación con el número de semiconductores tipo p. La cantidad de huecos en un semiconductor viene determinada principalmente por la posición relativa del orbital molecular ocupado de mayor energía (HOMO) con respecto al nivel de Fermi del contacto (función trabajo).

El cierto retraso tecnológico de los transistores de canal n afectó directamente al desarrollo de la tecnología complementaria. Recientemente, se ha logrado un progreso significativo en el desarrollo de semiconductores orgánicos, estando disponibles materiales de tipo p y n que presentan un alto rendimiento y una buena estabilidad en aire [12, 13]. En los circuitos complementarios, se utilizan voltajes de puerta positivos y negativos para conmutar los transistores, y además se caracterizan por tener una mejor velocidad y confiabilidad en comparación con sus homólogos unipolares [14, 15]. Actualmente, hay disponibles circuitos complementarios orgánicos fabricados con materiales solubles [13, 14, 16, 17], pero aún no existe una tecnología complementaria totalmente imprimida sobre substrato flexible con una alta movilidad electrónica para semiconductores de tipo p y n [11].

7.3.2. Transistores Orgánicos de Efecto Campo

Un transistor orgánico de efecto campo (OFET) es un dispositivo electrónico cuyo funcionamiento gira en torno a una estructura metal-aislante-semiconductor. Está formado por una puerta metálica, un dieléctrico, y capas de semiconductores. Dos contactos de metal, fuente y drenador. Si el semiconductor usado está en forma de película delgada, los dispositivos se denominan transistores orgánicos de película delgada (OTFTs). La posición de los electrodos de drenador y fuente en la parte superior de la estructura o incrustados entre el semiconductor y el aislante definen dos configuraciones típicas de transistores: el transistor de contactos superiores o el transistor de contactos inferiores, respectivamente. Esta estructuras se basan en las desarrolladas inicialmente para los transistores de silicio amorfo. El electrodo de puerta también se utiliza como substrato, proporcionando un soporte a toda la estructura. El óxido aislante o los polímeros aislantes recubren la puerta metálica con o sin tratamiento de superficie. Si no se aplica una tensión a la puerta V_G, la conductividad intrínseca del semiconductor orgánico es baja; si se aplica una tensión V_D entre drenador y puerta, fluirá muy poca corriente a través de la película semiconductora. Se dice que el dispositivo está en el estado OFF. Cuando una tensión V_G se aplica a la puerta, el campo eléctrico que existe a través de la estructura MOS atrae cargas hacia la interfaz dieléctrico-semiconductor. Estas cargas acumuladas son en su mayoría móviles y dan lugar a un canal conductor entre la fuente y el drenador. Estas cargas móviles pueden moverse en respuesta a la tensión V_D aplicada. El transistor está funcionando en el modo ON o acumulación.

El canal conductor aparece cuando se alcanza o sobrepasa un valor umbral, V_T. El valor de esta tensión umbral depende de diferentes mecanismos internos de la estructura. La mayoría de los semiconductores orgánicos no están dopados intencionadamente por lo que las cargas existentes son inyectadas y extraídas a través de los electrodos. En la mayoría de los casos, hay un desajuste entre el nivel de Fermi de los electrodos y el HOMO (LUMO) de los semiconductores tipo p (tipo n), que da lugar a la existencia de barreras de inyección de carga. Es necesaria la aplicación de una tensión V_G no nula a la puerta para desplazar los niveles orbitales de los semiconductores hacia arriba o hacia debajo de manera que los orbitales moleculares entren en resonancia con el nivel de Fermi del electrodo y se reduzcan las barreras de inyección de carga. Por otro lado, siempre hay estados asociados a trampas, impurezas y defectos en la película semiconductora, así como las moléculas de H_2O y O_2 adsorbidas del ambiente. Es necesario aplicar una tensión V_G no nula a la puerta para llenar estos estados trampa antes de que las cargas móviles pueden ser transportadas a lo largo del canal de conducción. El umbral de tensión V_T incorpora todos estos efectos.

Las curvas corriente-tensión experimentales de un OFET son muy similares a las de los MOSFETs. Esta es la razón por la que en muchas ocasiones los OFETs se describan mediante las ecuaciones clásicas del transistor MOS:

$$\begin{aligned} I_D &= \frac{W\mu_0 C_i}{L}\left[(V_G - V_T)V_D - \frac{V_D^2}{2}\right],\ V_D < V_G - V_T \\ I_D &= \frac{W\mu_0 C_i}{2L}\left[(V_G - V_T)^2\right],\ V_D \leq V_{GS} - V_T \end{aligned} \tag{7.1}$$

donde C_i es la capacidad del aislante de puerta por unidad de área, μ_0 es la movilidad de los portadores

y W y L son la anchura y la longitud del canal, respectivamente.

Hay algunos aspectos que necesitan de una especial consideración y hacen que los OFETs se distancien del comportamiento descrito por el modelo ideal MOS (7.1): la inyección de carga de los contactos, el transporte de carga en el semiconductor orgánico y las inestabilidades creadas por la acumulación de carga en la estructura. Debido a ellos, entre otros factores, el modelo (7.1) no es capaz de reproducir las características $I - V$ de los OFET, siendo obligatorio para tal fin el uso de modelos específicos.

7.3.3. Efectos de los contactos

Comprender y reducir los efectos de los contactos es de gran importancia tecnológica, ya que limitan el rendimiento de los OTFTs [18]. Hay evidencias experimentales que demuestran la existencia de estas regiones. La primera es evidente, debido a la propia naturaleza de los diferentes materiales que constituyen los contactos. Podemos encontrar una segunda razón en microfotografías de la interfaz. En ellas se muestra cómo la densidad de las moléculas en el material orgánico no son del mismo tamaño cerca del contacto metalúrgico o lejos del mismo. Una tercera razón se encuentra en medidas de perfil de potencial a lo largo del canal del transistor. Estas medidas muestran una caída de tensión en el contacto de fuente mayor que la que se produce cerca del drenador. En esta situación, se puede despreciar la caída de tensión entre el drenador y el canal intrínseco.

Se han realizado grandes esfuerzos para reducir el impacto de los efectos de contacto y, por lo tanto, para mejorar el rendimiento de los dispositivos. Entre los intentos por reducir los efectos de los contactos se puede destacar el uso de nuevos materiales para los electrodos de contacto, la inserción de capas en la interfaz metal-semiconductor o el uso de dopaje molecular. Además, se han desarrollado modelos capaces de reproducir los efectos de contacto en OTFTs [4, 19], siendo este actualmente un tema de interés [20].

7.3.4. Algoritmos Evolutivos

Los algoritmos evolutivos (EAs) son heurísticas de búsqueda y optimización basadas en la evolución natural y genética [21, 22]. El concepto de evolución natural ayudará al lector a tener una idea inicial de cómo funcionan los EAs. En la naturaleza, existen entidades o poblaciones de individuos con capacidad de reproducción. Estos individuos suelen tener diferentes características, como la altura o la fuerza. Los individuos descendientes heredan algunas características de sus progenitores. Además, algunos de ellos pueden mutar adquiriendo nuevas cualidades. A medida que pasa el tiempo, solo los individuos capaces de adaptarse al entorno sobreviven, generalmente los más aptos. Tomando como referencia la evolución natural, los EAs procesan en cada iteración una población de soluciones potenciales (individuos) para un problema determinado (entorno). Durante la ejecución del EA, las soluciones potenciales se combinan (reproducción) y algunas de ellas se alteran (mutación), dando lugar a una población de descendientes, en la que las soluciones potenciales más aptas tienen la mayor probabilidad de permanecer en ella (adaptación al entorno).

La diferencia más importante entre las técnicas de optimización clásicas y los EAs es que estos últimos procesan una población de soluciones potenciales en cada iteración en lugar de una única solución

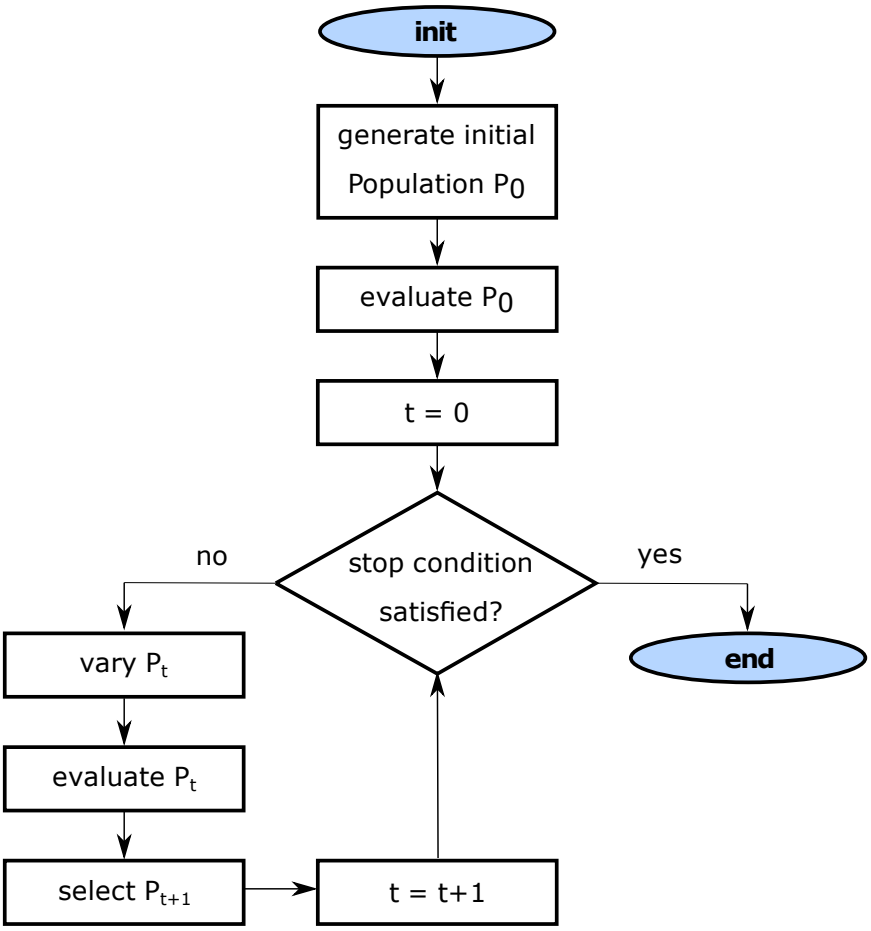

Figure 7.1: Diagrama de flujo básico de un EA.

para el problema. La Figura 7.1 muestra el diagrama de flujo básico de una EA, donde P_t es la población en la iteración t y N es el tamaño de la población. Los individuos de la población son soluciones potenciales de una función de minimización (maximización) $f(x)$. Se denominan $x^{(i,t)} = ({x_1}^{(i,t)}, \ldots, {x_p}^{(i,t)})$, $i = 1, 2, \ldots, N$ y $x^{(i,t)} \in X^p \subseteq \mathbb{R}^p$, donde X^p es el dominio de la población.

Tres operadores principales guían la evolución de la población:

- *Operador de recombinación.* Es el principal responsable de que la población mejore. Este operador combina las características de los progenitores para crear nuevos individuos, llamados descendientes. La idea de la recombinación es descubrir mejores individuos que los originales, o individuos intermedios que en el futuro permitirían descubrir mejores.

- *Operador de mutaciones.* Este operador contribuye a la diversidad de la población. La recombinación de los progenitores por sí sola puede no mejorar la población o puede no descubrir nuevos individuos. En estos casos, algunos de los descendientes deben ser alterados por otros medios. El

operador de mutación es responsable de garantizar que se explore todo el espacio de búsqueda. Este operador también es utilizado por los EAs para evitar la convergencia a óptimos locales.

- *Operador de selección.* Basado en una medida de la adecuación de los individuos, este operador decide qué individuos formarán parte de la población de la próxima generación.

Los EA son algoritmos altamente parametrizados, siendo sus características más importantes introducidas a continuación.

7.3.4.1. Representación de los Individuos

El primer paso para definir un EA es vincular el contexto del problema original y el espacio de solución donde tiene lugar la evolución. Tiene que estar claro que tipo de soluciones tiene el problema original. Luego, se define el dominio más apropiado para dichas soluciones y, finalmente, se utiliza la representación más apropiada.

7.3.4.2. Población Inicial

Al comienzo de un EA, la población está vacía. Para completarla con individuos, se debe definir un método para generar la población inicial P_0. No existe un método estándar para inicializar la población de un EA y generalmente P_0 se genera aleatoriamente. Una población obtenida en otras ejecuciones o una obtenida mediante otra heurística podría usarse como P_0.

7.3.4.3. Operadores de Variación

Los operadores de recombinación y mutación se definen con las tasas de recombinación (P_c) y mutación (P_m), respectivamente. Mediante el uso de los valores correctos de P_c y P_m, se debe explorar el espacio de búsqueda completo. Un P_c bajo no permitirá explorar el espacio de búsqueda, mientras que un P_m alto evitará la convergencia del EA.

7.3.4.4. Función de Evaluación

La función de evaluación muestra las diferencias en calidad entre los individuos de la población. Da una puntuación a cada individuo de la población. Dada una función de minimización (o maximización), un individuo x^q obtendrá una puntuación más baja (o mayor) que otro x^j si x^q es mejor.

7.3.4.5. Operador de Selección

El operador de selección selecciona los individuos más aptos o mejor puntuados, los cuales pasaran a formar parte de la población de la próxima generación P_{t+1}. Además, P_{t+1} debe cumplir ciertos requisitos, como la diversidad y el elitismo.

Diversidad La diversidad de la población es un factor crucial en problemas de optimización complejos, y la extracción de parámetros es uno de ellos. Si todos los individuos de la población estuvieran ubicados en el mismo espacio, por ejemplo, si P_{t+1} estuviese compuesta solamente por los individuos más aptos, el procedimiento podría converger prematuramente a un óptimo local. Por otro lado, si P_{t+1} está compuesta por individuos muy poco aptos, no convergería en absoluto. El operador de selección controla el compromiso entre la calidad y la diversidad de la población para garantizar una convergencia adecuada. A los individuos más aptos se les da una mayor probabilidad de participar en P_{t+1} que a los peores individuos. Sin embargo, los individuos de baja calidad también tienen la posibilidad de estar en P_{t+1}.

Elitismo Dado que los EAs son estocásticos, el mejor individuo encontrado hasta el momento, x^{best}, podría perderse durante el proceso de evolución. Los EAs introducen elitismo para garantizar la presencia de x^{best} en P_{t+1}. Durante el proceso de evolución y al final de cada ejecución, x^{best} siempre estará disponible.

7.3.4.6. Condición de Parada

Otro parámetro crítico en la definición de un EA es decidir cuándo detenerlo. Para tal efecto, se suelen usar los siguientes criterios:

- *Solución óptima global lograda.* En este caso, no tiene sentido seguir buscando una mejor solución.
- *Coste de la CPU.* Para minimizar el tiempo de cómputo, la ejecución del EA puede restringirse a un número limitado de generaciones y evaluaciones de la función de evaluación.
- *Estancamiento de la búsqueda.* La ejecución del EA se puede detener después de un número limitado de generaciones si no hay mejoría en la población. En este caso, la población debería de ser reiniciada, pero manteniendo x^{best}.

7.3.5. Problemas Multi-Objetivo

En la mayoría de los casos prácticos, los problemas tienen varios requisitos que cumplir. El proceso de extracción de parámetros es solo uno de ellos. Los problemas de este tipo se conocen como problemas multi-objetivo (MOPs) [23]. La mayor diferencia entre los problemas con un solo objetivo y los MOPs es la disposición de un conjunto de soluciones potenciales. En un problema con n_{obj} compitiendo entre ellos, cada uno de ellos se mide por una función objetivo $f_i(i = 1, \ldots, n_{obj})$. Podemos definir una función objetivo global f que cumpla con las siguientes relaciones para dos soluciones potenciales para el problema s_1 y s_2

$$\begin{aligned} &f(s_1) = f(s_2) \Leftrightarrow f_i(s_1) = f_i(s_2)\ \forall i \in 1, 2, ..., n_{obj} \\ &f(s_1) \leq f(s_2) \Leftrightarrow f_i(s_1) \leq f_i(s_2)\ \forall i \in 1, 2, ..., n_{obj} \\ &f(s_1) < f(s_2) \Leftrightarrow f(s_1) \leq f(s_2) \wedge f(s_1) \neq f(s_2) \end{aligned} \tag{7.2}$$

Teniendo en cuenta las relaciones anteriores, el criterio de dominancia de Pareto se puede utilizar para establecer un orden entre los individuos de la población [24]:

$$\begin{aligned} &s_1 \prec s_2 \Leftrightarrow f(s_1) < f(s_2) \\ &s_1 \preceq s_2 \Leftrightarrow f(s_1) \leq f(s_2) \\ &s_1 \sim s_2 \Leftrightarrow f(s_1) \not\leq f(s_2) \wedge f(s_2) \not\leq f(s_1) \end{aligned} \tag{7.3}$$

donde $s_1 \prec s_2$ (s_1 domina s_2) significa que s_1 es una solución mejor que s_2, $s_1 \preceq s_2$ (s_1 domina débilmente s_2) significa que s_1 es una solución mejor o igual que s_2, y $s_1 \sim s_2$ (s_1 es indiferente a s_2) significa que ambas soluciones no son comparables. Una solución Pareto-óptima s_{opt} [24] se define como una solución que no puede ser dominada por ninguna otra solución en el conjunto de soluciones S:

$$\nexists s_i \in S : s_i \prec s_{\text{opt}} \tag{7.4}$$

Todas las soluciones óptimas de Pareto componen el frente de Pareto. Las soluciones del frente de Pareto son indiferentes entre sí e igualmente válidas. Por lo tanto, serán los usuarios finales o los expertos quien decidan que soluciones del frente de Pareto son las mejores.

7.3.6. Algoritmos Evolutivos Multi-Objetivo

El uso combinado de EAs y el criterio de dominancia de Pareto da lugar a un tipo especial de EAs, denominados algoritmos evolutivos multi-objetivo (MOEAs), capaces de gestionar MOPs. Los MOEAs siguen los mismos principios de los EAs (descritos en la Figura 7.1) pero incluyen los mecanismos necesarios para operar con MOPs.

Hay muchas maneras de implementar un MOEA [25–28]. El NSGA-II (Non-dominated Sorting Genetic Algorithm II) [25] se ha utilizado con éxito en una amplia variedad de problemas y también se ha empleado en el desarrollo de esta tesis. El principal objetivo del NSGA-II es encontrar una generación P_{t+1} de N individuos a partir de una población anterior P_t con N individuos también. La evolución entre generaciones se desarrolla con los operadores de selección, recombinación y mutación y otros criterios definidos a continuación.

- *Clases no dominadas.* La población está ordenada según el criterio de no dominación. Los individuos de la población se agrupan en diferentes frentes $F_i(i = 0, 1, ...)$, donde i indica el nivel de no dominación, siendo F_0 el frente de los individuos que dominan el resto de individuos, F_1 es el siguiente frente, solo dominado por F_0, y así sucesivamente.
- *Distancia de amontonamiento.* Mide la cercanía de un individuo a sus vecinos. Para reducir la aglomeración de individuos, es necesario que los individuos estén distantes entre sí. El control de esta distancia se utiliza para mejorar la diversidad de la población.
- *Operador de selección.* NSGA-II utiliza el operador de selección por torneo [29]. Este operador elige aleatoriamente k individuos de P_t, y de estos k individuos se selecciona el que se encuentra en el

mejor frente. En el caso de que los k individuos estén ubicados en el mismo frente, se selecciona el que tenga la mayor distancia de amontonamiento, favoreciendo así la diversidad. Este proceso se repite hasta que una población Q_t de N individuos esté disponible. La población Q_t es sometida a cambios usando los operadores de recombinación y mutación. Finalmente, se construye una población R_t uniendo P_t y Q_t, $R_t = P_t \cup Q_t$.

- *Elitismo y población de la siguiente iteración.* La población de la siguiente generación P_{t+1} se forma con los individuos de los mejores frentes de R_t (truncando el número de individuos a N).

7.4. Estructura de la Tesis

Este trabajo está dividido en cuatro capítulos principales (Capítulos 2-5). Cada capítulo se puede leer de forma independiente y tiene su propia sección de conclusiones. Sin embargo, es muy recomendable leer primero el Capítulo 2, ya que el resto de capítulos hacen referencia a él. De esta forma, el lector comprenderá mejor el resto de capítulos.

Los primeros dos capítulos (Capítulos 2 y 3) se centran en la definición del procedimiento evolutivo aplicado a un modelo compacto para OTFTs, que a su vez incluye un modelo para la región de contacto. El Capítulo 4 se centra en la adaptación del modelo compacto para fototransistores orgánicos (OPTs). Finalmente, el Capítulo 5 se centra en mejorar el modelado de los contactos de los OTFTs.

En el capítulo 2 se propone un procedimiento evolutivo para la extracción de parámetros. Para extraer los parámetros del modelo del OTFT a partir de curvas experimentales de salida, este procedimiento hace uso de un MOEA. Se debe decir que este procedimiento evolutivo garantiza la estimación de un conjunto de parámetros, siempre que el espacio de búsqueda de cada parámetro se haya definido correctamente.

En el Capítulo 3, el procedimiento evolutivo se completa con la información proporcionada por un modelo de la conductancia para OTFTs. Esta información se incluye en el procedimiento de extracción en forma de objetivos y restricciones. El procedimiento se emplea de nuevo para extraer los parámetros del modelo a partir de las características de salida experimentales de dispositivos concretos.

En el Capítulo 4, el modelo compacto y el modelo de la región de contacto se amplían para tener en cuenta los efectos de la iluminación en los fototransistores orgánicos (OPT). El estudio de dos dispositivos bajo diferentes condiciones de iluminación confirma que la región de contacto de los fototransistores es muy sensible a los efectos fotovoltaicos y fotoconductores. Debido a este hecho, no solo deben considerarse los efectos de contacto cuando se realiza una extracción de parámetros, sino también el efecto de la iluminación en la región de contacto.

En el Capítulo 5, la funcionalidad del modelo de la región de contacto se amplía, dando lugar a un modelo semi-empírico y estándar. Originalmente, el modelo de la región de contacto y, por lo tanto, el procedimiento evolutivo, solo se podía aplicar a dispositivos con contactos limitados por carga espacial. Al ampliar el rango de un parámetro de este modelo, se extiende el alcance de este modelo (y el procedimiento evolutivo) a dispositivos en los que los contactos son limitados por barreras Schottky.

La memoria de la tesis termina con las siguientes conclusiones y recomendaciones para trabajos futuros.

7.5. Conclusiones

1. Se ha desarrollado un procedimiento evolutivo de extracción de parámetros. El procedimiento determina simultáneamente tanto los parámetros de un modelo compacto de OTFTs a partir de curvas experimentales de corriente-voltaje como los parámetros que caracterizan la región de contacto de los propios OTFTs. Este procedimiento mejora deficiencias encontradas en anteriores procedimientos de extracción de parámetros, por ejemplo, en aquellas situaciones en las que el conjunto de parámetros extraídos por otros procedimientos no cumple con su significado físico, o si existe un ajuste deficiente entre los datos experimentales y los resultados analíticos. En el último caso, el procedimiento evolutivo se puede utilizar como un método de optimización. El procedimiento evolutivo de extracción de parámetros se ha aplicado a las características de salida experimentales de diferentes transistores, obteniendo resultados muy precisos.

2. Para asegurar que los parámetros extraídos mantienen su significado físico, el procedimiento evolutivo se ha ampliado con reglas adicionales en forma de restricciones y objetivos de optimización. Estos cambios han dado lugar a un MOP con más de dos objetivos (MaOP). Para validar los cambios llevados a cabo, el procedimiento resultante ha sido aplicado a nuevos datos experimentales obteniendo también excelentes resultados.

3. Se ha propuesto una modificación del modelo de la región contacto para extender su aplicabilidad a fototransistores orgánicos. El modelo para la región de contacto de estos dispositivos incorpora los efectos de la iluminación. Este modelo es válido para todos los regímenes de operación de los transistores. Una vez más, el modelo compacto y el modelo de la región de contacto se validan con datos experimentales de varios OPTs bajo diferentes condiciones de iluminación. Los resultados muestran que tanto los efectos fotoconductores como los fotovoltaicos afectan a la región intrínseca del transistor, así como al comportamiento eléctrico de la región de contacto. Los parámetros utilizados en el modelo de la región de contacto están vinculados a estos efectos fotovoltaicos y fotoconductores.

4. Se ha propuesto una modificación final del modelo de la región de contacto para describir las características de corriente-voltaje de diferentes tipos de contactos. En este sentido, se ha propuesto un modelo estándar y semi-empírico para la región de contacto de OTFTs, el cual ha sido integrado en el modelo compacto original que describe las características corriente-voltaje de OTFTs. Es un modelo versátil que reproduce el comportamiento de los contactos Schottky o limitados por carga espacial. Es un modelo unificado y simple, ya que solo se necesita el valor de un parámetro para distinguir entre los dos tipos de contactos. El modelo ha sido probado con datos experimentales procedentes de dispositivos con contactos Schottky y limitados por carga espacial. En particular, se ha detectado que la región de contacto de un sensor de amoniaco es muy sensible a la concentración de gas, de tal manera que un contacto limitado por carga espacial se transforma en un contacto Schottky con la presencia de gas.

References

[1] Organic Electronics Association et al. OE-A roadmap for organic and printed electronics. *White Paper (2017)*, 2017.

[2] M. Jamal Deen, M.H. Kazemeini, and S. Holdcroft. Contact effects and extraction of intrinsic parameters in poly(3-alkylthiophene) thin film field-effect transistors. *J. Appl. Phys.*, 103(12):124509, June 2008.

[3] P. Lara Bullejos, J. A. Jiménez Tejada, S. Rodríguez-Bolívar, M. J. Deen, and O. Marinov. Model for the injection of charge through the contacts of organic transistors. *Journal of Applied Physics*, 105(8):084516, apr 2009.

[4] J. A. Jiménez Tejada, J. A. López Villanueva, P. López-Varo, K. M. Awawdeh, and M. J. Deen. Compact modeling and contact effects in organic transistors. *IEEE Trans. Electron Devices*, 61(2):266–277, 2014.

[5] Rodrigo Picos, Oscar Calvo, Benjamín Iñiguez, Eugeni García-Moreno, Rodolfo García, and Magali Estrada. Optimized parameter extraction using fuzzy logic. *Solid-state electronics*, 51(5):683–690, 2007.

[6] Zachary A. Lamport, Hamna F. Haneef, Sajant Anand, Matthew Waldrip, and Oana D. Jurchescu. Tutorial: Organic field-effect transistors: Materials, structure and operation. *Journal of Applied Physics*, 124(7):071101, aug 2018.

[7] Aurélie Morley, Giles Lloyd, Micaël Charbonneau, Denis Locatelli, Stéphanie Lombard, Christelle Laugier, Laurent Tournon, Stephen Bain, Mark James, and Howard Wang. 44.2: Invited paper: Printed polymer TFTs towards low-cost backplane production. *SID Symposium Digest of Technical Papers*, 49:476–478, apr 2018.

[8] Gerd Grau and Vivek Subramanian. Fully high-speed gravure printed, low-variability, high-performance organic polymer transistors with sub-5 v operation. *Advanced Electronic Materials*, 2(4):1500328, jan 2016.

[9] Hua Bai and Gaoquan Shi. Gas sensors based on conducting polymers. *Sensors*, 7(3):267–307, mar 2007.

[10] Myeon-Cheon Choi, Youngkyoo Kim, and Chang-Sik Ha. Polymers for flexible displays: From material selection to device applications. *Progress in Polymer Science*, 33(6):581–630, jun 2008.

[11] S. Jacob, S. Abdinia, M. Benwadih, J. Bablet, I. Chartier, R. Gwoziecki, E. Cantatore, A.H.M. van Roermund, L. Maddiona, F. Tramontana, G. Maiellaro, L. Mariucci, M. Rapisarda, G. Palmisano, and R. Coppard. High performance printed n and p-type OTFTs enabling digital and analog complementary circuits on flexible plastic substrate. *Solid-State Electronics*, 84:167–178, jun 2013.

[12] Iain McCulloch, Martin Heeney, Clare Bailey, Kristijonas Genevicius, Iain MacDonald, Maxim Shkunov, David Sparrowe, Steve Tierney, Robert Wagner, Weimin Zhang, Michael L. Chabinyc, R. Joseph Kline, Michael D. McGehee, and Michael F. Toney. Liquid-crystalline semiconducting polymers with high charge-carrier mobility. *Nature Materials*, 5(4):328–333, mar 2006.

[13] He Yan, Zhihua Chen, Yan Zheng, Christopher Newman, Jordan R. Quinn, Florian Dötz, Marcel Kastler, and Antonio Facchetti. A high-mobility electron-transporting polymer for printed transistors. *Nature*, 457(7230):679–686, jan 2009.

[14] Sanjiv Sambandan, Rene Lujan, Ana Claudia Arias, Christopher R. Newman, and Antonio Facchetti. Electrical stability of inkjet-patterned organic complementary inverters measured in ambient conditions. *Applied Physics Letters*, 94(23):233307, jun 2009.

[15] Hagen Klauk, Ute Zschieschang, Jens Pflaum, and Marcus Halik. Ultralow-power organic complementary circuits. *Nature*, 445(7129):745–748, feb 2007.

[16] He Yan, Yan Zheng, Robert Blache, Christopher Newman, Shaofeng Lu, Jasmin Woerle, and Antonio Facchetti. Solution processed top-gate n-channel transistors and complementary circuits on plastics operating in ambient conditions. *Advanced Materials*, 20(18):3393–3398, jul 2008.

[17] R. Blache, J. Krumm, and W. Fix. Organic CMOS circuits for RFID applications. In *2009 IEEE International Solid-State Circuits Conference - Digest of Technical Papers*. IEEE, feb 2009.

[18] D. J. Gundlach, L. Zhou, J. A. Nichols, T. N. Jackson, P. V. Necliudov, and M. S. Shur. An experimental study of contact effects in organic thin film transistors. *Journal of Applied Physics*, 100(2):024509, jul 2006.

[19] A. Valletta, A. Daami, M. Benwadih, R. Coppard, G. Fortunato, M. Rapisarda, F. Torricelli, and L. Mariucci. Contact effects in high performance fully printed p-channel organic thin film transistors. *Applied Physics Letters*, 99(23):233309, dec 2011.

[20] Chang-Hyun Kim and Gilles Horowitz. Toward a fully analytical contact resistance expression in organic transistors. *Materials*, 12(7), 2019.

[21] X. Yu and M. Gen. *Introduction to evolutionary algorithms*. Springer, 2010.

[22] A.E. Eiben and J.E. Smith. *Introduction to evolutionary computing*, volume 53. Springer, 2003.

[23] C. L. Hwang and A. S. M. Masud. *Multiple objective decision making—methods and applications: a state-of-the-art survey*, volume 164. Springer, 2012.

[24] V. Pareto. *Cours d'économie politique*, volume 1. Librairie Droz, 1964.

[25] Kalyanmoy Deb, Amrit Pratap, Sameer Agarwal, and TAMT Meyarivan. A fast and elitist multiobjective genetic algorithm: Nsga-ii. *IEEE transactions on evolutionary computation*, 6(2):182–197, 2002.

[26] Eckart Zitzler, Marco Laumanns, and Lothar Thiele. Spea2: Improving the strength pareto evolutionary algorithm. *TIK-report*, 103, 2001.

[27] C.M Fonseca and P.J. Fleming. Genetic algorithms for multiobjective optimization: Formulationdiscussion and generalization. In *Proc. of the 5th ICGA*, pages 416–423, San Francisco, CA, USA, 1993. Morgan Kaufmann Publishers Inc.

[28] J. Horn, N. Nafpliotis, and D.E. Goldberg. Multiobjective optimization using the niched pareto genetic algorithm. Technical Report 93005, Department of Computer Science, University of Illinois at Urbana-Champaign, July 1993.

[29] D.E. Goldberg and K. Deb. A comparative analysis of selection schemes used in genetic algorithms. In *Foundations of Genetic Algorithms*, pages 69–93. Morgan Kaufmann, 1991.

[30] Kazuo Takimiya, Masahiro Nakano, Hiroyoshi Sugino, and Itaru Osaka. Design and elaboration of organic molecules for high field-effect-mobility semiconductors. *Synthetic Metals*, 217:68–78, 2016.

[31] Takafumi Uemura, Cedric Rolin, Tung-Huei Ke, Pavlo Fesenko, Jan Genoe, Paul Heremans, and Jun Takeya. On the extraction of charge carrier mobility in high-mobility organic transistors. *Advanced Materials*, 28(1):151–155, 2016.

[32] Kenjiro Fukuda, Yasunori Takeda, Makoto Mizukami, Daisuke Kumaki, and Shizuo Tokito. Fully solution-processed flexible organic thin film transistor arrays with high mobility and exceptional uniformity. *Scientific reports*, 4:3947, 2014.

[33] R Picos, E Garcia, M Estrada, A Cerdeira, and B Iñiguez. Effect of process variations on an OTFT compact model parameters. *International Journal of High Speed Electronics and Systems*, 20(04):815–828, 2011.

[34] P. V. Necliudov, M. S. Shur, D. J. Gundlach, and T. N. Jackson. Modeling of organic thin film transistors of different designs. *J. Appl. Phys.*, 88(11):6594–6597, November 2000.

[35] W. Liu and C. Hu. *BSIM4 and MOSFET modeling for IC simulation*. World Scientific, November 2011.

[36] F. Torricelli, M. Ghittorelli, M. Rapisarda, A. Valletta, L. Mariucci, S. Jacob, R. Coppard, E. Cantatore, Z.M. Kovács-Vajna, and L. Colalongo. Unified drain-current model of complementary p- and n-type OTFTs. *Org. Electron.*, 22(Supplement C):5–11, July 2015.

[37] A. Valletta, M. Rapisarda, S. Calvi, G. Fortunato, M. Frasca, G. Maira, A. Ciccazzo, and L. Mariucci. A DC and small signal AC model for organic thin film transistors including contact effects and non quasi static regime. *Org. Electron.*, 41(Supplement C):345–354, February 2017.

[38] Rodrigo Picos, Eugeni Garcia-Moreno, M Moner Al Chawa, and Leon O Chua. Using memristor formalism in semiconductor device modeling. In *Meeting Abstracts*, pages 2048–2048. The Electrochemical Society, 2017.

[39] J. A. Jiménez Tejada, K. M. Awawdeh, J. A. López Villanueva, J. E. Carceller, M. J. Deen, N. B. Chaure, T. Basova, and A. K. Ray. Contact effects in compact models of organic thin film transistors: Application to zinc phthalocyanine-based transistors. *Org. Electron.*, 12(5):832–842, May 2011.

[40] J. A. Jiménez Tejada, P. López-Varo, Andrew N. Cammidge, Isabelle Chambrier, Michael J. Cook, Nandu B. Chaure, and Asim K. Ray. Compact modeling of organic thin-film transistors with solution processed octadecyl substituted tetrabenzotriazaporphyrin as an active layer. *IEEE Transactions on Electron Devices*, 64(6):2629–2634, jun 2017.

[41] Mustafa Fayez, Khaled Mohamed Morsi, and Mohammed Nabil Sabry. OTFTs compact models: analysis, comparison, and insights. *IET Circuits, Devices & Systems*, 11(5):409–420, sep 2017.

[42] K.M. Awawdeh, J.A. Jiménez Tejada, P. López Varo, J.A. López Villanueva, F.M. Gómez Campos, and M.J. Deen. Characterization of organic thin film transistors with hysteresis and contact effects. *Organic Electronics*, 14(12):3286–3296, dec 2013.

[43] K. D. Holland, A. U. Alam, N. Paydavosi, M. Wong, C. M. Rogers, S. Rizwan, D. Kienle, and M. Vaidyanathan. Impact of contact resistance on the f_t and $f_{\text{máx}}$ of graphene versus MoS_2 transistors. *IEEE Trans. Nanotechnol.*, 16(1):94–106, January 2017.

[44] S. V. Suryavanshi and E. Pop. S2DS: Physics-based compact model for circuit simulation of two-dimensional semiconductor devices including non-idealities. *J. Appl. Phys.*, 120(22):224503, December 2016.

[45] C. Rolin, E. Kang, J. H. Lee, G. Borghs, P. Heremans, and J. Genoe. Charge carrier mobility in thin films of organic semiconductors by the gated van der pauw method. *Nat. Commun.*, 8:14975, April 2017.

[46] D. Dasgupta and Z. Michalewicz. *Evolutionary Algorithms in Engineering Applications*. Springer Publishing Company, Incorporated, 2014.

[47] J.S. Gero, V.A. Kazakov, and T. Schnier. *Genetic Engineering and Design Problems*, pages 47–68. Springer Berlin Heidelberg, Berlin, Heidelberg, 1997.

[48] S.J. Louis, F. Zhao, and X. Zeng. *Flaw Detection and Configuration with Genetic Algorithms*, pages 103–116. Springer Berlin Heidelberg, Berlin, Heidelberg, 1997.

[49] D. Dasgupta. *Optimal Scheduling of Thermal Power Generation Using Evolutionary Algorithms*, pages 317–328. Springer Berlin Heidelberg, Berlin, Heidelberg, 1997.

[50] G. Antoun, M. El-Nozahi, W. Fikry, and H. Abbas. A hybrid genetic algorithm for MOSFET parameter extraction. In *CCECE 2003 - Canadian Conference on Electrical and Computer Engineering. Toward a Caring and Humane Technology (Cat. No.03CH37436)*, volume 2, pages 1111–1114, May 2003.

[51] B. Gross and P. Roosen. Total process optimization in chemical engineering with evolutionary algorithms. *Comput. Chem. Eng.*, 22(Supplement 1):S229–S236, March 1998. European Symposium on Computer Aided Process Engineering-8.

[52] D.L. Carroll. Chemical laser modeling with genetic algorithms. *AIAA J.*, 34(2):338–346, February 1996.

[53] K. Deb. *GeneAS: A Robust Optimal Design Technique for Mechanical Component Design*, pages 497–514. Springer Berlin Heidelberg, Berlin, Heidelberg, 1997.

[54] J.A. Jervase, H. Bourdoucen, and A. Al-Lawati. Solar cell parameter extraction using genetic algorithms. *Meas. Sci. Technol.*, 12(11):1922–1925, October 2001.

[55] J. Alcalá-Fdez, L. Sánchez, S. García, M. J. del Jesús, S. Ventura, J. M. Garrell, J. Otero, C. Romero, J. Bacardit, V. M. Rivas, J. C. Fernández, and F. Herrera. Keel: A software tool to assess evolutionary algorithms for data mining problems. *Soft Comput.*, 13(3):307–318, October 2008.

[56] D.C. Dracopoulos. *Genetic Algorithms and Genetic Programming for Control*, pages 329–343. Springer Berlin Heidelberg, Berlin, Heidelberg, 1997.

[57] B.C. Floresand V. Kreinovich and R. Vasquez. *Signal Design for Radar Imaging in Radar Astronomy: Genetic Optimization*, pages 409–423. Springer Berlin Heidelberg, Berlin, Heidelberg, 1997.

[58] R Picos, M Roca, O Calvo, and E Garcia-Moreno. Characterisation of radiation effects on MOSFET using genetic algorithms. In *Devices, Circuits and Systems, 2000. Proceedings of the 2000 Third IEEE International Caracas Conference on*, pages D52–1. IEEE, 2000.

[59] J. Watts, C. Bittner, D. Heaberlin, and J. Hoffmann. Extraction of compact model parameters for ULSI MOSFETs using a genetic algorithm. In *Proceedings of Second International Conference on Modeling and Simulation of Microsystems, Cambridge, MA, November*, pages 176–179, 1999.

[60] M. Keser, K. Joardar, and M. Motorola. Genetic algorithm based MOSFET model parameter extraction. In *Technical Proceedings of the 2000 International Conference on Modeling and Simulation of Microsystems*, pages 341–344, 2000.

[61] Y. Li and Y. Y. Cho. Parallel genetic algorithm for SPICE model parameter extraction. In *Proc. 20th IEEE IPDPS*, page 8, April 2006.

[62] M.U. Siddiqui and M. Abido. Parameter estimation for five- and seven-parameter photovoltaic electrical models using evolutionary algorithms. *Appl. Soft Comput.*, 13(12):4608–4621, December 2013.

[63] D. Halboot, A. Bakar, T. Khatib, and I. Ahmed. Parameters extraction of double diode photovoltaic module's model based on hybrid evolutionary algorithm. *Energy Conversion and Management*, 105(Supplement C):552–561, August 2015.

[64] Nicolai Moldovan, Rodrigo Picos, and Eugenio Garcia-Moreno. Parameter extraction of a solar cell compact model usign genetic algorithms. In *Electron Devices, 2009. CDE 2009. Spanish Conference on*, pages 379–382. IEEE, 2009.

[65] P Moreno, R Picos, M Roca, E Garcia-Moreno, B Iniguez, and M Estrada. Parameter extraction method using genetic algorithms for an improved OTFT compact model. In *Electron Devices, 2007 Spanish Conference on*, pages 64–67. IEEE, 2007.

[66] Rodrigo Picos, Eugeni Garcia-Moreno, and Benjamin Iniguez. Non-traditional OTFT parameter extraction. In *Meeting Abstracts*, pages 1240–1240. The Electrochemical Society, 2007.

[67] Eugenio Garcia-Moreno, Benjamin Iniguez, and Rodrigo Picos. Directed genetic algorithms for OTFT model parameter extraction. In *Solid-State and Integrated-Circuit Technology, 2008. ICSICT 2008. 9th International Conference on*, pages 424–427. IEEE, 2008.

[68] O. Marinov, M. J. Deen, U. Zschieschang, and H. Klauk. Organic thin-film transistors: Part I-compact dc modeling. *IEEE Trans. Electron Devices*, 56:2952–2961, 2009.

[69] M. J. Deen, O. Marinov, U. Zschieschang, and H. Klauk. Organic Thin-Film Transistors: Part II. Parameter Extraction. *IEEE Trans. Electron Devices*, 56(12):2962 –2968, Dec. 2009.

[70] B.H. Hamadani and D. Natelson. Extracting contact effects in organic FETs. *Proceedings of the IEEE*, 93(7):1306–1311, jul 2005.

[71] P. López Varo, J.A. Jiménez Tejada, J.A. López Villanueva, J.E. Carceller, and M.J. Deen. Modeling the transition from ohmic to space charge limited current in organic semiconductors. *Organic Electronics*, 13(9):1700–1709, sep 2012.

[72] A. Cerdeira, M. Estrada, R. García, A. Ortiz-Conde, and F.J. Garcıía Sánchez. New procedure for the extraction of basic a-Si:H TFT model parameters in the linear and saturation regions. *Solid-State Electron.*, 45(7):1077–1080, July 2001.

[73] R. L. Burden and D. J. Faires. *Numerical analysis*. PWS Publishing Company, Boston, 3 edition, 1985.

[74] Adelmo Ortiz-Conde, Francisco J García-Sánchez, Juan Muci, Alberto Terán Barrios, Juin J Liou, and Ching-Sung Ho. Revisiting MOSFET threshold voltage extraction methods. *Microelectronics Reliability*, 53(1):90–104, 2013.

[75] M.J. Deen and Z.X. Yan. A new method for measuring the threshold voltage of small-geometry MOSFETs from subthreshold conduction. *Solid-State Electronics*, 33(5):503 – 511, 1990.

[76] Z.X. Yan and M.J. Deen. Physically-based method for measuring the threshold voltage of MOSFETs. *IEE Proceedings G Circuits, Devices and Systems*, 138(3):351, 1991.

[77] Y. H. Hu and S. Pan. Saposm: an optimization method applied to parameter extraction of MOSFET models. *IEEE Transactions on Computer-Aided Design of Integrated Circuits and Systems*, 12(10):1481–1487, Oct 1993.

[78] T. Sakurai, B. Lin, and A. R. Newton. Fast simulated diffusion: an optimization algorithm for multiminimum problems and its application to MOSFET model parameter extraction. *IEEE Transactions on Computer-Aided Design of Integrated Circuits and Systems*, 11(2):228–234, Feb 1992.

[79] Rodrigo Picos, Miquel Roca, Benjamin Iñiguez, and Eugeni Garcia-Moreno. A new MOSFET parameter extraction method using genetic algorithms. In *1999 Proceedings of CDE*, 1999.

[80] R. A. Thakker, N. Gandhi, M. B. Patil, and K. G. Anil. Parameter extraction for PSP MOSFET model using particle swarm optimization. In *2007 International Workshop on Physics of Semiconductor Devices*, pages 130–133, Dec 2007.

[81] K. Deb, A. Pratap, S. Agarwal, and T. Meyarivan. A fast and elitist multiobjective genetic algorithm: NSGA-II. *IEEE Transactions on Evolutionary Computation*, 6(2):182–197, apr 2002.

[82] Eckart Zitzler, Marco Laumanns, and Lothar Thiele. Spea2: Improving the strength pareto evolutionary algorithm. *TIK-report*, 103, 2001.

[83] R. B. Agrawal and K. Deb. Simulated binary crossover for continuous search space. *Complex Systems*, 9(2):115–148, 1995.

[84] H.-G. Beyer and K. Deb. On self-adaptive features in real-parameter evolutionary algorithms. *Trans. Evol. Comp*, 5(3):250–270, June 2001.

[85] K. Deb and S. Agrawal. *A Niched-Penalty Approach for Constraint Handling in Genetic Algorithms*, pages 235–243. Springer Vienna, Vienna, 1999.

[86] K. Deb and D. Deb. Analysing mutation schemes for real-parameter genetic algorithms. *Int. J. Artif. Intell. Soft Comput.*, 4(1):1–28, February 2014.

[87] J. González, I. Rojas, J. Ortega, H. Pomares, F.J. Fernandez, and A.F. Díaz. Multiobjective evolutionary optimization of the size, shape, and position parameters of radial basis function networks for function approximation. *IEEE Trans. Neural Netw.*, 14(6):1478–1495, November 2003.

[88] Sean Luke. ECJ evolutionary computation library, 1998. Available for free at http://cs.gmu.edu/∼eclab/projects/ecj/.

[89] M. C. Hamilton, S. Martin, and J. Kanicki. Thin-film organic polymer phototransistors. *IEEE Transactions on Electron Devices*, 51(6):877–885, June 2004.

[90] J. A. Jiménez Tejada, Pilar Lopez-Varo, Nandu B. Chaure, Isabelle Chambrier, Andrew N. Cammidge, Michael J. Cook, Ali Jafari-Fini, and Asim K. Ray. Organic thin film transistors using a liquid crystalline palladium phthalocyanine as active layer. *Journal of Applied Physics*, 123(11):115501, mar 2018.

[91] Nandu B Chaure, Andrew N Cammidge, Isabelle Chambrier, Michael J Cook, Markys G Cain, Craig E Murphy, Chandana Pal, and Asim K Ray. High-mobility solution-processed copper phthalocyanine-based organic field-effect transistors. *Science and technology of advanced materials*, 12(2):025001, 2011.

[92] A. Romero, J. González, R. Picos, M.J. Deen, and J.A. Jiménez-Tejada. Evolutionary parameter extraction for an organic tft compact model including contact effects. *Organic Electronics*, 61:242 – 253, 2018.

[93] P. Lara Bullejos, J. A. Jiménez Tejada, F. M. Gómez-Campos, M. J. Deen, and O. Marinov. Evaluation of the charge density in the contact region of organic thin film transistors. *Journal of Applied Physics*, 106(9):094503, 2009.

[94] Bingdong Li, Jinlong Li, Ke Tang, and Xin Yao. Many-objective evolutionary algorithms: A survey. *ACM Computing Surveys (CSUR)*, 48(1):13, 2015.

[95] Luisa Torsi, Francesco Marinelli, M Daniela Angione, Antonio Dell'Aquila, Nicola Cioffi, Elvira De Giglio, and Luigia Sabbatini. Contact effects in organic thin-film transistor sensors. *Organic Electronics*, 10(2):233–239, 2009.

[96] Pengcheng Gu, Yifan Yao, Linlin Feng, Shujie Niu, and Huanli Dong. Recent advances in polymer phototransistors. *Polymer Chemistry*, 6(46):7933–7944, 2015.

[97] O Marinov, M Jamal Deen, and B Iniguez. Performance of organic thin-film transistors. *Journal of Vacuum Science & Technology B: Microelectronics and Nanometer Structures Processing, Measurement, and Phenomena*, 24(4):1728–1733, 2006.

[98] Jordi Carrabina, Mohammad Mashayekhi, Jofre Pallarès, and Lluis Terés. Inkjet-configurable gate arrays (IGA). *IEEE Transactions on Emerging Topics in Computing*, 5(2):238–246, apr 2017.

[99] Ta-Ya Chu, Zhiyi Zhang, Afshin Dadvand, Christophe Py, Stephen Lang, and Ye Tao. Direct writing of inkjet-printed short channel organic thin film transistors. *Organic Electronics*, 51:485–489, dec 2017.

[100] Zhe Qi, Jiamin Cao, Hui Li, Liming Ding, and Jizheng Wang. High-performance thermally stable organic phototransistors based on PSeTPTI/PC61bm for visible and ultraviolet photodetection. *Advanced Functional Materials*, 25(21):3138–3146, apr 2015.

[101] Jianfeng Zhong, Xiaomin Wu, Shuqiong Lan, Yuan Fang, Huipeng Chen, and Tailiang Guo. High performance flexible organic phototransistors with ultrashort channel length. *ACS Photonics*, 5(9):3712–3722, aug 2018.

[102] Xuhua Wang, Kamol Wasapinyokul, Wei De Tan, Ruth Rawcliffe, Alasdair J. Campbell, and Donal D. C. Bradley. Device physics of highly sensitive thin film polyfluorene copolymer organic phototransistors. *Journal of Applied Physics*, 107(2):024509, jan 2010.

[103] Yingquan Peng, Wenli Lv, Bo Yao, Jipeng Xie, Ting Yang, Guoying Fan, Deqiang Chen, Pengjie Gao, Maoqing Zhou, and Ying Wang. Improved performance of photosensitive field-effect transistors based on palladium phthalocyanine by utilizing al as source and drain electrodes. *IEEE Transactions on Electron Devices*, 60(3):1208–1212, mar 2013.

[104] Yanlian Lei, Ning Li, Wing-Kin Edward Chan, Beng S. Ong, and Furong Zhu. Highly sensitive near infrared organic phototransistors based on conjugated polymer nanowire networks. *Organic Electronics*, 48:12–18, sep 2017.

[105] Bo Yao, Yan Li, Zebo Fang, Yongsheng Tan, Shiyan Liu, Yingquan Peng, and Haitao Xu. Investigation of the source-drain electrodes/the active layer contact-effect on the performance of organic phototransistor. *Synthetic Metals*, 233:58–62, nov 2017.

[106] C. S. Suchand Sangeeth, P. Stadler, S. Schaur, N. S. Sariciftci, and Reghu Menon. Interfaces and traps in pentacene field-effect transistor. *Journal of Applied Physics*, 108(11):113703, dec 2010.

[107] W. Boukhili, C. Tozlu, M. Mahdouani, S. Erten-Ela, and R. Bourguiga. Illumination and dipole layer effects on the density of state distribution in n-type organic thin film phototransistors based on naphthalene bis-benzimidazole: Experiment and modeling. *Microelectronic Engineering*, 179:37–47, jul 2017.

[108] Xiaohui Liu, Mingjun Zhang, Guifang Dong, Xinyue Zhang, Yapei Wang, Lian Duan, Liduo Wang, and Yong Qiu. The effect of oxygen content on the performance of low-voltage organic phototransistor memory. *Organic Electronics*, 15(7):1664–1671, jul 2014.

[109] Yingquan Peng, Wenli Lv, Bo Yao, Guoying Fan, Deqiang Chen, Pengjie Gao, Maoqing Zhou, and Ying Wang. High performance near infrared photosensitive organic field-effect transistors realized by an organic hybrid planar-bulk heterojunction. *Organic Electronics*, 14(4):1045–1051, apr 2013.

[110] O. Marinov, M.J. Deen, and B. Iniguez. Charge transport in organic and polymer thin-film transistors: recent issues. *IEE Proceedings - Circuits, Devices and Systems*, 152(3):189, 2005.

[111] A. Romero, J. Gonzalez, and J.A. Jimenez-Tejada. Constrained many-objective evolutionary extraction procedure for an OTFT compact model including contact effects. In *2018 Spanish Conference on Electron Devices (CDE)*. IEEE, nov 2018.

[112] M. J. Deen, M. H. Kazemeini, Y. M. Haddara, J. Yu, G. Vamvounis, S. Holdcroft, and W. Woods. Electrical characterization of polymer-based FETs fabricated by spin-coating poly(3-alkylthiophene)s. *IEEE Trans. Electron. Dev.*, 51(11):1892–1901, nov 2004.

[113] Pilar López-Varo, J. A. Jiménez Tejada, Ognian Marinov, JE Carceller, CH Chen, and MJ Deen. Boundary condition model for the simulation of organic solar cells. *Organic Electronics*, 48:85–95, 2017.

[114] O. Marinov, M. J. Deen, and R. Datars. Compact modeling of charge carrier mobility in organic thin-film transistors. *J. Appl. Phys.*, 106(6):064501, sep 2009.

[115] Y. Tsividis. *Operation and Modeling of the MOS Transistor*. New York: McGraw-Hill, 2nd edition, 1999.

[116] M.D. Jacunski, M.S. Shur, A.A. Owusu, T. Ytterdal, M. Hack, and B. Iniguez. A short-channel DC SPICE model for polysilicon thin-film transistors including temperature effects. *IEEE Transactions on Electron Devices*, 46(6):1146–1158, jun 1999.

[117] Michael S Shur, Tor A Fjeldly, and Trond Ytterdal. Transistor modeling for the vdsm era. In *Quality Electronic Design, 2000. ISQED 2000. Proceedings. IEEE 2000 First International Symposium on*, pages 37–43. IEEE, 2000.

[118] Ognian Marinov, M. Jamal Deen, Cong Feng, and Yiliang Wu. Precise parameter extraction technique for organic thin-film transistors operating in the linear regime. *Journal of Applied Physics*, 115(3):034506, jan 2014.

[119] Hyo-Soon Kang, Chang-Soon Choi, Woo-Young Choi, Dae-Hyun Kim, and Kwang-Seok Seo. Characterization of phototransistor internal gain in metamorphic high-electron-mobility transistors. *Applied Physics Letters*, 84(19):3780–3782, may 2004.

[120] R. Liguori, W.C. Sheets, A. Facchetti, and A. Rubino. Light- and bias-induced effects in pentacene-based thin film phototransistors with a photocurable polymer dielectric. *Organic Electronics*, 28:147–154, jan 2016.

[121] Ling Li, Nianduan Lu, Ming Liu, and Heinz Bässler. General einstein relation model in disordered organic semiconductors under quasiequilibrium. *Physical Review B*, 90(21), dec 2014.

[122] Zhiwei Zong, Ling Li, Jin Jang, Zhigang Li, Nianduan Lu, Liwei Shang, Zhuoyu Ji, and Ming Liu. A new surface potential-based compact model for a-IGZO TFTs in RFID applications. In *2014 IEEE International Electron Devices Meeting*. IEEE, dec 2014.

[123] S. Mansouri, A. Jouili, L. El Mir, Ahmed A. Al-Ghamdi, and F. Yakuphanoglu. Studies of photosensitivity and photo-induced negative differential resistance (NDR) of TIPS-pentacene-poly(3-hexyl)thiophene blend organic thin film transistor. *Synthetic Metals*, 207:1–12, sep 2015.

[124] Johannes Milvich, Tarek Zaki, Mahdieh Aghamohammadi, Reinhold Rödel, Ulrike Kraft, Hagen Klauk, and J. N. Burghartz. Flexible low-voltage organic phototransistors based on air-stable dinaphtho[2,3-b:2′,3′-f]thieno[3,2-b]thiophene (DNTT). *Organic Electronics*, 20:63–68, may 2015.

[125] M.J. Deen and M.H. Kazemeini. Photosensitive polymer thin-film FETs based on poly(3-octylthiophene). *Proceedings of the IEEE*, 93(7):1312–1320, jul 2005.

[126] Y. Takanashi, K. Takahata, and Y. Muramoto. Characteristics of InAlAs/InGaAs high electron mobility transistors under 1.3-μm laser illumination. *IEEE Electron Device Letters*, 19(12):472–474, dec 1998.

[127] Y. Takanashi, K. Takahata, and Y. Muramoto. Characteristics of InAlAs/InGaAs high-electron-mobility transistors under illumination with modulated light. *IEEE Transactions on Electron Devices*, 46(12):2271–2277, 1999.

[128] C. Y. Chen. Theory of a modulated barrier photodiode. *Applied Physics Letters*, 39(12):979–981, 1981.

[129] Cem Tozlu, Mahmut Kus, Mustafa Can, and Mustafa Ersöz. Solution processed white light photodetector based n, n′-di (2-ethylhexyl)-3,4,9,10-perylene diimide thin film phototransistor. *Thin Solid Films*, 569:22–27, oct 2014.

[130] Wentao Huang, Yen-Hung Lin, and Thomas D. Anthopoulos. High speed ultraviolet phototransistors based on an ambipolar fullerene derivative. *ACS Applied Materials & Interfaces*, 10(12):10202–10210, mar 2018.

[131] Cem Tozlu, Sule Erten-Ela, and Siddik Icli. Photoresponsive n-channel organic field effect transistor based on naphthalene bis-benzimidazole with divinyltetramethyl disiloxane-bis (benzo-cyclobutene) gate insulator. *Sensors and Actuators A: Physical*, 161(1-2):46–52, 2010.

[132] Petr Toman, Miroslav Menšík, Wojciech Bartkowiak, and Jiří Pfleger. Modelling of the charge carrier mobility in disordered linear polymer materials. *Physical Chemistry Chemical Physics*, 19(11):7760–7771, 2017.

[133] A. Jouili, S. Mansouri, Ahmed A. Al-Ghamdi, L. El Mir, W. A. Farooq, and F. Yakuphanoglu. Characterization and modeling of nano-organic thin film phototransistors based on 6,13(triisopropylsilylethynyl)-pentacene: Photovoltaic effect. *Journal of Electronic Materials*, 46(4):2221–2231, dec 2016.

[134] Erika Kozma and Marinella Catellani. Perylene diimides based materials for organic solar cells. *Dyes and Pigments*, 98(1):160–179, jul 2013.

[135] Chen Li and Henrike Wonneberger. Perylene imides for organic photovoltaics: Yesterday, today, and tomorrow. *Advanced Materials*, 24(5):613–636, jan 2012.

[136] B. Li, C. Y. Han, P. T. Lai, and W. M. Tang. Effects of source/drain-electrode material, thickness and fabrication method on the electrical performance of pentacene thin-film transistor. *Thin Solid Films*, 667:28 – 33, 2018.

[137] Shiny Nair, M Kathiresan, and T Mukundan. Two dimensional simulation of patternable conducting polymer electrode based organic thin film transistor. *Semicond. Sci. and Tech.*, 33(2):025006, jan 2018.

[138] Tribeni Borthakur and Ranjit Sarma. Top-contact pentacene-based organic thin film transistor (OTFT) with n,n'-bis(3-methyl phenyl)-n,n'-diphenyl benzidine (TPD)/au bilayer source-drain electrode. *J. Electron. Mater.*, 47(1):627–632, Jan 2018.

[139] Yaochuan Mei, Derek Fogel, Jihua Chen, Jeremy W. Ward, Marcia M. Payne, John E. Anthony, and Oana D. Jurchescu. Interface engineering to enhance charge injection and transport in solution-deposited organic transistors. *Org. Electron.*, 50:100 – 105, 2017.

[140] Alexandra F. Paterson, Yen-Hung Lin, Alexander D. Mottram, Zhuping Fei, Muhammad R. Niazi, Ahmad R. Kirmani, Aram Amassian, Olga Solomeshch, Nir Tessler, Martin Heeney, and Thomas D. Anthopoulos. The impact of molecular p-doping on charge transport in high-mobility small-molecule/polymer blend organic transistors. *Adv. Electron. Mater.*, 4(10):1700464, 2018.

[141] Pablo Lara Bullejos, Juan A. Jiménez Tejada, M. J. Deen, O. Marinov, and W. R. Datars. Unified model for the injection and transport of charge in organic diodes. *Journal of Applied Physics*, 103(6):064504, mar 2008.

[142] L. Mariucci, M. Rapisarda, A. Valletta, S. Jacob, M. Benwadih, and G. Fortunato. Current spreading effects in fully printed p-channel organic thin film transistors with schottky source–drain contacts. *Org. Electron.*, 14(1):86–93, jan 2013.

[143] M. Charbonneau, D. Locatelli, S. Lombard, C. Serbutoviez, L. Tournon, F. Torricelli, S. Abdinia, E. Cantatore, and M. Fattori. A large-area gravure printed process for p-type organic thin-film transistors on plastic substrates. In *2018 48th European Solid-State Device Research Conference (ESSDERC)*. IEEE, sep 2018.

[144] A. Romero, C. Jiménez, J. González, P. López-Varo, M. J. Deen, and J. A. Jiménez-Tejada. Compact modeling of the effects of illumination on the contact region of organic phototransistors. *Organic Electronics*, 70:113 – 121, 2019.

[145] H. H. Berger. Contact resistance and contact resistivity. *J. Electrochem. Soc.*, 119(4):507–514, 1972.

[146] Ulrike Kraft, John E. Anthony, Emilie Ripaud, Marsha A. Loth, Edwin Weber, and Hagen Klauk. Low-voltage organic transistors based on tetraceno[2,3-b]thiophene: Contact resistance and air stability. *Chem. Mater.*, 27(3):998–1004, 2015.

[147] Markus Krammer, James Borchert, Andreas Petritz, Esther Karner-Petritz, Gerburg Schider, Barbara Stadlober, Hagen Klauk, and Karin Zojer. Critical evaluation of organic thin-film transistor models. *Crystals*, 9(2):85, feb 2019.

[148] S. Abdinia, F. Torricelli, G. Maiellaro, R. Coppard, A. Daami, S. Jacob, L. Mariucci, G. Palmisano, E. Ragonese, F. Tramontana, A.H.M. van Roermund, and E. Cantatore. Variation-based design of an AM demodulator in a printed complementary organic technology. *Organic Electronics*, 15(4):904–912, apr 2014.

[149] Alex M Ma and Douglas W Barlage. Analysis of the channel and contact regions in staggered and drain-offset zno thin-film transistors with compact modeling. *IEEE Transactions on Electron Devices*, 65(8):3277–3282, 2018.

[150] Rodrigo Martins, Diana Gaspar, Manuel J. Mendes, Luis Pereira, Jorge Martins, Pydi Bahubalindruni, Pedro Barquinha, and Elvira Fortunato. Papertronics: Multigate paper transistor for multifunction applications. *Appl. Mater. Today*, 12:402–414, sep 2018.

[151] M. Buonomo, N. Lago, G. Cantarella, N. Wrachien, M. Natali, F. Prescimone, E. Benvenuti, M. Muccini, S. Toffanin, and A. Cester. Simple and accurate single transistor technique for parameters extraction from organic and inorganic thin film devices. *Organic Electronics*, 63:376–383, dec 2018.

[152] S. Fatima, U. Rafique, U.F. Ahmed, and M.M. Ahmed. A global parameters extraction technique to model organic field effect transistors output characteristics. *Solid-State Electron.*, 152:81–92, feb 2019.

[153] Masataka Higashiwaki, Keita Konishi, Kohei Sasaki, Ken Goto, Kazushiro Nomura, Quang Tu Thieu, Rie Togashi, Hisashi Murakami, Yoshinao Kumagai, Bo Monemar, Akinori Koukitu, Akito Kuramata, and Shigenobu Yamakoshi. Temperature-dependent capacitance–voltage and current–voltage characteristics of pt/ga2o3 (001) schottky barrier diodes fabricated on n—ga2o3 drift layers grown by halide vapor phase epitaxy. *Applied Physics Letters*, 108(13):133503, mar 2016.

[154] M. Rapisarda, A. Valletta, A. Daami, S. Jacob, M. Benwadih, R. Coppard, G. Fortunato, and L. Mariucci. Analysis of contact effects in fully printed p-channel organic thin film transistors. *Org. Electron.*, 13(10):2017–2027, oct 2012.

[155] P. López-Varo, J. A. Jiménez-Tejada, J. A. López-Villanueva, and M. J. Deen. Space-charge and injection limited current in organic diodes: A unified model. *Organic Electronics*, 15(10):2526 – 2535, 2014.

[156] C. Rolin, E. Kang, J. H. Lee, G. Borghs, P. Heremans, and J. Genoe. Charge carrier mobility in thin films of organic semiconductors by the gated van der Pauw method. *Nat. Commun.*, 8:14975, 2017.

[157] Chang-Hyun Kim, Suzanne Thomas, Ji Hwan Kim, Martin Elliott, J. Emyr Macdonald, and Myung-Han Yoon. Potentiometric parameterization of dinaphtho[2,3-b:2′,3′-f]thieno[3,2-b]thiophene field-effect transistors with a varying degree of nonidealities. *Advanced Electronic Materials*, 4(7):1700514, may 2018.

[158] J. Ross Macdonald. Impedance spectroscopy. *Annals of Biomedical Engineering*, 20(3):289–305, May 1992.

[159] James W. Borchert, Boyu Peng, Florian Letzkus, Joachim N. Burghartz, Paddy K. L. Chan, Karin Zojer, Sabine Ludwigs, and Hagen Klauk. Small contact resistance and high-frequency operation of flexible low-voltage inverted coplanar organic transistors. *Nat. Commun.*, 10(1), mar 2019.

[160] V.R. Rajeev, Akhil K. Paulose, and K.N. Narayanan Unni. Ammonia gas detection using field-effect transistor based on a solution-processable organic semiconductor. *Vacuum*, 158:271–277, dec 2018.

[161] Marco Farina and Paolo Amato. On the optimal solution definition for many-criteria optimization problems. In *Proceedings of the NAFIPS-FLINT international conference*, pages 233–238, 2002.

[162] Liangli Zhen, Miqing Li, Ran Cheng, Dezhong Peng, and Xin Yao. Multiobjective test problems with degenerate pareto fronts. *arXiv preprint arXiv:1806.02706*, 2018.

[163] Dhish Kumar Saxena, João A. Duro, Ashutosh Tiwari, Kalyanmoy Deb, and Qingfu Zhang. Objective reduction in many-objective optimization: Linear and nonlinear algorithms. *IEEE Transactions on Evolutionary Computation*, 17(1):77–99, feb 2013.

[164] Antonio López Jaimes and Carlos A. Coello Coello. Many-objective problems: Challenges and methods. In *Springer Handbook of Computational Intelligence*, pages 1033–1046. Springer Berlin Heidelberg, 2015.

[165] V. Khare, X. Yao, and K. Deb. Performance scaling of multi-objective evolutionary algorithms. In *Lecture Notes in Computer Science*, pages 376–390. Springer Berlin Heidelberg, 2003.

[166] Hai-Lin Liu, Lei Chen, Qingfu Zhang, and Kalyanmoy Deb. Adaptively allocating search effort in challenging many-objective optimization problems. *IEEE Transactions on Evolutionary Computation*, 22(3):433–448, 2018.

[167] K. Ikeda, H. Kita, and S. Kobayashi. Failure of pareto-based MOEAs: does non-dominated really mean near to optimal? In *Proceedings of the 2001 Congress on Evolutionary Computation (IEEE Cat. No.01TH8546)*. IEEE.

[168] Thomas Hanne. Global multiobjective optimization with evolutionary algorithms: Selection mechanisms and mutation control. In *Lecture Notes in Computer Science*, pages 197–212. Springer Berlin Heidelberg, 2001.

[169] K. Deb, L. Thiele, M. Laumanns, and E. Zitzler. Scalable multi-objective optimization test problems. In *Proceedings of the 2002 Congress on Evolutionary Computation. CEC'02 (Cat. No.02TH8600)*. IEEE.

[170] Maha Elarbi, Slim Bechikh, Abhishek Gupta, Lamjed Ben Said, and Yew-Soon Ong. A new decomposition-based NSGA-II for many-objective optimization. *IEEE Transactions on Systems, Man, and Cybernetics: Systems*, 48(7):1191–1210, jul 2018.

[171] Kalyanmoy Deb and Himanshu Jain. An evolutionary many-objective optimization algorithm using reference-point-based nondominated sorting approach, part i: Solving problems with box constraints. *IEEE Transactions on Evolutionary Computation*, 18(4):577–601, aug 2014.

[172] Himanshu Jain and Kalyanmoy Deb. An evolutionary many-objective optimization algorithm using reference-point based nondominated sorting approach, part ii: Handling constraints and extending to an adaptive approach. *IEEE Trans. Evolutionary Computation*, 18(4):602–622, 2014.

[173] P. J. Bentley and J. P. Wakefield. Finding acceptable solutions in the pareto-optimal range using multiobjective genetic algorithms. In *Soft Computing in Engineering Design and Manufacturing*, pages 231–240. Springer London, 1998.

[174] Nicole Drechsler, Rolf Drechsler, and Bernd Becker. Multi-objective optimization in evolutionary algorithms using satisfiability classes. In *Lecture Notes in Computer Science*, pages 108–117. Springer Berlin Heidelberg, 1999.

[175] Dimo Brockhoff and Eckart Zitzler. Are all objectives necessary? on dimensionality reduction in evolutionary multiobjective optimization. In *Parallel Problem Solving from Nature - PPSN IX*, pages 533–542. Springer Berlin Heidelberg, 2006.

[176] Antonio López Jaimes, Carlos A. Coello Coello, and Debrup Chakraborty. Objective reduction using a feature selection technique. In *Proceedings of the 10th annual conference on Genetic and evolutionary computation*. ACM Press, 2008.

[177] Hemant Kumar Singh, Amitay Isaacs, and Tapabrata Ray. A pareto corner search evolutionary algorithm and dimensionality reduction in many-objective optimization problems. *IEEE Transactions on Evolutionary Computation*, 15(4):539–556, aug 2011.

[178] Dhish Kumar Saxena and Kalyanmoy Deb. Non-linear dimensionality reduction procedures for certain large-dimensional multi-objective optimization problems: Employing correntropy and a novel maximum variance unfolding. In *Lecture Notes in Computer Science*, pages 772–787. Springer Berlin Heidelberg.

[179] Tinkle Chugh, Karthik Sindhya, Kaisa Miettinen, Jussi Hakanen, and Yaochu Jin. On constraint handling in surrogate-assisted evolutionary many-objective optimization. In *International Conference on Parallel Problem Solving from Nature*, pages 214–224. Springer, 2016.

[180] C.M. Fonseca and P.J. Fleming. Multiobjective optimization and multiple constraint handling with evolutionary algorithms. i. a unified formulation. *IEEE Transactions on Systems, Man, and Cybernetics - Part A: Systems and Humans*, 28(1):26–37, 1998.

[181] AKM Khaled Ahsan Talukder, Kalyanmoy Deb, and Julian Blank. Visualization of the boundary solutions of high dimensional pareto front from a decision maker's perspective. In *Proceedings of the Genetic and Evolutionary Computation Conference Companion on - GECCO '18*. ACM Press, 2018.

[182] AKM Khaled Ahsan Talukder and Kalyanmoy Deb. A topologically consistent visualization of high dimensional pareto-front for multi-criteria decision making. In *2018 IEEE Symposium Series on Computational Intelligence (SSCI)*. IEEE, nov 2018.

[183] Edward J. Wegman. Hyperdimensional data analysis using parallel coordinates. *Journal of the American Statistical Association*, 85(411):664–675, sep 1990.

[184] Shigeru Obayashi and Daisuke Sasaki. Visualization and data mining of pareto solutions using self-organizing map. In *Lecture Notes in Computer Science*, pages 796–809. Springer Berlin Heidelberg, 2003.

Appendix I

IA. Publications.

Publications by date of delivery at the University of Granada:

Journal publications

1) Evolutionary parameter extraction for an organic TFT compact model including contact effects. A. Romero, J. González, R. Picos, M. J. Deen, J. A. Jiménez-Tejada. *Organic Electronics*, **2018**.

2) Compact modeling of the effects of illumination on the contact region of organic phototransistors. A. Romero, C. Jiménez, J. González, M. J. Deen, J. A. Jiménez-Tejada. *Organic Electronics*, **2019**.

3) Standard Model for the Contact Region of Organic Thin-Film Transistors. A. Romero, J. González, M. J. Deen, J. A. Jiménez-Tejada. *Organic Electronics*, **2019** *(submitted)*.

Conference publications

1) Constrained Many-Objective Evolutionary Extraction Procedure for an OTFT Compact Model including Contact Effects. A. Romero, J. González, J. A. Jiménez-Tejada. *IEEE Proceedings of the 12th Spanish Conference on Electron Devices, CDE'2018*, **Nov. 2018**.

2) **Invited paper.** Evolutionary Parameter Extraction for Organic TFT Compact Models Including Contact Effects A. Romero, J. González, R. Picos, M. J. Deen, J. A. Jiménez-Tejada. *ECS-235th Electrochemical Society, Meeting Abstracts*, **2019**.

3) Dependence with illumination of the contact region of organic phototransistors. A. Romero, J. González, M. J. Deen, J. A. Jiménez-Tejada. *CAD-TFT 2019 Workshop, Tarragona (Spain), July 9-10*, **2019**.